

6 April 2018

Response to the comments of Reviewer 2 on

“Multivariate analysis of Kelvin wave seasonal variability in ECMWF L91 analyses”

by Marten Blaauw and Nedjeljka Žagar

Dear Referee,

thank you very much for your comments and suggestion on our manuscript.

We have revised paper following your criticism and suggestions. In particular, we have re-written parts of Introduction and methodology sections in order to better describe novel features of the applied method.

Enclosed please find our responses to your comments using the same organisation as in your review. Your comments are coloured blue whereas our responses are in black.

Your sincerely,

Marten Blaauw and Nedjeljka Žagar

## GENERAL COMMENTS:

*The authors have developed a powerful analysis technique whereby they are able to decompose any 3-dimensional atmospheric analysis product into its (linear) global normal modes, which includes the equatorial Kelvin wave as one of its components. As I understand it, this decomposition is computed for each individual time point of the analysis, and no information on the propagation from one time point to the next is used for the categorization into the different normal modes. This is quite different to what has been done in many other studies, for example, Wheeler and Kiladis (1999) who used wavenumber-frequency spectra and filtering for identification of equatorial waves. Therefore, what is called a "Kelvin wave" in this study is somewhat different to those C1 ACPD Interactive comment Printer-friendly version Discussion paper other studies, since the identified structures may not be propagating, but may be stationary or even display propagation in the opposite direction to what is usually ascribed to a particular mode. This difference with other studies requires careful explanation and should be highlighted, but is not necessarily a problem with the paper.*

*Another aspect of this work that I think needs highlighting is that the normal mode decomposition is based on the assumption that the equations of motion are linearized about a basic state of rest (i.e. zero winds, line 88). It is unclear to me how much this assumption may affect the results.*

*I also wonder what assumptions are made about the static stability for the calculation of the normal modes. The static stability is important for setting the relationship between the horizontal and vertical structures of the normal modes. For the same gravity wave speed,  $c$ , a Kelvin wave in the stratosphere will have a shorter vertical wavelength than a Kelvin wave in the troposphere, due to the different static stability. But both these Kelvin waves will have the same meridional (horizontal) structure, which is set by the equatorial Rossby radius, a function of  $c$ , where  $c$  is the gravity wave speed. The meridional length scale is actually  $\sqrt{c/\beta}$ , where  $\beta$  is  $df/dy$ . So what temperature and static stability profiles do you assume, and how can this affect the results? What would happen if you assumed a "moist static stability" for the troposphere? Instead of the traditional dry static stability?*

*To be more convinced about the utility of the technique for understanding, I also wonder what the wavenumber-frequency spectra of the decomposed "Kelvin waves" would look like. You could do this at each level and see what equivalent depth dominates at each level. I imagine that in the troposphere you may see a predominance of the MJO and the  $c \sim 20\text{m/s}$  convectively-coupled Kelvin waves, but as you enter the stratosphere the equivalent depth should start increasing due to the filtering provided by the background winds. These results would be useful to compare to Hendon and Wheeler (2008, J. Atmos. Sci., Vol 65).*

*Perhaps another interesting comparison to make is how the transient behaviour in OLR matches the transient behaviour in your Kelvin wave dataset. Do the convectively-coupled Kelvin waves identified in OLR by the technique of Wheeler and Kiladis (1999) show up in your independent Kelvin wave dataset? To me, this would be much more interesting than some of the analysis provided here.*

*In summary, I must admit that I was a little underwhelmed by the results presented here. I think more interesting things could have been studied. But at the same time, the work is rigorous and may be more interesting to others, so it still adds something to the published literature*

## **Response**

### **1. Methodology**

The first goal of our paper is to introduce a novel methodology for the Kelvin wave filtering and demonstrate it by examples and diagnostics with similarity to previous studies.

We use analytical relationships for the horizontal structure of the Kelvin wave wind and geopotential height perturbations on the sphere. This is different from many previous studies which relied on the Kelvin wave solutions on the equatorial beta plane. We sum up linear Kelvin wave solutions in many shallow-water equation systems (60 in our case). The extension of the Kelvin wave analysis by 2D approach (on individual horizontal levels or vertical planes) to the three-dimensional (3D) spherical coordinates is an important step for realistic filtering of Kelvin waves in global datasets. As shown by Boyd and Zhou (J. Atmos. Sci., 2008), the degree of the Kelvin wave equatorial confinement on the sphere is controlled not only by the equivalent depth (i.e. by the equatorial Rossby radius of deformation) but also by the zonal wavenumber. Therefore, even barotropic Kelvin waves with equivalent depth around 10 km on the sphere are trapped to the equator. This is a strong reason to use the spherical Kelvin wave solution for the projection.

Data projection on horizontal Kelvin wave structure, along with other equatorial waves, on individual time instants was performed before by Tindall et al (2006, QJRMS). In the revised paper we add also a reference to a similar approach by Yang et al (J. Atmos. Sci., 2003) for data on individual levels using the equatorial beta plane solutions and using the equatorial Rossby deformation radius as the fitting parameter. We also refer to Žagar et al (QJRMS, 2005, 2007) who used analytical solutions on the equatorial beta plane to analyze the distribution of the equatorial wave variance in the short-term forecast errors of the ECWMF model.

Our Kelvin wave signal at any time is a sum of many Kelvin waves with different phase speeds. As the applied normal-mode function projection provides a complete projection basis, we can quantify the amount of total variance associated with Kelvin waves in global data.

We have re-written parts of Introduction and other sections in order to better highlight methodology approach and what kind of outputs it provides. We believe that here are many research questions regarding the Kelvin and other equatorial waves where the presented method can provide added insight and complement other methods.

### **2. Comparison with spectral space-time filtering (so-called Wheeler-Kiladis diagrams)**

Our filtering procedure is different from the widely used spectral space-time filtering pioneering by Hayashi (1972) that applies Kelvin wave dispersion relations. We analyze circulation data at selected processing times independently of other times. In other words, the dispersion relationship for the linear Kelvin waves on the sphere, used to derive the analytical expressions for the Kelvin wave wind and geopotential height, is not used explicitly in the data analysis. At every analyzed time step, in every grid point we

sum up contributions from 60 Kelvin wave solutions for each zonal wavenumber. Nevertheless, the linear wave features readily persist in our outputs for the Kelvin waves as shown in the example and Hovmoeller diagrams in the Result section. This result alone is very interesting as it validates the linear wave theory approach that has been successfully employed in many studies, especially for the large-scale tropical circulation features.

The spectral space-time filtering does not consider the meridional wave structure. The normal-mode function projection, thanks to its 3D orthogonal structures, allows a full quantification of the Kelvin wave signal and its spatial localization.

We agree that would be interesting to combine the two different methods on analyzing Kelvin waves. But such analysis is beyond the scope of the present paper. Previously mentioned paper by Yang et al (J. Atmos. Sci., 2003) and several their follow-on studies combined the space-time filtering and the projection on analytical equatorial wave solution on the equatorial beta plane. Our 6.5 year long dataset is also shorter than time series used in space-time filtering. We aim to perform some comparison of the two methods within the ongoing analysis of Kelvin waves in several decades long time series from reanalysis data.

### **3. Linearization about a basic state of rest**

This is not a drawback of the method as wave frequencies are used solely for the formulation of the projection basis and not for studying the wave propagation properties. Namely, the frequencies differ depending on whether the linearization is performed around the state of rest as in our case or the mean flow is taken into account. If the mean zonal flow is taken into account, the frequencies of wave solutions can become unstable, as well as continuous, except for a few of the lowest balanced modes (Kasahara, 1980). Fortunately, the meridional structures of the Hough functions are not significantly different if the linearization is performed around the non-zero mean zonal flow (see Corrigendum to Kasahara, 1980, J. Atmos. Sci.). It is therefore suitable to use the Hough functions constructed with reference to the basic state at rest as a basis for the projection.

We have discussed this issue in the paper by Žagar et al. (2015, Geo. Model Dev.) where the projection method has been described in details. In Žagar et al. (2017, J. Atmos. Sci.) we demonstrated that even inertia-gravity waves with smaller scales can be successfully represented by the method. Another paper using the same decomposition, currently also in ACP Discussion, demonstrates the same point: <https://www.atmos-chem-phys-discuss.net/acp-2018-228/>

The impact of latitudinal shear on the Kelvin waves was previously shown negligible by Boyd (1978, J. Atmos. Sci.).

### **4. Assumptions about the static stability for the calculation of the normal modes**

Stability and temperature are globally averaged and their temporal changes are not significant for the structure of the basis functions for the projection. In any case, definition of stability is a part of the derivation procedure by Kasahara and Puri (1981, Mon. Wea. Rev.) that considers hydrostatic atmosphere described by primitive equations. Moisture enters in the computation of geopotential on the terrain-following levels where virtual temperature is used.

We did not spend extra space on such details as it has been discussed in previous papers where we discussed the normal-mode function projection methodology. For example, Žagar et al. (2015, Geo. Model Dev.) showed typical vertical profiles of globally averaged temperature and stability which are input to the vertical structure equation. Normal-mode functions are derived for the bounded atmosphere with lid located at the model top half-level (pressure=0, sigma = 0). The same condition is applied in NWP models and indeed in the model of ECMWF that produced the analyzed data.

With the global surface temperature specified, the equivalent depth of the first vertical mode (barotropic mode) is always about 10 km as the barotropic equivalent depth depends only on the surface temperature and the atmosphere depth (Cohn and Dee, QJRMS, 1989). Analysis of Staniforth et al. (1985) showed that the equivalent depths for subsequent internal modes are relatively insensitive to the value of the surface boundary condition, but they are sensitive to the top boundary conditions (stability and the depth of the top model layers). This means that the vertical model depth matters for the shape of the vertical structure functions. This is the reason why we analyzed only their sum i.e. the total Kelvin wave signal and not individual vertical modes.

#### **SPECIFIC COMMENTS:**

*Line 5. Why do you call it a "barotropic" KW response? Shouldn't this be the baroclinic mode with a half-sinusoid vertical structure in the troposphere?*

**Response:** Thank you for noticing this typo. The abstract has been rewritten.

*Line 64. Missing "the" before "information".*

**Response:** Corrected. Thank.

*Lines 74 or 75. Change to "covers approximately 6.5 years from January 2007 until June 2013".*

**Response:** Changed as suggested.

*Line 93. "denotedm"?*

**Response:** This typo has been corrected.

*Lines 104-105. It is confusing to me to denote the KW as the  $n=0$  EIG mode, since in many other papers (e.g. Matsuno 1966 and Wheeler and Kiladis 1999) the  $n=0$  mode is the continuation of the mixed Rossby-gravity mode through the wavenumber 0 axis. In these papers the KW is the  $n=-1$  solution.*

**Response:** We follow derivation and classification of wave solutions of the linearized shallow-water equations on the sphere from Žagar et al. (2015, Geo. Mod. Dev.) and references therein. Enclosed is figure 1 from the paper which shows dispersion curves for four equivalent depths.

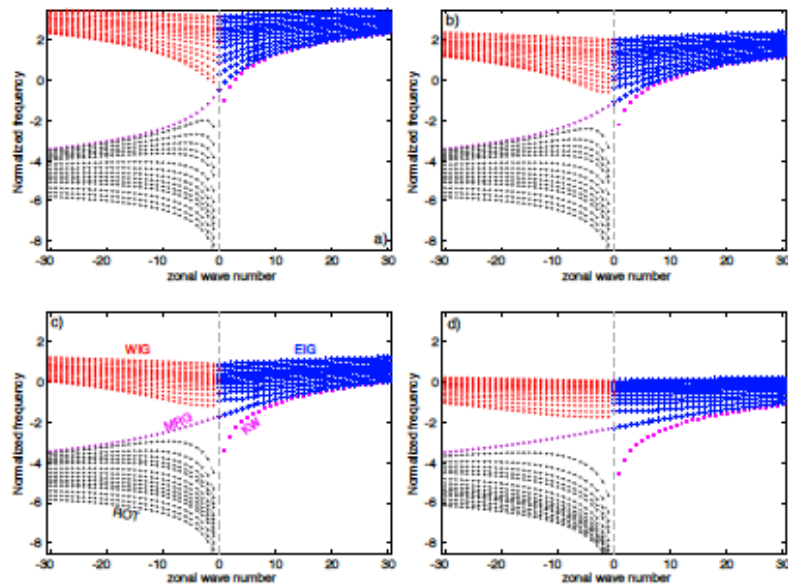


**Figure 1.** Frequencies of spherical normal modes for different equivalent depths. (a)  $D = 10$  km, (b)  $D = 1$  km, (c)  $D = 100$  m and (d)  $D = 10$  m. Frequencies are normalized by  $2\Omega$  factor and shown in a logarithmic scale. Frequencies of the easterly and westerly inertia-gravity modes (EIG and WIG, respectively) are shown for the meridional modes  $n = 0, 1, 3, 6, 9, 14, 19, 24, 29, 34, 39, 49, 59$  and  $69$ . For the balanced modes (ROT), meridional modes are shown for  $n = 0, 1, 3, 5, 7, 9, 14, 19, 24, 29, 34, 39, 49, 59$  and  $69$ . Frequencies of the Kelvin modes ( $n = 0$  EIG) and MRG modes ( $n = 0$  ROT) are shown by magenta-coloured symbols. Frequencies of ROT modes  $n > 1$  are denoted by grey circles and interconnected by dashed black lines. The EIG and WIG mode frequencies are shown by blue and red symbols, respectively. Negative frequencies correspond to negative values of zonal wave numbers. Frequencies for  $k = 0$  are zero for all ROT modes, for the MRG mode, for the Kelvin mode and for the  $n = 0$  WIG mode. For  $n > 0$  and  $k = 0$ , frequencies of the WIG modes have opposite signs and equal values as the EIG mode frequencies. For  $k > 1$ , frequencies of the WIG modes have larger absolute values than frequencies of the EIG modes for the same  $n$ .

Lines 138-139. I found this difficult to read because of the use of parentheses to provide the opposite meaning – please read the paper <https://eos.org/opinions/parentheses-are-not-for-references-and-clarification-saving-space>

**Response:** It has been changed throughout the text.

Line 141. "zonal wind" not "zonal wave".

**Response:** Changed as suggested.

Line 146 and many other locations. Add "the" before "Eastern hemisphere".

**Response:** Corrected.

Figure 4. I didn't find this figure to be very informative. A wavenumber-frequency spectrum of the Kelvin wave dataset at a few different vertical levels would have been more interesting.

**Response:** In the spectral i.e. modal space we can not provide the Kelvin wave energy spectrum on individual levels as we perform vertical decomposition. At each level, our KW wind and temperature perturbations include contributions from 60 spherical shallow water models meaning 60 phase speeds. While it is different from previous studies of Kelvin wave spectrum, our spectrum quantifies the vertically integrated Kelvin wave total (potential + kinetic) energy in global data. This integrated energy depends on the vertical model depth. This is a property of the global normal-mode decomposition which may be

most different from widely used single shallow-water equation system on the equatorial beta plane.

*Line 221 and many other locations. What is "summer" at the equator? It doesn't make sense to call the seasons using "summer", "autumn", "winter", and "spring" for equatorial waves. I would prefer you just call them "DJF", "MAM", "JJA", "SON".*

**Response:** Changed everywhere as suggested.

*Line 260. You say "when the ENSO index is positive". Do you mean "during El Nino"?*

**Response:** Yes. Changed as suggested.

*Lines 262-265. It is perhaps also important to note that the MJO was quite strong in 2007-08 (e.g. as defined by the Real-time Multivariate MJO index), and that the MJO has been found to be generally stronger in easterly QBO years (Sun et al. 2017). I am also fairly certain that the MJO must project quite stronger onto your Kelvin wave mode.*

**Response:** Thank you. We have updated text to include your comment on the strong MJO in this period of the strong KW activity.

*Line 298. I think you mean "warm anomalies", not "heating"*

**Response:** Changed as suggested.

*Line 305. Why do you call these intramonthly KWs the "free propagating" waves? If "free" means away from the forcing of convection, then isn't every wave in the stratosphere "free"?*

**Response:** We agree with the referee that the term "free propagating" KWs refers to the part of the Kelvin wave signal away from convective forcing, whereas in our case we discuss intramonthly KWs which are possibly coupled to convection. The revised paper uses the term "intramonthly KWs" to describe waves with periods 3-20 days.

*Line 385. Please call this section "Intramonthly propagating Kelvin waves".*

**Response:** Changed as suggested.

*Figure 13. I found this very difficult to understand. On line 415 you say "different years", but what different years"? Is this a composite of all years? On line 416 you say "specific longitude". What specific longitude? The caption says it is a "climatology", but why is it so noisy if it is a climatology?*

**Response:** The word climatology was not appropriate here. This figure is a composite of intramonthly Kelvin waves in all years as recognized by the reviewer. We have rewritten the caption and figure description in the text.

*Figure 1 caption. Remove text "(panel b in Fig. 1)"*

**Response:** Corrected

*Figure 5. There appears to be some data missing at the end of 2009.*

**Response:** The limits of x-axes in the figure were corrected. Thank you for noticing it.



# Multivariate analysis of Kelvin wave seasonal variability in ECMWF L91 analyses

Marten Blaauw<sup>1</sup> and Nedjeljka Žagar<sup>1</sup>

<sup>1</sup>University of Ljubljana, Faculty of mathematics and physics, Ljubljana, Slovenia

*Correspondence to:* Marten Blaauw (marten.blaauw@fmf.uni-lj.si)

## 1 **Abstract.**

2 The paper performs multivariate analysis of the linear Kelvin waves (KWs) represented by the operational 91-level ECMWF  
3 analyses in 2007-2013 period, with focus on seasonal variability. The applied method simultaneously filters Kelvin wave  
4 wind and temperature perturbations in the continuously stratified atmosphere on the sphere. The spatial filtering of the three-  
5 dimensional Kelvin wave structure in the upper troposphere and lower stratosphere is based on the Hough harmonics using  
6 several tens of linearized shallow-water equation systems on the sphere with equivalent depths ranging from 10 km to a few  
7 meters.

8 Results provide the global Kelvin wave energy spectrum. It shows a clear seasonal cycle with the Kelvin wave activity  
9 predominantly in zonal wavenumbers 1–2 where up to 50% more energy is observed during the solstice seasons in comparison  
10 with boreal spring and autumn.

11 Seasonal variability of Kelvin waves in the upper troposphere and lower stratosphere is examined in relation to the back-  
12 ground wind and stability. A spectral bandpass filtering is used to decompose variability into three period ranges: seasonal,  
13 intraseasonal and intramonthly variability component. Results reveal a slow seasonal KW component with a robust dipole  
14 structure in the upper troposphere with its position determined by the location of the dominant convective outflow throughout  
15 the seasons. Its maximal strength occurs during boreal summer when easterlies in the Eastern hemisphere are strongest. Other  
16 two components represent vertically propagating Kelvin waves and are observed throughout the year with seasonal variability  
17 mostly found in the wave amplitudes being dependent on the seasonality of the background easterly winds and static stability.



## 18 1 Introduction

19 Atmospheric equatorial Kelvin waves (hereafter KWs), first discovered in the stratosphere (Wallace and Kousky, 1968), are  
20 nowadays observed and studied over a broad range of spatial and temporal scales. A broad wavenumber-frequency spectrum  
21 can be traced to the spatiotemporal nature of tropical convection which generates KWs along with a spectrum of other equatorial  
22 waves. Atmospheric wave response to the stochastic nature of convection was studied by Garcia and Salby (1987) and Salby  
23 and Garcia (1987) who made a distinction between (i) projection or vertical response to short-term heating fluctuations (e.g.  
24 daily convection) and (ii) barotropic or horizontal response to seasonal convective heating. For KWs, the vertical response  
25 gives rise to a broad frequency spectrum of vertically propagating KWs that radiate outward into the stratosphere where  
26 they drive zonal-mean quasi-periodic flows such as the quasi-biennial oscillation (QBO, Holton and Lindzen, 1972). The  
27 horizontal response to seasonal transitions in convective heating gives rise to planetary-scale disturbances with a half-sinusoidal  
28 vertical structure confined to the troposphere. A part of this response remains stationary over the convective hotspot; its shape  
29 resembling a classic "Gill-type" KW solution (Gill, 1980). The other part of the response intensifies and advances over the  
30 Pacific, representing a transient component of the Walker circulation (Salby and Garcia, 1987).

31 Both components of the KW response received increased attention in the scientific community over the last decades in terms  
32 of the role they play in the (intra)seasonal variability of the Tropical Tropopause Layer (hereafter TTL), defined as a transition  
33 layer between the typical level of convective outflow at  $\sim 12$  km where the Brunt-Väisälä frequency is at its minimum, and the  
34 cold point tropopause at  $\sim 16$ - $17$  km (Highwood and Hoskins, 1998; Fueglistaler et al., 2009). Within the TTL, temperature  
35 variations play an important role in controlling the stratosphere-troposphere exchange of various species such as ozone and  
36 water vapour thereby aiding in the dehydration process of air entering the stratosphere. The two parts of the KW response  
37 modulate the TTL differently on different time scales (Highwood and Hoskins, 1998; Randel and Wu, 2005; Ryu et al.,  
38 2008; Flannaghan and Fueglistaler, 2013); their relative contribution to TTL dynamics varies with season and is not yet fully  
39 understood. The present study contributes to this topic by applying a novel multivariate analysis of Kelvin wave seasonal  
40 variability in model-level analysis data.

41 Seasonal variations of Kelvin wave dynamics in the TTL have been previously studied using temperature data derived from  
42 satellites such as SABER (Sounding of the Atmosphere using Broadband Emission Radiometry, Garcia et al., 2005; Ern et al.,  
43 2008; Ern and Preusse, 2009), HIRDLS (High Resolution Dynamics Limb Sounder, Alexander and Ortland, 2010), and GPS-  
44 RO (Global Positioning System Radio Occultation, Tsai et al., 2004; Randel and Wu, 2005; Ratnam et al., 2006). For example,  
45 Alexander and Ortland (2010) reported a clear seasonal cycle around 16-17 km ( $\sim 100$  hPa) in KW temperature observed by  
46 HIRDLS, coinciding closely with variations in background stability. A widely used method for the KW filtering from gridded  
47 data is the space-time spectral analysis introduced by Hayashi (1982). Space-time spectral filtering assumes that the linear  
48 adiabatic theory for equatorial waves on a resting atmosphere is applicable (Gill, 1982). Filtering operates on single variable  
49 data and it has been widely used to diagnose equatorial waves in the outgoing longwave radiation (OLR, e.g. Wheeler and  
50 Kiladis, 1999) and climate model outputs (e.g. Lin and Coauthors, 2006). Based on 40-year ECMWF reanalysis (ERA-40)

51 data, Suzuki and Shiotani (2008) found that the temperature component of Kelvin waves tends to peak at 70 hPa while the  
 52 zonal wind peaks at lower altitudes, i.e. at 100 hPa and 150 hPa in Eastern and Western hemisphere, respectively.

53 On the equatorial  $\beta$ -plane, shallow-water linear wave theory describes the Kelvin wave geopotential height ( $h_{kw}$ ) and zonal  
 54 wind ( $u_{kw}$ ) perturbations propagating zonally with phase speed  $c$  as (Matsuno, 1966):

$$55 \quad h_{kw}(x, y) = \frac{c}{g} u_{kw} \quad \text{where} \quad u_{kw}(x, y) = u_0 \exp\left(-\frac{\beta y^2}{2c}\right) \cos k(x - ct). \quad (1)$$

56 Here,  $u_0$  is the zonal wind amplitude at the equator,  $g$  is gravity,  $y$  is the distance from the equator and  $\beta = df/dy$ ,  $f$  being  
 57 the Coriolis parameter. The dispersion relationship between the wave frequency  $\nu$  and the zonal wavenumber  $k$  is  $\nu = kc$ . The  
 58 gravity wave speed in a layer of homogeneous fluid with mean depth  $D$  is given by  $c = \sqrt{gD}$  (Gill, 1982).

59 The KW  $e$ -folding decay width  $a_e$ , known as the equatorial radius of deformation, is given by  $a_e = (c/2\beta)^{1/2}$ . By pre-  
 60 scribing  $D$ , the horizontal structure of KW is defined by (1) for any  $k$  and can be used to simultaneously analyze wind and  
 61 geopotential height perturbations due to KW waves on a single horizontal level. Such analysis was carried out by Tindall et al.  
 62 (2006) for the lower stratosphere for the ERA-15 data in 1981-93 period. Their results suggested that KWs contributes ap-  
 63 proximately 1 K<sup>2</sup> of the temperature variance on the equator with peak activity occurring during solstice seasons at 100 hPa,  
 64 during December–February at 70 hPa and at 50 hPa it occurs during the easterly to westerly quasi-biennial oscillation (QBO)  
 65 phase transition. Yang et al. (2003) used  $a_e$  as the fitting parameter for the projection of the ERA-15 data on the meridional  
 66 structure of the KW and other equatorial waves. They found that the best fit trapping scale within 20°N–20°S is around 6°.  
 67 The multivariate projection of data on the horizontal structures of equatorial waves including KWs on the equatorial  $\beta$ -plane  
 68 was performed also for the short-range forecast errors of the ECMWF model (Žagar et al., 2005, 2007). For example, Žagar  
 69 et al. (2007) found that forecast errors within 20°N–20°S belt project on KWs significantly more in the easterly QBO phase  
 70 than in the westerly phase.

71 In this paper we extend the linear Kelvin wave analysis based on the shallow-water equation theory on the equatorial  $\beta$ -plane  
 72 to the sphere. Second, we extend the KW filtering on individual horizontal levels or vertical planes to the three-dimensional  
 73 (3D) KW analysis simultaneously in wind and temperature fields. This study thus explores seasonal variability of KWs in the  
 74 TTL layer in a multivariate fashion using most of the information on the vertical wave structure available in recent operational  
 75 ECMWF analyses.

76 On the sphere, the Kelvin mode is the slowest eastward-propagating eigensolution of the shallow-water equations (or Laplace  
 77 tidal equations) linearized around a state of rest (e.g. Kasahara, 1976). In the continuously stratified atmosphere, the depth  $D$   
 78 becomes the "equivalent depth" of a given baroclinic mode and we need to solve Laplace tidal equations for a range of  $D$  from  
 79 large (corresponding to the barotropic structure) to rather small (for high baroclinic modes) in order to consider the spectrum  
 80 of Kelvin waves (e.g. Boyd, 2018). In contrast to the Kelvin wave trapping on the equatorial  $\beta$ -plane, which is controlled by  $a_e$   
 81 i.e. by the equivalent depth, the degree of the KW equatorial confinement on the sphere is in addition controlled by the zonal  
 82 wavenumber (Boyd and Zhou, 2008). As shown by Boyd and Zhou (2008), even barotropic KW with  $D$  around 10 km are on  
 83 the sphere confined within the tropical belt.

84 In section 2 we present a methodology which diagnosis 3D Kelvin waves in spherical datasets. Section 3 presents the KW  
 85 energetics in wavenumber space focusing on the seasonal cycle. Section 4 presents seasonal KW variability in several frequency  
 86 bands both for the horizontal as well as for the vertical projection KW response. Conclusions and outlook are given in section  
 87 5.

## 88 2 Data and methodology

89 The Kelvin waves are filtered using the normal-mode function (NMF) decomposition derived by Kasahara and Puri (1981) and  
 90 formulated as the *MODES* software package by Žagar et al. (2015). Here the methodology is briefly summarized followed by  
 91 the method for the computation of the KW temperature perturbations and by examples of the 3D KW structure in global data.

92 Input ECMWF operational analyses covers approximately 6.5 years from January 2007 until June 2013. The dataset starts  
 93 after two important updates in the ECMWF assimilation cycle: a resolution update on 1 February 2006 and the introduction of  
 94 GPS-RO temperature profiles in the assimilation on 12 December 2006. The data ends at the next update in vertical resolution  
 95 from L91 to L137 on 25 June 2013. The data horizontal resolution is  $256 \times 128$  points in the zonal and meridional directions  
 96 (regular Gaussian grid N64), respectively, on 91 irregularly spaced hybrid model levels up to around 0.01 hPa (around 80 km).  
 97 The temporal resolution is 6 hours, i.e. 4 times per day, at 00, 06, 12 and 18 UTC. A case study of the large-scale KW in July  
 98 2007 in this dataset by Žagar et al. (2009) showed that the NMF method provides information on the 3D wave structure and its  
 99 vertical propagation in the stratosphere. Another case study from the same month demonstrated how the vertical KW structure  
 100 improves as the number of vertical levels increased (Žagar et al., 2012).

### 101 2.1 Filtering of Kelvin waves by 3D normal-mode function expansion

102 The basic assumption behind the NMF expansion is that a global state of the atmosphere described by its mass and wind  
 103 variables at any time can be considered as a superposition of the linear wave solutions upon a predefined background state.  
 104 The NMF decomposition derived by Kasahara and Puri (1981) uses the  $\sigma$  vertical coordinate and linearization around the state  
 105 of rest and realistic vertical temperature and stability stratification. 3D wave solutions of linearized primitive equations are  
 106 represented as a truncated time series of the Hough harmonic oscillations and the vertical structure functions. The assump-  
 107 tion of separability leads to separate equations for the vertical structure and horizontal oscillations. The latter are known as  
 108 shallow-water equations on the sphere or Laplace tidal equations without forcing. The two systems are coupled by a separation  
 109 parameter  $D$  which is called the equivalent height (Boyd, 2018). Eigenmodes of the global shallow-water equations are known  
 110 as Hough harmonics. They describe two types of wave motions: Rossby waves and inertia-gravity waves which obey their  
 111 corresponding dispersion relationships on the sphere.

112 The expansion of a global input data vector  $\mathbf{X}(\lambda, \varphi, \sigma) = (u, v, h)^T$  can be represented by a discrete finite series as:

$$113 \begin{pmatrix} u(\lambda, \varphi, \sigma) \\ v(\lambda, \varphi, \sigma) \\ h(\lambda, \varphi, \sigma) \end{pmatrix} = \sum_{m=1}^M \mathbf{S}_m \left[ \sum_{n=1}^R \sum_{k=-K}^K \chi_n^k(m) \mathbf{H}_n^k(\lambda, \varphi; m) \right] G_m(\sigma) \quad (2)$$

114 The input data vector contains wind components  $u, v$  and the transformed geopotential height  $h$  defined as  $h = g^{-1}P$  where  
 115  $g$  is the gravity and  $P$  is defined as:  $P = \Phi + RT_0 \ln(p_s)$ ; that is, it is the sum of geopotential  $\Phi$  and a surface pressure,  $p_s$ ,  
 116 term. Other two variables represent the specific gas constant for dry air ( $R$ ) and the globally-averaged vertical temperature  
 117 profile ( $T_0(\sigma)$ ). The zonal and vertical truncations ( $K$  and  $M$ , respectively) define maximal numbers of zonal waves at a  
 118 single latitude (wavenumber  $k$ ) and a maximal number of vertical modes (denoted  $m$ ) respectively. For every vertical structure  
 119 eigenfunctions  $G_m(\sigma)$ , Hough harmonic functions,  $\mathbf{H}_n^k(\lambda, \varphi)$  describe non-dimensional oscillations in the horizontal plane of  
 120 the fluid with the mean depth equal the equivalent depth  $D_m$ . The parameter  $D_m$  appears in Eq. (2) in the diagonal matrix  $\mathbf{S}_m$   
 121 with elements  $(gD_m)^{1/2}$ ,  $(gD_m)^{1/2}$  and  $D_m$  which normalizes the input data vector after the vertical projection and thereby  
 122 removes dimensions. Parameter  $R$  is the total number of meridional modes which is a sum of the eastward inertio-gravity waves  
 123 (EIG), westward inertio-gravity waves (WIG) and Rossby waves. Linearization about the state of rest is not a drawback of the  
 124 method as wave frequencies are used solely for the formulation of the projection basis and not for studying wave propagation  
 125 properties. As shown by Kasahara (1980) (see also its Corrigendum) the meridional structures of the Hough functions for  
 126 large scales are not significantly different if the linearization is performed around the non-zero mean zonal flow. The impact of  
 127 latitudinal shear on the Kelvin waves was shown negligible by Boyd (1978). Further details of the NMF projection procedure  
 128 are given in Žagar et al. (2015).

129 For each zonal wavenumber, the Kelvin mode is the lowest eastward-propagating latitudinal Hough function. In (2), the  
 130 Kelvin wave is represented by the nondimensional complex expansion coefficients  $\chi_n^k(m)$  with the meridional index  $n = 1$ .  
 131 However, to follow often used notation, we shall denote the Kelvin wave in the remainder of this study as the  $n = 0$  EIG mode,  
 132 i.e. the Kelvin wave wind and geopotential height are represented by coefficients  $\chi_{kw} = \chi_0^k(m)$ . The truncation values are  
 133  $K = 85$  and  $M = 60$ . This means that KW signal in 3D circulation at a single time instant consists of 5100 waves, 85 waves  
 134 in every shallow-water equation system. Higher vertical modes were left out as their equivalent depth is smaller than 2 meters  
 135 and their contribution to the total KW signal is negligible in the outputs in the TTL and the stratosphere. The relation between  
 136 the truncation parameters and the normal-mode projection quality is discussed in Žagar et al. (2015) and references therein.

137 Once the forward projection is carried out and coefficients  $\chi_n^k(m)$  are produced, filtering of KWs in physical space can be  
 138 performed through (2) after setting all  $\chi$ , except those representing the KWs, to zero. The result of filtering are fields  $u_{kw}$ ,  
 139  $v_{kw}$  and  $h_{kw}$  which provide the KW zonal wind, meridional wind and geopotential height perturbations. Notice here that in  
 140 contrast to the equatorial  $\beta$ -plane, KWs on the sphere have a small meridional wind component which is thus left out from  
 141 the discussion (Boyd, 2018).

142 The KW temperature perturbation,  $T_{kw}$  can be derived from the  $h_{kw}$  fields on  $\sigma$  levels using the hydrostatic relation in  $\sigma$   
 143 coordinates:

$$144 \quad T_{kw} = -\frac{g\sigma}{R} \frac{\partial h_{kw}}{\partial \sigma}. \quad (3)$$

145 The orthogonality of the normal-mode basis functions provides KW energy as a function of the zonal wavenumber and  
 146 vertical mode. After the forward projection, the energy spectrum of total (potential and kinetic) energy for each Kelvin wave

147 can be computed using the energy product for the  $k$ th and  $m$ th normal modes (Žagar et al., 2015) as:

$$148 \quad I_{kw}(k, m) = \frac{1}{2} g D_m \chi_{kw} [\chi_{kw}]^* . \quad (4)$$

149 The units are  $\text{J kg}^{-1}$ . The KW global energy spectrum as a function of the zonal wavenumber is obtained by summing energy  
150 in all vertical modes:

$$151 \quad I_{kw}(k) = \frac{1}{2} \sum_{m=1}^M g D_m \chi_{kw} [\chi_{kw}]^* . \quad (5)$$

## 152 2.2 Examples of 3D structure of Kelvin waves in L91 analyses

153 Kelvin waves are shown in Fig. 1-2 for a few days in July 2010 to introduce and illustrate their properties as filtered by the  
154 NMF methodology.

155 Figure 1 illustrates the meridional structure of Kelvin waves on 25 July 2010 on 2 levels. KW activity was found largest in  
156 the zonal wind component at 150 hPa over the Indian Ocean. The geopotential dipole structure is centred over the convective  
157 hotspot over the Maritime continent. At 100 hPa, we find largest amplitude of KW temperature perturbations up to 4 K  
158 positioned above the zonal wind maxima at 150 hPa. The meridional wind component of the KW is nonzero in spherical  
159 coordinates, but is at most  $0.22 \text{ ms}^{-1}$  at 100 hPa which is negligible compared to the zonal wind component (maximum  $12.5$   
160  $\text{ms}^{-1}$ ) making the KW wind field primarily zonal. Note that the presented horizontal structure at a single level is a superposition  
161 of 60 vertical modes, i.e. 60 shallow water models with equivalent depths from about 10 km to a couple of meters.

162 Figure 2 illustrates day-to-day filtered KW fields along the equator on three separate July days in 2010, namely 25, 28 and  
163 31. Both zonal wind (blue-to-red shades) and temperature fields (red contours) are shown. Without any predefined constrains  
164 on the KW propagation, one can observe a rich variety of KW behaviour occurring in time: from the quasi-stationary dipole  
165 patterns centred at 160 hPa to a wave package of free propagating wave structures in the stratosphere transiting from the  
166 western into the eastern hemisphere.

167 In the stratosphere, the uppermost easterly wind component in blue shades around 30 – 50 hPa moves in eastward and  
168 downward direction, demonstrating the upward transport of KW energy (Andrews et al., 1987). KW amplitudes were largest  
169 over Eastern hemisphere with temperatures up to 4 K and zonal winds up to  $12 \text{ ms}^{-1}$ . The large amount of KW activity  
170 occurred during the easterly phase of the QBO with strong easterly winds present between 30 and 80 hPa (not shown), providing  
171 favourable conditions for strong KW activity.

172 Between 100 and 200 hPa during the second half of July, there was low-frequency KW activity present in the form of a  
173 stationary and robust "wave-1" pattern with strong KW easterly winds up to  $24 \text{ ms}^{-1}$  in Eastern Hemisphere and KW westerly  
174 winds up to  $10 \text{ ms}^{-1}$  in the Western Hemisphere. The high vertical resolution within the TTL resolves shallow KW structures  
175 and a typical slanted structure towards the east in KW easterlies as well. The appearance and strength of horizontal KW  
176 response coincides with the presence of strong easterly winds in the TTL in the Eastern Hemisphere during this period (not  
177 shown). Figure 2 also shows that below 300 hPa the KW activity decreases and we shall not discuss levels under 300 hPa in  
178 the paper.

179 The zonal wind and temperature components are coupled through Eq. (3) which states that the amplitude of the negative  
 180 KW temperature perturbation is proportional to the negative vertical gradient in geopotential (and vice versa), as well as in the  
 181 zonal wind since the zonal wind and geopotential are in phase. Horizontally, the cold anomaly is always located between the  
 182 westerly and the easterly phase of the zonal wind component. Vertically, maximal positive temperatures are observed between  
 183 easterly winds below and westerly winds above. An estimate of the vertical wavelength can be made based on alternating zonal  
 184 wind minima and maxima. For example, on 25th July a well-developed KW package extending into the stratosphere moved  
 185 from the Western into the Eastern hemisphere. A quasi-stationary component of the wave package is observed around 60°E  
 186 with easterly winds located at 50 hPa (~ 21.5 km) and 150 hPa (~ 13.5 km), implying a vertical wavelength of around 8 km.  
 187 More examples based on daily basis filtered from the 10-day deterministic forecast of the ECMWF can be found on the  
 188 MODES website<sup>1</sup>.

### 189 2.3 Other data and impact of the background state

190 In addition to the outputs from modal decomposition, full zonal wind and temperature fields from ECMWF analyses are used  
 191 to compute the background fields based on the same N64 grid and over the same period (Jan 2007 - Jun 2013). Zonal wind  $U$   
 192 and static stability  $N$  are latitudinally averaged in the belt 5°S-5°N on all model levels to produce their zonal structure.

193 Static stability profiles are estimated through

$$194 \quad N^2 = \frac{g^2}{\Theta} \frac{\partial \Theta}{\partial \phi} \quad (6)$$

195 in units of  $s^{-2}$  and are defined on hybrid model levels on which the geopotential field  $\phi$  and the potential temperature field  $\Theta$   
 196 are derived a priori from the input data. Both fields are shown in Fig. 3.

197 The zonal wind field has the largest values on average in the TTL around 150 hPa with westerly winds peaking in the  
 198 Western Hemisphere over the Pacific Ocean and easterly winds peaking in the Eastern hemisphere over the Indian Ocean  
 199 and Indonesia. It represents a typical time-averaged outflow pattern in response to tropical convection (e.g. Fueglistaler et al.,  
 200 2009). Throughout the seasons there is a longitudinal shift of this pattern following the convective source which is most clearly  
 201 observed at 150 hPa. Such seasonal shift is visible up to 100 hPa in Fig. 3(b) where winds are weaker compared to 150 hPa.  
 202 In northern winter, zonal winds are strongest over Indonesia and the Eastern Pacific with the zonal wind maxima position and  
 203 strength similar compared to the longer ERA-40 dataset used by Suzuki and Shiotani (2008). During boreal summer easterly  
 204 winds mainly prevail over the Indian Ocean, which is linked to the Indian Monsoon season.

205 At 100 hPa, the static stability illustrates the strongest seasonal cycle with values ranging from near-tropospheric values of  
 206  $3 \times 10^{-4} \text{ ms}^{-2}$  during northern winter towards stratospheric values of  $5 - 6 \times 10^{-4} \text{ ms}^{-2}$  during boreal summer. Note also  
 207 the resolved local maxima in static stability at 80 hPa above the warm pools, known as the Tropical Inversion Layer (TIL)  
 208 and which is possibly wave-driven (Grise et al., 2010; Kedzierski et al., 2016). Figure 3(b) suggests that the TIL descends  
 209 down to 100 hPa during boreal summer months peaking over Western Pacific, in agreement with the cycle found in GPS-RO  
 210 observations by Grise et al. (2010).

---

<sup>1</sup><http://meteo.fmf.uni-lj.si/MODES/>

211 Kelvin waves are subject to wave modulation in changing background environments. Along its trajectory, the potential  
212 energy of the KW changes with varying background winds and stability which can be largely described by linear wave theory  
213 as long as waves are not near their critical level involving breaking and dissipation (Andrews et al., 1987). For simplification,  
214 KW modulation can be examined for the case of pure zonal as well as pure vertical wave propagation based on the wave  
215 modulation analysis performed by Ryu et al. (2008). A few key points on their local wave action conservation principle are  
216 summarised in the following.

217 In the tropical atmosphere, zonal modulation is the dominant process for KWs propagating in the stratosphere and in all non-  
218 easterly winds in the TTL. Vertical modulation becomes important in the presence of easterly winds within the TTL. Zonal  
219 modulation is found to affect both  $u_{kw}$  and  $T_{kw}$  components and their amplitudes are proportional to the Doppler-shifted phase  
220 speed by  $(c - U)^{1/2}$  in case of pure zonal propagation direction. This means that Kelvin waves diminish in amplitude over  
221 regions with westerly winds and become more prone to dissipative processes, while amplify over regions with easterly winds<sup>2</sup>.  
222 In case of pure vertical modulation, the change in wave potential energy mainly fluctuates with the temperature component of  
223 the Kelvin wave. Along the rays' vertical path, the waves amplitude is proportional to the Brunt-Väisälä frequency as  $\propto N^{3/2}$ ,  
224 and to the Doppler-shifted phase speed as  $\propto (c - U)^{-1/2}$ , such that  $N$  is expected to play a primary role above 120 hPa where  
225 its value starts increasing rapidly (see Fig. 3).

226 Alexander and Orland (2010) showed through wave modulation principles that temporal variations in zonal-mean  $N$  indeed  
227 are correlated with observed KW amplitudes at 16 km (approx. 100 hPa). A more extensive wave modulation analysis was  
228 described by Flannaghan and Fueglistaler (2013) using the full ray tracing equations to demonstrate that zonal winds in the TTL  
229 not only modulate Kelvin waves locally, but also create a lasting modulating effect on wave activity through ray convergence  
230 in the stratosphere. In particular, the seasonal cycle of the upper tropospheric easterlies (on average located over the western  
231 Pacific), that acts as an escape window for Kelvin waves throughout the year and largely explains the longitudinal structure of  
232 Kelvin wave zonal wind and temperature climatology.

233 We shall present the seasonal variability of tropical convection by using the Outgoing Longwave Radiation (OLR) dataset  
234 with daily outputs from the NOAA Interpolated OLR product (Liebmann and Smith, 1996). The OLR product, often used as a  
235 proxy for convection, is extracted on a  $2.5^\circ \times 2.5^\circ$  grid and interpolated on a N64 grid. Latitudinal averages are derived over  
236 larger domain, namely over  $15^\circ\text{S}$ - $15^\circ\text{N}$  since organized convection tend to happen more remote from the equator, especially  
237 during the summer monsoon season over the Asian continent.

### 238 3 Kelvin wave energetics

239 We start with a discussion of the KW energy distribution among zonal wavenumbers as given by (5), followed by seasonal  
240 differences.

---

<sup>2</sup>Keeping in mind that vertical wave propagation and consequently modulation becomes increasingly important as well wherever easterly winds are strong.



### 241 3.1 Energy distribution of Kelvin wave

242 The seasonal cycle in the energy-zonal wavenumber spectra is shown in Fig. 4 after summing up over all vertical modes. On  
243 average, energy decreases as the zonal wavenumber increases as typical for atmospheric energy spectra. As we deal with the  
244 large scales, we show only the first six zonal wavenumbers with energy values shown separately for the annual mean and the  
245 four seasons separately.

246 Figure 4 shows that largest seasonal variations in KW energy are found at the largest zonal scales. For all zonal wavenumbers,  
247 above annual-mean energy values are observed during DJF and JJA seasons while SON and MAM are below annual-mean  
248 energy. In the zonal wavenumber 1, total KW energy varies between  $200 \text{ Jkg}^{-1}$  in MAM season and somewhat over  $300 \text{ Jkg}^{-1}$   
249 in JJA. In wavenumber 2, values do not exceed  $100 \text{ Jkg}^{-1}$  and JJA still contains the largest energy. At higher wavenumbers,  
250 DJF season becomes the most energetic. In  $k > 4$ , total KW energy is under  $20 \text{ Jkg}^{-1}$  and continue to reduce with  $k$ . The slope  
251 of the KW energy spectrum is between  $-5/3$  and  $-1$  at planetary scales (not shown), similar to the spectra presented in Žagar  
252 et al. (2009) for July 2007 data. The JJA spectra has on average the steepest slope compared to other seasons, in particular the  
253 DJF spectra. The energy distribution on planetary scales is mainly associated with large-scale tropical circulation established  
254 in response to ongoing tropical convection. Therefore, the zonal distribution of tropical convection may likely play a crucial  
255 role in explaining DJF and JJA season differences of KW energy, which will be explored in next section.

### 256 3.2 Seasonal cycle of KW energy

257 Figure 5 illustrates more details on the seasonal cycle by showing KW energy time series at the largest scales represented by  
258 zonal wavenumbers  $k = 1$ ,  $k = 2$  and remaining scales  $k > 2$ . During most JJA seasons and occasionally in DJF (e.g. 2008)  
259 the total amount of KW energy in  $k = 1$  can reach up to  $600 \text{ Jkg}^{-1}$ , or twice the JJA average. The minimum in  $k = 1$  KW  
260 energy mainly occurs during October followed by April with values dropping towards  $100 \text{ Jkg}^{-1}$ , or half the SON average. The  
261 temporal pattern in  $k = 2$  is similar to the  $k = 1$  pattern, but with a less pronounced semiannual cycle with maximum values up  
262 to  $200 \text{ Jkg}^{-1}$  and minimum values towards  $30 \text{ Jkg}^{-1}$ . On zonal scales  $k > 2$ , KWs still show a semiannual cycle with highest  
263 vertically-integrated values of energy in DJF.

264 In particular, for zonal wavenumber  $k = 1$  one can distinguish intermonthly in addition to semiannual variability. Inter-  
265 monthly variability is most clearly observed during JJA, for example in July 2011 where one can distinguish six separate  
266 peaks of over  $400 \text{ Jkg}^{-1}$  energy over a period of approximately 90 days resembling an average wave period of about 18 days.  
267 These are typical periods for free propagating Kelvin waves as observed in the TTL and lower stratosphere (e.g. Randel and  
268 Wu, 2005). Note here again that our KW energy is vertically integrated over the whole model depth. This means that the ob-  
269 served intermonthly variability of KWs appears dominated by the cyclic process of free propagating KWs entering the TTL,  
270 amplifying due to changing environmental conditions, followed by wave breaking or dissipation.

271 The dominant scales of temporal variability in KWs are illustrated by a frequency spectrum of  $k = 1$  in Fig. 6. The spectrum  
272 is produced by the Fourier transform of energy time series of 6.5 years. The resulting power spectrum has been smoothed by  
273 taking the Gaussian-shaped moving averages over the raw spectrum by using the Daniell kernel three times (Shumway and

274 Stoffer, 2010). The spectrum contains a peak at 1-day period associated with the diurnal tide projecting to the Kelvin waves.  
275 After that, a gradual increase of energy is seen towards the 16-day period with multiple individual periods standing out. For  
276 periods longer than 20 days, individual peaks are found close to 25, 43 and 59 days. After that, most KW energy is contained  
277 by far in the semiannual cycle. The frequency spectrum provides a useful starting point for the discussion in the next section  
278 when the spatiotemporal patterns of KWs shall be examined in several spectral domains.

279 Returning to Fig. 5, a low-pass filter with 90 day cut-off has been applied on KW energy in order to keep only the two  
280 main spectral peaks in Fig. 6. The result is visible as the thicker black line in Fig.5 for all three zonal wavenumber groups. A  
281 semiannual cycle for all zonal wavenumbers is evident with most energy observed around January and July, while least energy  
282 is observed approximately one month after the equinoxes. During the years 2007, 2010, 2011, and 2012, more  $k = 1$  KW  
283 energy is observed during JJA compared to the follow-up DJF season. The DJF of 2009-2010 was for example above average  
284 with energy values for  $k = 1$  above  $350 \text{ Jkg}^{-1}$ .

285 The year to year differences can be explained by many coupled factors. In general, one expects the vertically-integrated KW  
286 activity to increase when background wind conditions become favorable, i.e. in the presence of easterly winds. This occurs  
287 in the TTL in relation to strong convective outflow (Garcia and Salby, 1987; Suzuki and Shiotani, 2008; Ryu et al., 2008;  
288 Flannaghan and Fueglistaler, 2013) during DJF and JJA seasons mainly. Moreover, KW activity is enhanced whenever easterly  
289 QBO winds are present down into the lower stratosphere (Baldwin and Coauthors, 2001; Alexander and Ortland, 2010) or  
290 during El Niño (Yang and Hoskins, 2013). The latter factor may partly explain a large difference in the KW energy during the  
291 El Niño DJF of 2009-2010 and the below-average energy level a year after, during the strong La Niña DJF period of 2010-  
292 2011. However, during the La Niña DJF of 2007-2008, the amount of KW energy is above normal. That season was however  
293 characterized by above-normal MJO activity which often occurs during favourable easterly QBO conditions in the stratosphere  
294 (Son et al., 2017). During 2010-2011 DJF season stratospheric winds were largely westerly thereby prohibiting KW activity.  
295 The role of these low-frequency atmospheric phenomena on KW seasonal variability is a topic of further research.

296 Finally, Fig. 5 also shows that KW activity in July 2007, previously examined by Žagar et al. (2009), was exceptionally  
297 strong. A large part of that energy, (somewhat more than half) belonged to zonal wavenumber 1. In spatiotemporal terms, it is  
298 associated with the presence of a strong dipole structure in the TTL (as in Fig.2), which is colocated with favourable easterly  
299 wind conditions in the TTL as well as in the stratosphere (not shown). In fact, at 50 hPa the QBO was just at the beginning of  
300 its westerly phase in July 2007.

## 301 **4 A spatiotemporal view on Kelvin wave seasonal variability**

### 302 **4.1 Kelvin wave decomposition among wave periods**

303 In this section, the spatiotemporal view of KWs shall be presented over three dominant ranges of wave periods in Fig. 6,  
304 namely: (i) the (semi)annual cycle using a low-pass filter with cut-off period at 90 days, (ii) the intraseasonal period using  
305 a bandpass filter over periods between 20-90 days, and finally (iii) the intramonthly period with bandpass filtered periods

306 between 3-20 days. The chosen periods, especially the intramonthly periods, are similar to those used in previous studies. In  
307 each case, mean 6-year fields as well as seasonal means shall be presented.

308 Note that our temporal filtering operates on time series of KW signals at every grid point. This is different from the commonly  
309 applied space-time filtering following Hayashi (1982) that applies KW dispersion relations. Our filtered KWs can appear  
310 stationary or even westward shifted due to westward-moving sources of the KW amplification (e.g. easterly winds, high static  
311 stability in the TTL).

312 Both KW components  $u_{kw}$  and  $T_{kw}$  are Fourier-transformed to frequency space where the spectral expansion coefficients  
313  $\chi_{kw}$  in domains outside the desired frequency ranges are put to zero. Case (i) results in KW components  $u_{kw,l}$  and  $T_{kw,l}$  where  
314  $l$  indicates the low-frequency component. Case (ii) results in  $u_{kw,m}$  and  $T_{kw,m}$  where  $m$  indicates the intramonthly period.  
315 Case (iii) results in fields  $u_{kw,h}$  and  $T_{kw,h}$  where  $h$  stands for the high-frequency component. Previous studies have defined  
316 free propagating Kelvin waves over similar ranges (3-20 days, Alexander and Ortland (2010); 4-23 days, Suzuki and Shiotani  
317 (2008)) and similarly for intraseasonal periods (23-92 days, Suzuki and Shiotani (2008)). Next, seasonal averages will be taken  
318 over the four seasons, resulting in variables  $\overline{u_{kw,l}}^s$ ,  $\overline{T_{kw,l}}^s$  for the low-frequency component and similarly for the other two  
319 cases. The superscript  $s$  represents one of the four seasons: northern winter ( $s = \text{DJF}$ ), spring ( $s = \text{MAM}$ ), summer ( $s = \text{JJA}$ ),  
320 and autumn ( $s = \text{SON}$ ).

321 Cases (ii) and (iii) contain purely subseasonal variability and therefore one can expect their 6-year means to be zero-valued  
322 since variability beyond 90 days has been put to zero. Similarly, mean fields for each of the four seasons results in  $\overline{u_{kw,h}}^s \ll$   
323  $\overline{u_{kw,l}}^s$  and  $\overline{u_{kw,m}}^s \ll \overline{u_{kw,l}}^s$  and the same for the temperature component. This reflects the fact that positive and negative  
324 phases of the fast KW responses average out to approximately zero on seasonal timescales (figure not shown). Therefore, the  
325 seasonal mean of the absolute amplitudes of the zonal wind and temperature are examined instead, i.e.  $|\overline{u_{kw,h}}^s|$ ,  $|\overline{u_{kw,m}}^s|$  and  
326 similarly for temperature. This describes seasonal fluctuations in subseasonal KW amplitudes<sup>3</sup>.

327 Figure 7 shows results for all three cases after taking mean over the whole period. The left panel resembles a dominant  
328 "wave-1" structure with zonal wind maximized around 140 hPa. Easterly KW winds are strongest around 60°E and westerly  
329 winds around the Date Line. Note that two stationary perturbations over African (30°E) and South American (80°W) orography  
330 are the result of our terrain-following NMF analysis. If one compares the KW zonal wind pattern with the climatological zonal  
331 wind pattern in Fig. 3(a) it can be observed that the zonal wind pattern is located around 20° west of the climatological pattern.  
332 Wave temperature perturbations are largest where the vertical gradients in zonal wind are largest which explains the quadrupole  
333 structure. Warm and cold KW anomalies are located at 100 hPa in the Eastern and Western hemisphere, respectively, and vice  
334 versa at 200-300 hPa.

335 The average low-frequency or seasonal KW structure has a significant resemblance with the classical Gill-type KW solution  
336 (Gill, 1980) describing a steady-state linear wave response to convective forcing. The Gill-type KW solution is characterized  
337 by westerly upper-troposphere winds east of the large-scale convective source. In responds to the seasonal cycle of convection,

---

<sup>3</sup>Most previous studies define KW activity as square amplitude rather than absolute amplitude. In our high resolution dataset we observe highly localized patterns of the KW activity in the Eastern hemisphere due to ongoing wave amplification. By using absolute amplitudes we better visualize the longitudinal structure of the KW activity in comparison to its local maxima.

338 the solution in Fig. 7a illustrates, in addition to a low-frequency KW variability in westerly winds, also a considerable low-  
339 frequency variability west of the convective outflow. This part of the signal represents the wave modulation effect of the  
340 propagating KWs on seasonal timescales.

341 The middle panel of Fig. 7 shows the average distribution of KW activity on intraseasonal timescales. The activity is largest  
342 in the Eastern hemisphere with average zonal wind maxima up to  $3 \text{ ms}^{-1}$  and temperature maxima up to 0.7 K. Zonal wind  
343 activity is largest over a broad area between 90 and 150 hPa over the Indian Ocean and the Maritime Continent. Temperature  
344 activity occurs slightly higher around 90-100 hPa. Intraseasonal activity is locally somewhat increased also around  $120^\circ\text{W}$ ,  
345 west of the Andes mountain range.

346 Finally, Fig. 7c illustrates the average distribution of intramonthly KWs. The Eastern hemisphere again makes up for the  
347 larger KW activity than the Western hemisphere, but the maximum is located more upward in comparison to the intraseasonal  
348 scales, around 80 hPa. Zonal wind activity peaks up to  $3 \text{ ms}^{-1}$  over a broad range of 70-110 hPa and temperature peaks over  
349 a more narrow area around 76 hPa (up to 0.75 K). The main area for KW activity is found over Indian Ocean region, while  
350 least wave activity is above central Pacific. Towards the stratosphere KW activity reduces and becomes more uniform along in  
351 longitudinal direction.

#### 352 4.2 Low-frequency Kelvin wave variability

353 The seasonal patterns of the low-frequency components of the KW is presented as pressure-longitudinal cross-sections along  
354 the equator (at  $0.7^\circ\text{N}$ ) of the KW seasonal means, given by  $\overline{[u_{kw,l}]^s}$  and  $\overline{[T_{kw,l}]^s}$  in Fig. 8.

355 The largest amplitudes are found during the JJA months. A strong dipole "wave-1" pattern is evident in the TTL. The  
356 strongest zonal winds are found close to 150 hPa with easterlies up to  $-12 \text{ ms}^{-1}$  centered over Indian Ocean and westerlies  
357 up to  $6 \text{ ms}^{-1}$  over the Western Pacific. Negative temperature KW anomalies at 110 hPa are strongest as well during JJA with  
358 values up to 1.5 K over Indian Ocean and annually averaged value of -0.5 K over Western Pacific.

359 During DJF, the dipole pattern has shifted more eastward and upward compared to JJA and has a more slanted structure.  
360 Easterly (westerly) KW winds are located more east over the Maritime continent (central Pacific) and are centered at 130 hPa.  
361 The upper temperature dipole pattern is found higher up at 90 hPa approximately. Values are somewhat weaker compared to  
362 NH summer with easterlies up to  $-6 \text{ ms}^{-1}$  and westerlies up to  $5 \text{ ms}^{-1}$ .

363 Finally, SON and MAM season months are transition seasons with respect to the strength and position of the KW dipole as  
364 it moves west- and downward towards JJA and east- and upward towards DJF. MAM has the weakest KW dipole with slightly  
365 stronger westerly winds up to  $5 \text{ ms}^{-1}$ .

366 The longitudinal position and the strength of the low-frequency KWs have been linked to the seasonal patterns of the back-  
367 ground winds in the TTL representing the upper level monsoon and Walker circulations (Flannaghan and Fueglistaler, 2013).  
368 The average background winds maximize at 150 hPa as shown in Fig. 3(a). In Fig. 8, one can see how the KW easterlies in the  
369 Eastern hemisphere are strongest during JJA in relation to the Indian-South Asian monsoon circulation. Background easterlies  
370 as strong as  $-30 \text{ ms}^{-1}$  are located approximately  $10^\circ$  east of the KW maximum easterlies. DJF has the strongest background

371 westerlies in relation to the upper-level circulation of the Western Pacific anticyclones. MAM shows similar background wind  
 372 patterns compared to DJF but with weaker circulation. SON shows similar patterns with JJA but with weaker winds.

373 Further details on longitudinal position and interannual variability of the low-frequency KW response at its maximum value  
 374 at 150 hPa are illustrated by the Hovmoller diagram in Fig. 9. For comparison, tropical convection is represented as well through  
 375 the OLR proxy variable averaged over 15°S-15°N latitudes. All fields have been filtered with a 90 day cut-off low-pass filter  
 376 in order to highlight the seasonality. As a result, one can observe enhanced/reduced KW activity during the same individual  
 377 seasons as seen from the timeseries in Fig. 5. Above average seasonal KW activity with stronger dipole structures occurred  
 378 during the summer of 2007 (mainly through its easterlies at 60°E) and during the winters of 2006-2007 and 2009-2010. In  
 379 these winters, El-Nino was active and a clear longitudinal eastward shift is observed in OLR, in the background circulation  
 380 (not shown), as well as in the dipole KW structure. The El-Nino winter of 2009-2010 was followed by a strong La Nina winter  
 381 with an increase in tropical convection over the Maritime continent (note: OLR values below 195 Wm<sup>-2</sup>).

382 The vertical seasonal movement of the KW dipole has been linked with the seasonal movement of the tropical tropopause  
 383 height (Flannaghan and Fueglistaler, 2013; Ryu et al., 2008). The position of the tropical tropopause height (represented by a  
 384 static stability value of  $5 \times 10^{-4} \text{ s}^{-2}$  in Fig. 8) is found at approximately 85 hPa during DJF and descends towards 100 hPa in  
 385 JJA, similar to values obtained from GPS-RO observations by Grise et al. (2010). In particular, during JJA, one can notice how  
 386 the asymmetry in the tropical tropopause height over Indian Ocean around 60°E coincides with increasing temperatures by the  
 387 KW dipole up to 1.5 K. Such deformation of the tropical tropopause is also evident during DJF and SON seasons.

388 Figures 10a and 10b illustrate seasonal-mean KW temperatures  $\overline{T_{kw,l}}^s$  in relation to the tropical tropopause layer defined  
 389 by static stability  $N^2$ . Seasonal variations in KW temperatures are colocated with the position of the tropopause, descending  
 390 down from its highest position during DJF to its lowest position during JJA. Temperature amplitudes are observed to decline  
 391 roughly above  $N^2 = 5 - 6 \times 10^{-4} \text{ s}^{-2}$ . Within this zonal-mean seasonal picture, zonal asymmetries in  $N^2$  exist and are found:  
 392 (i) near the Date Line with values of  $8 \times 10^{-4} \text{ s}^{-2}$  at 80 hPa during DJF and  $7 \times 10^{-4} \text{ s}^{-2}$  at 90 hPa during JJA and (ii) lower  
 393 at 100 hPa over the Indian Ocean during JJA. Particularly during JJA, the deformation of the zonal-mean static stability field  
 394 colocates strongly with the position of a strong KW temperature anomaly over Indian Ocean. A rough estimation is made on  
 395 the contribution of the KW anomaly to the zonal deformation of the tropopause layer by removing zonal-mean parts of both  
 396 fields. First, static stability zonal anomalies,  $\overline{N'^2}^s$ , are derived by subtracting zonal-mean values of  $N^2$  from the full  $N^2$  field  
 397 per timestep and at every pressure level, followed by seasonal averaging. Next, we can estimate the static stability change  
 398 associated with the KW anomaly, using the relation:  $N_{kw}^2 = \frac{g}{\theta} \frac{\partial \theta_{kw}}{\partial z}$ , followed by seasonal averaging as well, i.e.  $\overline{N_{kw}^2}^s$ .

399 As a result, Fig. 10c and 10d show how both static stability anomalies are overlapping. During DJF, the structure of the  
 400 zonal anomaly  $\overline{N'^2}^s$  has a positively-valued tilt eastward which stretches up to 80 hPa, while during JJA a strong static stability  
 401 anomaly is found more localized over Indian ocean region with values in the TTL up to  $\overline{N'^2}^{JJA} = \pm 0.8 \times 10^{-4} \text{ s}^{-2}$ . The  
 402 anomaly associated with the KW temperature anomaly is found to peak up to  $+0.6 \times 10^{-4} \text{ s}^{-2}$  during JJA and up to  $+0.4 \times 10^{-4}$   
 403  $\text{ s}^{-2}$  during DJF. Finally, by dividing both fields with each other, the resulting contribution of the quasi-stationary Kelvin wave  
 404 to the observed deformation of the tropical tropopause layer is estimated up to 60% during JJA and 80% during DJF.

### 405 4.3 Intraseasonal Kelvin wave variability

406 The seasonality of intraseasonal Kelvin wave variability is shown in Fig. 11 and shall be briefly discussed here. The DJF stands  
407 out as the most active season for KW activity, located mainly in the Eastern hemisphere centred at 100°E and with maximum  
408 activity at 110 hPa for zonal wind and temperature with a second maximum in temperature at 90 hPa. Values observed are up  
409 to 0.8 K for KW temperature and 5 ms<sup>-1</sup> for KW zonal wind. During MAM season, the KW activity fields are weaker but  
410 spread over a larger area in the Eastern hemisphere and in the TTL with maximum activity centered at 120 hPa (90 hPa) for  
411 the zonal wind (temperature) component. Both JJA and SON seasons have KW activity positioned at lower altitudes and more  
412 westward. In both seasons, KW zonal wind activity is split up between two structures with an eastward tilt with height; one  
413 with a maximum around 110°E and one pattern starting from 100 hPa and extending towards 60°E. Note also the increase  
414 in KW activity in the Western hemisphere below 150 hPa in the East Pacific. The maximum KW activity in the temperature  
415 component for both seasons is positioned near 100 hPa approximately on the tropical tropopause contour with value  $5 \times 10^{-4}$   
416 s<sup>-2</sup>.

417 The eastward tilted structure is observed throughout all seasons except MAM when background easterly winds are nearly  
418 absent in the Eastern hemisphere. In all other seasons one can observe how the tilted structure is locked to the background  
419 easterlies with maximum amplitudes located slightly above and west of it. Such eastward tilt with height has been frequently  
420 observed, for example over radiosonde station Medan at 100°E during the early stage of MJO development (Kiladis et al.,  
421 2005).

### 422 4.4 Intramonthly Kelvin waves

423 The seasonal variability of intramonthly Kelvin waves, represented by their absolute amplitudes  $\overline{|u'_{kw,h}|^s}$  and  $\overline{|T'_{kw,h}|^s}$ , shall  
424 be examined in relation to the background conditions. Figure 12 illustrates favorable regions for KW activity. In general, KW  
425 activity increases upward from around 120 hPa towards its zonal-mean peak value at 76 hPa. The largest values are observed  
426 in the Eastern hemisphere in region from 30°E till 150°E. The temperature component in particular has a constant maximum  
427 peak (up to 0.8 K) located around 76 hPa throughout the year, where also the largest increase in  $N^2$  occurs as shown in Fig. 3.  
428 Above 70 hPa, KW activity continuously decreases in the stratosphere.

429 The longitudinal structure of the KW zonal wind shows two distinct peaks in the TTL, one consistently located at 76 hPa and  
430 another around 100-110 hPa in the Eastern hemisphere which is mainly present during solstice seasons. The first maximum co-  
431 incides with the temperature distribution which can be explained by their balance relationships and free horizontal propagation  
432 in the stratosphere. Below the tropopause, KW activity is coupled to convective processes alternating the tropospheric vertical  
433 wave structures as discussed by Flannaghan and Fueglistaler (2012).

434 The secondary maximum around 110 hPa in Fig. 12 is present mainly during solstice seasons in the Eastern hemisphere and  
435 it is associated with the seasonal movement of the background wind. The maximum of KW wind and the background wind  
436 maximum move eastward from DJF to JJA season similar to the low-frequency variability. A day-by-day comparison of the  
437 KW activity and background wind confirms that propagating KWs amplify while approaching a region of strong easterlies,

438 forming a folding structure around it while the individual KWs dissipate towards the center of easterly winds. One can notice  
439 in Fig. 12 a fast reduction of KW amplitudes eastward of its maximum towards the center of the background easterlies. It is  
440 likely related to dissipation and wave breaking processes as observed over Indonesia (120°E) by Fujiwara et al. (2003). Within  
441 such regions, the KW-background wind interaction becomes complex and the linearity assumption breaks (Ryu et al., 2008;  
442 Flannaghan and Fueglistaler, 2013).

443 A comparison with the previous study by Suzuki and Shiotani (2008) using ERA-40 data shows that the L91 data contain  
444 stronger KW activity in the vicinity of the background easterlies in the Eastern hemisphere, and more fine-scale details which  
445 can be explained by better analyses based on more observations and improved models including increased resolution. For  
446 example, Suzuki and Shiotani (2008) used 5 levels of ERA-40 data between 50 and 200 hPa whereas the present study considers  
447 25 model levels between 50 – 200 hPa. Maxima of the KW temperature signal appear in similar locations and strength except  
448 for a small offset in vertical position (70 hPa in Suzuki and Shiotani (2008) versus 80 hPa in Fig. 12) and a larger zonal  
449 asymmetry in our results.

450 Another view of the seasonal cycle of free propagating KWs is illustrated in Fig. 13 which focuses on the spatiotemporal  
451 distribution of individual KW tracks. Hovmoller diagrams are illustrated of KW zonal wind and temperature at levels 110 and  
452 200 hPa cumulated from different years into a single calendar year along with the background zonal wind. In addition, the  
453 monthly-mean values of daily maximum KW amplitudes occurring in longitude are added on the rightside of each diagram. It  
454 represents seasonality in the KW maximum amplitudes in a similar fashion to Fig. 6 in Alexander and Ortland (2010) which is  
455 based on HIRDLS satellite data.

456 The individual wave tracks at 110 hPa illustrate KWs with amplitudes exceeding  $3 \text{ ms}^{-1}$  and 0.6 K which are propagating  
457 throughout the year in the Eastern hemisphere, during June-October months only over the Pacific, and all except DJF months in  
458 most of the Western Hemisphere. Typical wave tracks start east of the  $0^\circ$  ( $30^\circ\text{W}$ ) meridian during winter (summer) and largely  
459 disappear west of  $120^\circ\text{E}$ . The largest wave amplitudes are observed between  $50^\circ\text{E}$  and  $100^\circ\text{E}$  prior to regions of easterly winds  
460 in agreement with Fig. 12. Here presented details show that most notable waves appear during the Asian monsoon period with  
461 upper-level easterlies prevailing from June into September. The largest KW amplitudes appear confined to the June and July  
462 months followed by a rapid drop in August. In fact, a local minimum in the number of KWs as well as in wave amplitudes  
463 occurs in August before the KW activity increases slightly during autumn.

464 At 200 hPa, the favorable area for KW propagation shifts to the Western Hemisphere and large KW activity is observed west  
465 of the South American continent throughout the year (west of  $80^\circ\text{W}$ ) with a westward extension over the Pacific during JJA.  
466 Another set of wave tracks starts over equatorial South America around  $30^\circ\text{W}$  and continues till  $60^\circ\text{E}$  during JJA. During DJF  
467 these wave tracks shift more east and start at  $5^\circ\text{W}$  and continue till  $90^\circ\text{E}$ . The seasonal shifts of approximately  $30^\circ$  in KW  
468 tracks collocate with similar shifts in the prevailing TTL winds.

469 The amplitude of KWs undergoes a clear annual cycle with a small secondary peak present during DJF, as represented by the  
470 monthly-means of daily maximum amplitudes on the rightside of Fig. 13. The largest amplitudes are found at 110 hPa during  
471 JJA with monthly-mean zonal wind (temperature) values up to  $8.5 \text{ ms}^{-1}$  (1.8 K) in June. During the DJF months Kelvin  
472 waves amplify more eastward with monthly-mean zonal wind (temperature) values up to  $7.8 \text{ ms}^{-1}$  (1.6 K) in December.



473 Our result matches well with the observed seasonal pattern in maximum KW temperatures at 16km ( $\sim 100$  hPa) from the  
474 HIRDLS satellite observations (Alexander and Ortland, 2010, Fig. 6). At 200 hPa, KW amplitudes are on average lower with  
475 a yearly-averaged amplitude reduction around 55% in temperature and 35% in zonal wind.

476 The semiannual cycle in maximum amplitudes remains visible up till 70 hPa. Above 70 hPa, where the KW activity remains  
477 large in Eastern hemisphere (Fig. 12), the semiannual cycle is replaced by an interannual cycle in line with the dominant impact  
478 of the QBO.

## 479 5 Discussion and Conclusions

480 We have applied the multivariate decomposition of the ECMWF operational analyses during the period 2007-2013 when  
481 the operational data assimilation and forecasting were performed on 91 model levels. The applied normal-mode function  
482 decomposition provides simultaneously the wind components, geopotential height and temperature perturbations of Kelvin  
483 waves for many scale without any prior data filtering. The three-dimensional Kelvin wave structure in the upper troposphere  
484 and lower stratosphere is composed of Kelvin wave solutions of 60 linearized shallow-water equation systems on the sphere  
485 with equivalent depths from 10 km up to about 3 meters. As the KW meridional wind component is very small it is not discussed  
486 here. We showed that large-scale KWs readily persist in the data despite analyzing selected processing times independently.

487 The KW is a normal mode of the global atmosphere and our 3D-orthogonal decomposition allows quantification of its  
488 contribution to the global energy spectrum and variability. We have presented the total (kinetic+potential) energy of KWs in  
489 the L91 data as a function of the zonal wavenumber in different seasons. The zonal wavenumber  $k = 1$  contains the largest  
490 portion of KW energy in all seasons. There is almost one third more energy in JJA than in MAM in  $k = 1$ . In  $k = 2$  there is  
491 50% less energy than in  $k = 1$  but JJA still contains most energy. In all larger zonal wavenumbers, the most energetic season is  
492 DJF.

493 We focused on the spatiotemporal features of the KW temperature and zonal wind components in the four seasons. The  
494 Kelvin wave seasonal cycle in the tropical tropopause layer (TTL) was compared with seasonal variability of the Outgoing  
495 Longwave Radiation (OLR), and the background wind and stability fields, which are believed to play an important role for  
496 the KW variability. Our results of the seasonal KW variability complement previous studies which applied different methods  
497 for the KW filtering and different datasets. The frequency spectrum has revealed a semiannual cycle as well as intraseasonal  
498 and intramonthly variability. Three ranges of wave periods were analyzed: 3-20 days, 20-90 days and longer than 90 days.  
499 This choice was partly deliberate in order to compare our results with several previous studies of KW variability. First we  
500 demonstrated that the low-frequency KW dipole pattern in the TTL, with westerly winds in the Western hemisphere and  
501 with easterly winds in the Eastern hemisphere, partly resembles a seasonal-averaged Gill-type "wave-1" pattern and contains  
502 partly low-frequency modulation of vertically-propagating KWs. The quadrature-shaped temperature component represents a  
503 thermally adjusted pattern with respect to the zonal wind component, and contributes to seasonal warming above 100 hPa in the  
504 Western and cooling in the Eastern hemisphere. The largest KW amplitudes are observed during JJA and DJF seasons. From  
505 boreal summer towards winter, KW perturbations moves eastward (from Indian Ocean basin towards Maritime Continent) and

506 upward (e.g. zonal wind component moves up from 150 hPa towards 120 hPa). The KW zonal wind amplitude varies between  
507 12 m/s strong easterlies over Indian ocean near 150 hPa in JJA to 6 m/s over Western Pacific. Over Indian Ocean in JJA, the  
508 KW easterlies thus make almost half of the total wind vector. The associated KW temperature perturbations are from 1.5 K  
509 over Indian ocean in JJA to -0.5 K over West Pacific. The zonal modulation of Kelvin waves is found to be locked with respect  
510 to the seasonal movement of convection and the convective outflow in the TTL. The modulation effect is strongest for the  
511 low-frequency Kelvin waves during the summer monsoon season, when strong easterly winds are present at 150 hPa, resulting  
512 in the largest KW zonal wind and temperature anomalies, of which the latter results in deformation of the tropical tropopause  
513 over Indian Ocean.

514 Intraseasonal (periods 20-90 days) activity is strongest in DJF with maxima up to 0.8 K for KW temperature and up to 5 m/s  
515 for KW zonal wind centred at 120°E. Both temperature and zonal wind activities have eastward tilt with height. In comparison  
516 to previous study by Suzuki and Shiotani (2008) using ERA-40 data, the slanted structure in the present data continues to  
517 extend more upward and eastward which is likely due to the increased number of vertical model levels compared to ERA-40.  
518 The importance of vertical model resolution for the KW structure and amplitude was demonstrated in Žagar et al. (2012) and  
519 Podglajen et al. (2014).

520 For periods 3 – 20 days, the seasonal cycle of KWs is clearly seen in the wave amplitude. In the zonal-mean perspective, the  
521 largest amplitudes are located between 70 and 100 hPa for both zonal wind and temperature but it is modulated by the seasonal  
522 movement of the TTL. A major zonal asymmetry was found in KW activity: around 110 hPa the Kelvin wave undergoes  
523 amplification mainly in the Eastern hemisphere during the solstice seasons, while at 200 hPa a secondary region of the KW  
524 amplification occurs in the Western hemisphere during boreal summer. The intermonthly KWs show largest amplitudes in the  
525 vicinity of the strongest easterlies preferably west and above the centre of easterlies. The applied novel methodology makes it  
526 possible to observe such dynamics on daily basis whenever easterlies are strong in the TTL. Nearly real-time representation of  
527 the KW activity is available on <http://modes.fmf.uni-lj.si>.

528 In summary, our seasonal variability analysis shows that the background wind in the TTL linked with convective outflows,  
529 play a dominant role in the longitudinal position where the zonal modulation of Kelvin waves is preferred, while the tropical  
530 tropopause and its seasonal vertical movement determine the vertical extent of the KW modulation processes.

531 *Acknowledgements.* This study was funded by the European Research Council (ERC), Grant Agreement no. 280153, MODES. We are  
532 grateful to Dr George Kiladis and an anonymous reviewer for their detailed constructive comments.

533 **References**

- 534 Alexander, M. J. and Ortland, D. A.: Equatorial waves in High Resolution Dynamics Limb Sounder (HIRDLS) data, *J. Geophys. Res.*, 115,  
535 D24 111, <https://doi.org/10.1029/2010JD014782>, 2010.
- 536 Andrews, D. G., Holton, J. R., and Leovy, C. B.: *Middle atmospheric dynamics*, Academic Press, 1987.
- 537 Baldwin, M. P. and Coauthors: The Quasi-Biennial Oscillation, *Rev. Geophys.*, 39, 179–229, 2001.
- 538 Boyd, J. P.: The Effects of Latitudinal Shear on Equatorial Waves. Part II: Applications to the Atmosphere, *J. Atmos. Sci.*, 35, 2259–2267,  
539 1978.
- 540 Boyd, J. P.: *Dynamics of the Equatorial Ocean*, Springer-Verlag GmbH Germany 2018, 2018.
- 541 Boyd, J. P. and Zhou, C.: Uniform Asymptotics for the Linear Kelvin Wave in Spherical Geometry, *J. Atmos. Sci.*, 65, 655–660,  
542 <https://doi.org/10.1175/2007JAS2356.1>, 2008.
- 543 Ern, M. and Preusse, P.: Wave fluxes of equatorial Kelvin waves and QBO zonal wind forcing derived from SABER and ECMWF temperature  
544 space-time spectra, *Atmos. Chem. Phys.*, 9, 3957–3986, 2009.
- 545 Ern, M., Preusse, P., Krebsbach, M., Mlynarczyk, M. G., and Russell, J. M.: Equatorial wave analysis from SABER and ECMWF temperatures,  
546 *Atmos. Chem. Phys.*, 8, 845–869, 2008.
- 547 Flannaghan, T. J. and Fueglistaler, S.: Tracking Kelvin waves from the equatorial troposphere into the stratosphere, *J. Geophys. Res.*, 117,  
548 <https://doi.org/10.1029/2012JD017448>, d21108, 2012.
- 549 Flannaghan, T. J. and Fueglistaler, S.: The importance of the tropical tropopause layer for equatorial Kelvin wave propagation, *J. Geophys.*  
550 *Res.*, 118, 5160–5175, 2013.
- 551 Fueglistaler, S., Dessler, A. E., Dunkerton, T. J., Folkins, I., Fu, Q., and Mote, P. W.: Tropical tropopause layer, *Reviews of Geophysics*, 47,  
552 <https://doi.org/10.1029/2008RG000267>, 2009.
- 553 Fujiwara, M., Yamamoto, M. K., Hashiguchi, H., and Horinouchi, T.: Turbulence at the tropopause due to breaking Kelvin waves observed  
554 by the Equatorial Atmosphere Radar, *Geophysical Research Letters*, 30, 1171, <https://doi.org/10.1029/2002GL016278>, 2003.
- 555 Garcia, R. R. and Salby, M. L.: Transient response to localized episodic heating in the Tropics. Part II: Far-field behavior, *J. Atmos. Sci.*, 44,  
556 499–530, 1987.
- 557 Garcia, R. R., Lieberman, R., Russell III, J. M., and Mlynarczyk, M. G.: Large-scale waves in the mesosphere and lower thermosphere observed  
558 by SABER, *J. Atmos. Sci.*, 62, 4384–4399, <https://doi.org/10.1175/JAS3612.1>, 2005.
- 559 Gill, A. E.: Some simple solution for heat-induced tropical circulation, *Quart. J. Roy. Meteor. Soc.*, 106, 447–462, 1980.
- 560 Gill, A. E.: *Atmosphere-Ocean Dynamics*, Academic Press, New York, 1982.
- 561 Grise, K. M., Thompson, D. W. J., and Birner, T.: A global survey of static stability in the stratosphere and upper troposphere, *J. Climate*, 23,  
562 2275–2292, 2010.
- 563 Hayashi, Y.: Space-time spectral analysis and its applications to atmospheric waves, *J. Meteor. Soc. Japan*, 60, 156–171, 1982.
- 564 Highwood, E. J. and Hoskins, B. J.: The tropical tropopause, *Q.J.R. Meteorol. Soc.*, 124, 1579–1604, 1998.
- 565 Holton, J. R. and Lindzen, R. S.: An updated theory for the quasi-biennial cycle of the tropical stratosphere, *J. Atmos. Sci.*, 29, 1076–1080,  
566 1972.
- 567 Kasahara, A.: Normal modes of ultralong waves in the atmosphere, *Mon. Wea. Rev.*, 104, 669–690, 1976.
- 568 Kasahara, A.: Effect of zonal flows on the free oscillations of a barotropic atmosphere, *J. Atmos. Sci.*, 37, 917–929. Corrigendum, *J. Atmos.*  
569 *Sci.*, 38 (1981), 2284–2285, 1980.

570 Kasahara, A. and Puri, K.: Spectral representation of three-dimensional global data by expansion in normal mode functions, *Mon. Wea. Rev.*,  
571 109, 37–51, 1981.

572 Kedzierski, R. P., Matthes, K., and Bumke, K.: The tropical tropopause inversion layer: variability and modulation by equatorial waves,  
573 *Atmos. Chem. Phys.*, 16, 11 617–11 633, <https://doi.org/10.5194/acp-16-11617-2016>, 2016.

574 Kiladis, G. N., Straub, K. H., and Haertel, P. T.: Zonal and vertical structure of the Madden–Julian Oscillation, *J. Atmos. Sci.*, 62, 2790–2809,  
575 <https://doi.org/10.1175/JAS3520.1>, 2005.

576 Liebmann, B. and Smith, C. A.: Description of a complete (interpolated) outgoing longwave radiation dataset, *Bull. Am. Meteorol. Soc.*, 77,  
577 1275–1277, 1996.

578 Lin, J.-L. and Coauthors: Tropical intraseasonal variability in 14 IPCC AR4 climate models. Part I: Convective signals, *J. Climate*, 19,  
579 2665–2690, 2006.

580 Matsuno, T.: Quasi-geostrophic motions in the equatorial area, *J. Meteor. Soc. Japan.*, 44, 25–43, 1966.

581 Podglajen, A., Hertzog, A., Plougonven, R., and Žagar, N.: Assessment of the accuracy of (re)analyses in the equatorial lower stratosphere,  
582 *J. Geophys. Res. Atmos.*, 119, 11 166–11 188, <https://doi.org/10.1002/2014JD021849>, 2014.

583 Randel, W. J. and Wu, F.: Kelvin wave variability near the equatorial tropopause observed in GPS radio occultation measurements, *J.*  
584 *Geophys. Res.*, 105(D12), 15 509–15 523, <https://doi.org/10.1029/2000JD900155>, 2005.

585 Ratnam, M. V., Tsuda, T., Kozu, T., and Mori, S.: Long-term behavior of the Kelvin waves revealed by CHAMP/GPS RO measurements and  
586 their effects on the tropopause structure, *Ann. Geophys.*, 24, 1355–1366, 2006.

587 Ryu, J.-H., Lee, S., and Son, S.-W.: Vertically propagating Kelvin Waves and tropical tropopause variability, *J. Atmos. Sci.*, 65, 1817–1837,  
588 2008.

589 Salby, M. L. and Garcia, R. R.: Transient response to localized episodic heating in the tropics. Part I: Excitation and short-time near-field  
590 behavior, *J. Atmos. Sci.*, 44, 458–498, 1987.

591 Shumway, R. and Stoffer, D.: Time series analysis and its applications: with R examples, Springer texts in statistics, Springer New York,  
592 <https://doi.org/https://books.google.si/books?id=dbS5IQ8P5gYC>, 2010.

593 Son, S.-W., Lim, Y., Yoo, C., Hendon, H. H., and Kim, J.: Stratospheric Control of the Madden–Julian Oscillation, *Journal of Climate*, 30,  
594 1909–1922, <https://doi.org/10.1175/JCLI-D-16-0620.1>, 2017.

595 Suzuki, J. and Shiotani, M.: Space-time variability of equatorial Kelvin waves and intraseasonal oscillations around the tropical tropopause,  
596 *J. Geophys. Res.*, 113, D16 110, <https://doi.org/10.1029/2007JD009456>, 2008.

597 Tindall, J. C., Thuburn, J., and Highwood, E. J.: Equatorial waves in the lower stratosphere. II: Annual and interannual variability, *Q.J.R.*  
598 *Meteorol. Soc.*, 132, 195–212, <https://doi.org/10.1256/qj.04.153>, 2006.

599 Tsai, H.-F., Tsuda, T., Hajj, G., Wickert, J., and Aoyama, Y.: Equatorial Kelvin waves observed with GPS occultation measurements (CHAMP  
600 and SAC-C), *J. Meteor. Soc. Japan.*, 82, 397–406, 2004.

601 Žagar, N., Andersson, E., and Fisher, M.: Balanced tropical data assimilation based on a study of equatorial waves in ECMWF short-range  
602 forecast errors, *Q.J.R. Meteorol. Soc.*, 131, 987–1011, <https://doi.org/10.1256/qj.04.54>, 2005.

603 Žagar, N., Andersson, E., Fisher, M., and Untch, A.: Influence of the quasi-biennial oscillation on the ECMWF model short-range forecast  
604 errors in the tropical stratosphere, *Q. J. R. Meteorol. Soc.*, 133, 1843–1853, 2007.

605 Žagar, N., Tribbia, J., Anderson, J. L., and Raeder, K.: Uncertainties of estimates of inertia-gravity energy in the atmosphere. Part II: Large-  
606 scale equatorial waves, *Mon. Wea. Rev.*, 137, 3858–3873, Corrigendum: 138:2476–2477, 2009.

607 Žagar, N., Terasaki, K., and Tanaka, H. L.: Impact of the vertical resolution of analysis data on the estimates of large-scale inertio-gravity  
608 energy, *Mon. Wea. Rev.*, 140, 2297–2307, 2012.

609 Žagar, N., Kasahara, A., Terasaki, K., Tribbia, J., and Tanaka, H.: Normal-mode function representation of global 3D datasets: Open-access  
610 software for the atmospheric research community, *Geosci. Model Dev.*, 8, 1169–1195, 2015.

611 Wallace, J. M. and Gousky, V. E.: Observational evidence of Kelvin waves in the tropical stratosphere, *J. Atmos. Sci.*, 25, 900–907, 1968.

612 Wheeler, M. and Kiladis, G. N.: Convectively coupled equatorial waves: Analysis of clouds and temperature in the wavenumber-frequency  
613 domain, *J. Atmos. Sci.*, 56, 374–399, 1999.

614 Yang, G.-Y. and Hoskins, B. J.: ENSO impact on Kelvin Waves and associated tropical convection, *J. Atmos. Sci.*, 70, 3513–3532, 2013.

615 Yang, G.-Y., Hoskins, B. J., and Slingo, J.: Convectively coupled equatorial waves: A new methodology for identifying wave structures in  
616 observational data, *J. Atmos. Sci.*, 60, 1637–1654, 2003.

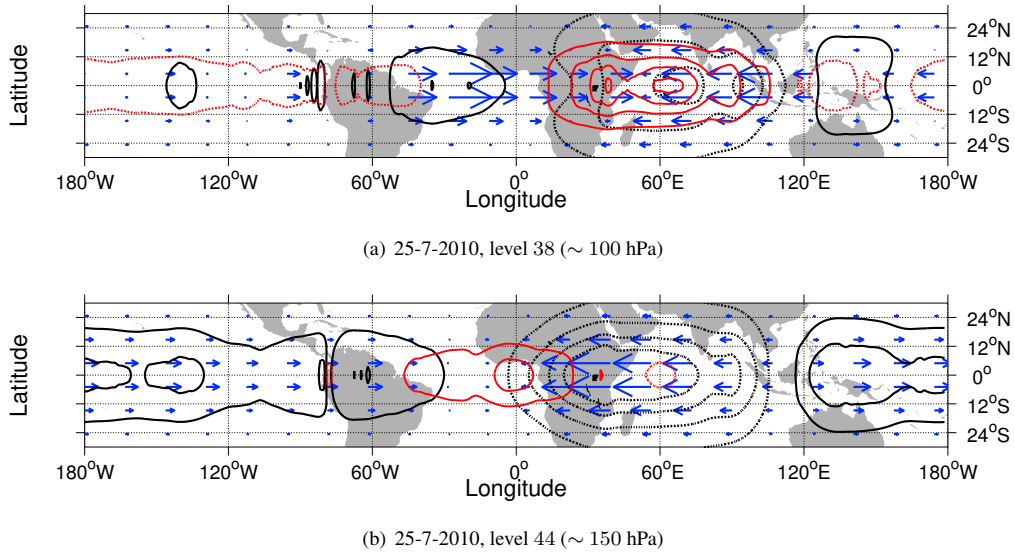


**Figure 1.** The horizontal structure of Kelvin waves in the ECMWF analysis data on 25 July 2010 at (a) 100 hPa and (b) 150 hPa. The geopotential height perturbations ( $h_{kw}$ ) are shown by black contours, every 20 m, whereas temperature perturbations ( $T_{kw}$ ) are in coloured red, every 1 K). Dashed contours represent negative and full line positive perturbations. Zero lines are omitted.

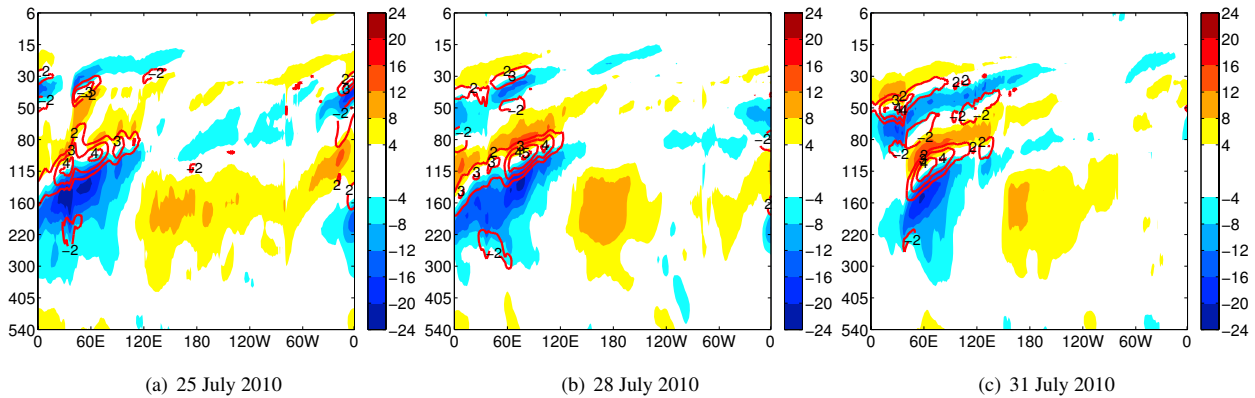


**Figure 2.** Longitude-pressure cross-section of the Kelvin wave zonal wind (red-blue shaded contours) and temperature (red contours) perturbations along  $0.7^\circ\text{N}$  on (a) 25 July, (b) 28 July and (c) 31 July 2010. Temperature is shown every 1 K, starting at 2 K. Zonal winds are drawn every  $4 \text{ ms}^{-1}$ . Zero lines are omitted.

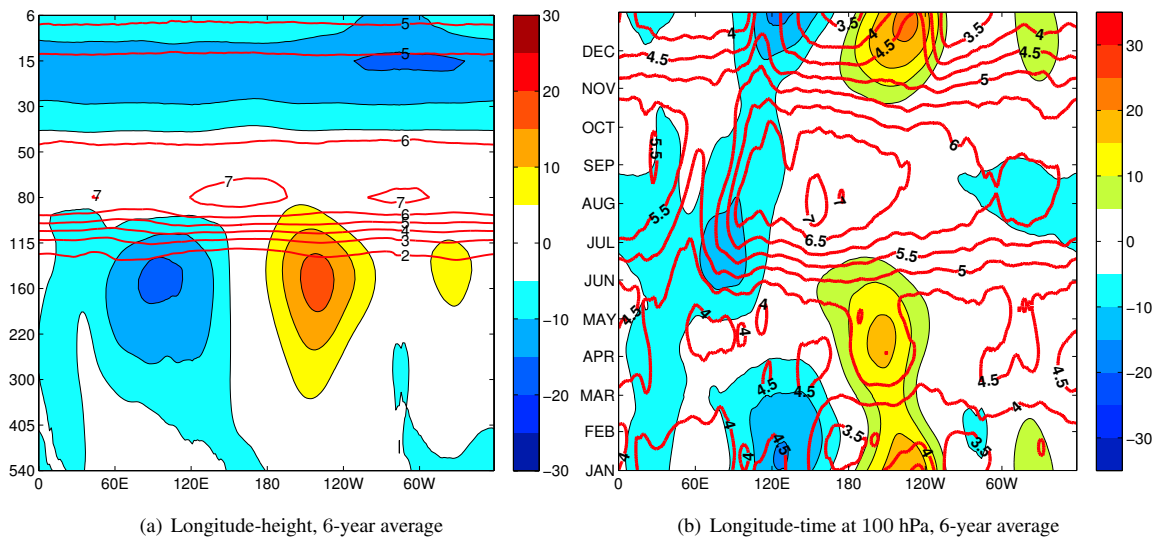


**Figure 3.** Six-year average of the zonal wind and static stability fields of the ECMWF operational analyses. Both fields are latitudinally averaged over  $5^{\circ}\text{S}$ - $5^{\circ}\text{N}$ , and have been low-pass filtered a priori with a cut-off period of 90 days to highlight seasonal variability. (a) Longitude-height section and (b) Longitude-time section at 100 hPa. Zonal winds are coloured by blue-to-red contours, each  $5 \text{ ms}^{-1}$  whereas static stability is shown in red contours, each (a)  $1 \times 10^{-4} \text{ s}^{-2}$  and (b)  $0.5 \times 10^{-4} \text{ s}^{-2}$ . Zero lines are omitted.



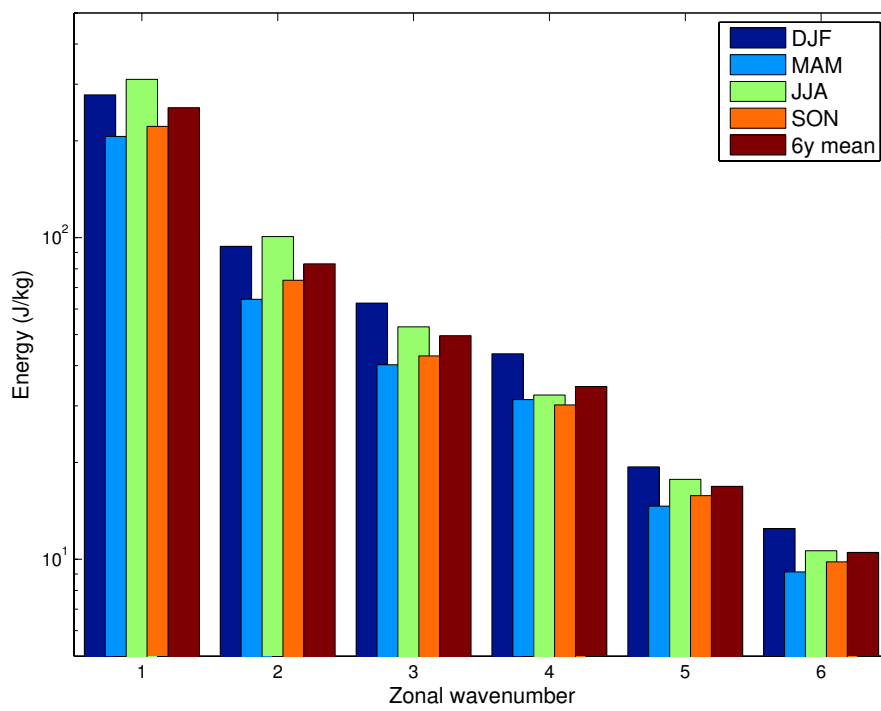
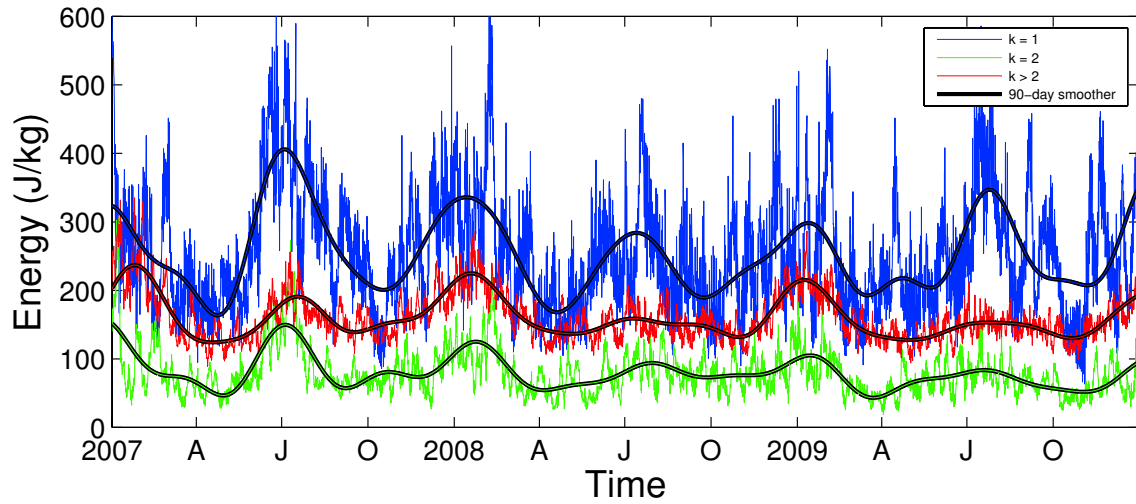
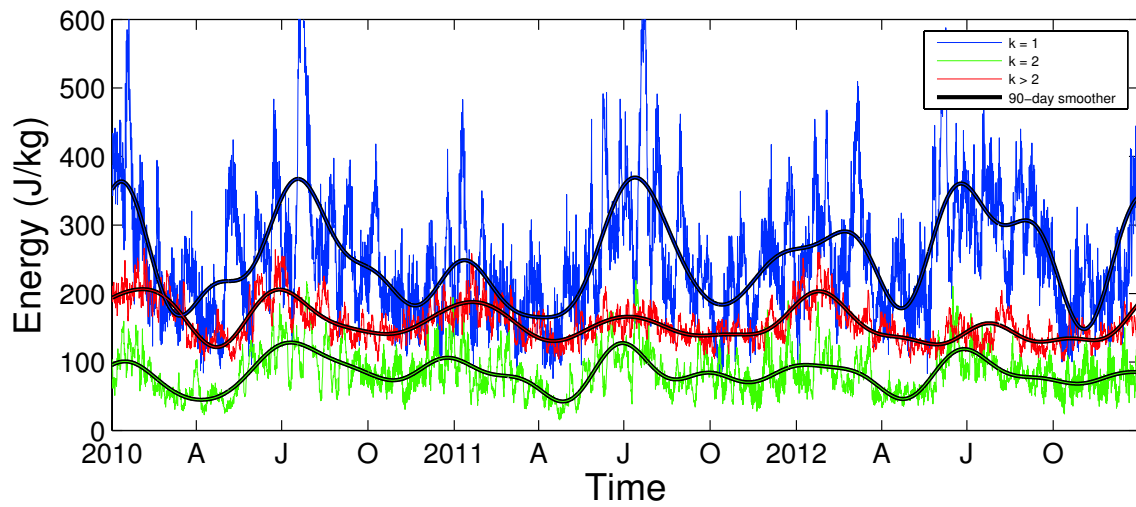


**Figure 4.** Kelvin wave energy (in  $\text{Jkg}^{-1}$ ) as function of the zonal wavenumber  $k$  for  $k = 1 - 6$ . For each  $k$ , seasonal averages are shown along with the total average as described by the legend. Energy is vertically integrated over 60 vertical modes. Further details are in the text.



(a) 2007 – 2009



(b) 2010 – 2012

**Figure 5.** Timeseries of the global total KW energy for various zonal wavenumbers over the following periods: (a) 2007 – 2009 and (b) 2010 – 2012. Labels on the x-axis 'A', 'J' and 'O' refer to the first days of April, July and October, respectively. Presented are the zonal wavenumbers  $k = 1$  (blue line),  $k = 2$  (green line) and all smaller zonal scales,  $k > 2$  (red line). A 90-day low-pass filter has been applied (black lines) for each time series in order to filter out high-frequency variability and to highlight seasonal variability.

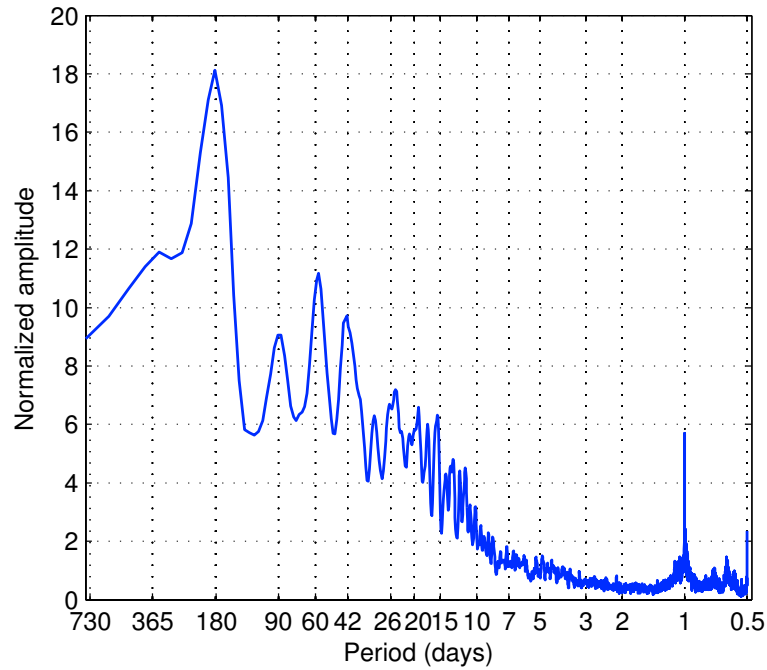


**Figure 6.** Kelvin wave frequency spectrum for the zonal wavenumber  $k = 1$ . The 1-2-1 filter with a Daniell kernel has been used to smooth the initial raw power spectra.

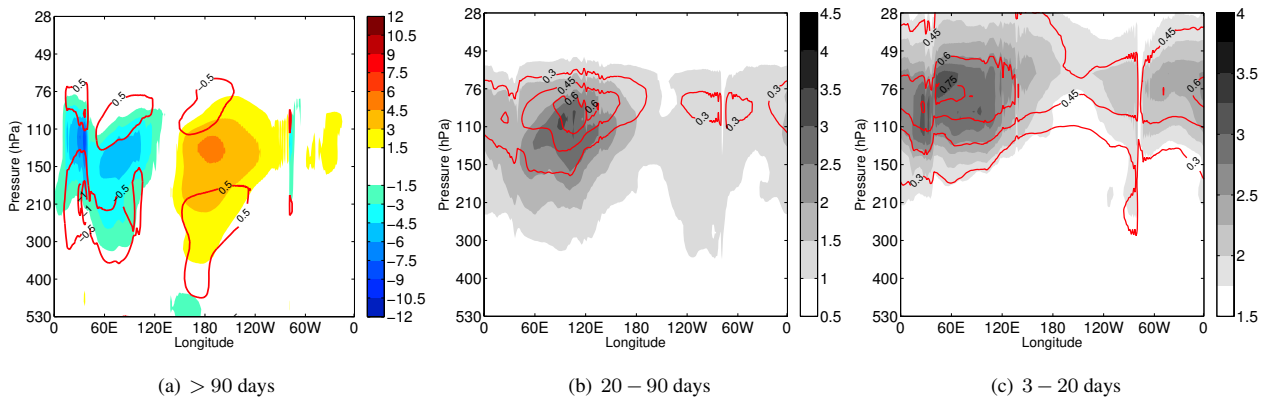


**Figure 7.** Longitude-pressure sections along  $0.7^\circ\text{N}$  of the KW zonal wind and temperature averaged over the 6-year period for: (a) low-frequency, (b) intraseasonal, and (c) intramonthly periods. The contouring is as follows: (a) zonal wind is coloured each  $1.5 \text{ ms}^{-1}$  and temperature is shown by red contours each  $0.5 \text{ K}$ , with zero lines omitted, (b) absolute amplitudes of the zonal wind and temperature are shown in grey shades each  $0.5 \text{ ms}^{-1}$  and red contours, each  $0.15 \text{ K}$ , respectively, and (c) absolute amplitudes of the zonal wind are in grey shades each  $0.25 \text{ ms}^{-1}$  and of temperature in red contours each  $0.15 \text{ K}$ .

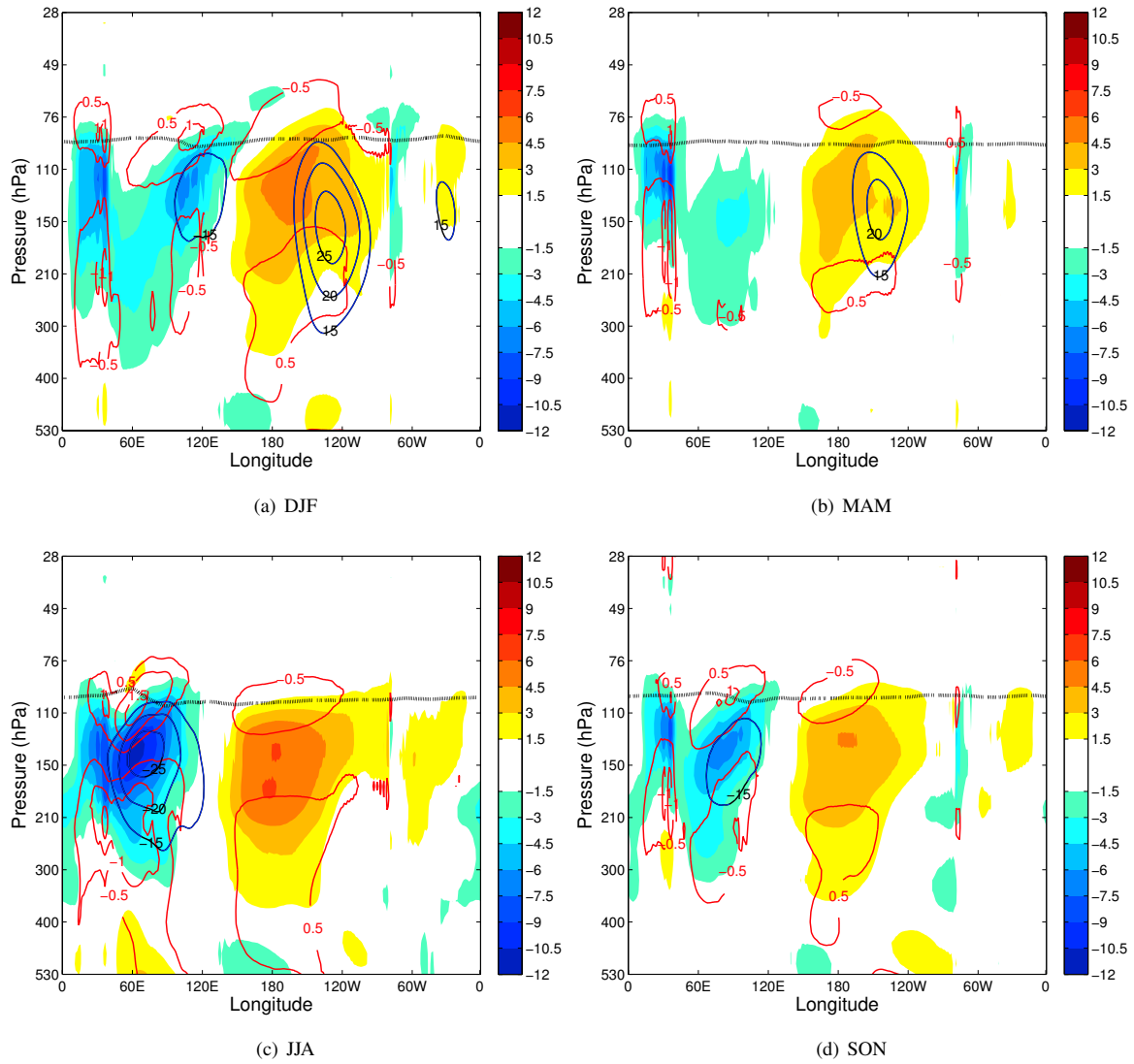


**Figure 8.** Seasonally averaged longitude-pressure sections of the Kelvin wave zonal wind (blue-to-red colour-filled contours) and temperature (red contours) along  $0.7^\circ\text{N}$ . (a) DJF, (b) MAM, (c) JJA and (d) SON. Contouring of the KW signal is the same as in Fig. 7(a). A single static stability contour with value  $5 \times 10^{-4} \text{ s}^{-2}$  is shown as a thick dotted black line to represent the seasonal movement of the tropical tropopause height. The average background zonal wind is shown by blue contours (each  $5 \text{ ms}^{-1}$ , starting from  $15 \text{ ms}^{-1}$ ). The background zonal wind and stability fields are latitudinally-averaged over  $5^\circ\text{S}$ - $5^\circ\text{N}$ . All fields are smoothed using a low-pass filter with the cut-off period of 90 days.

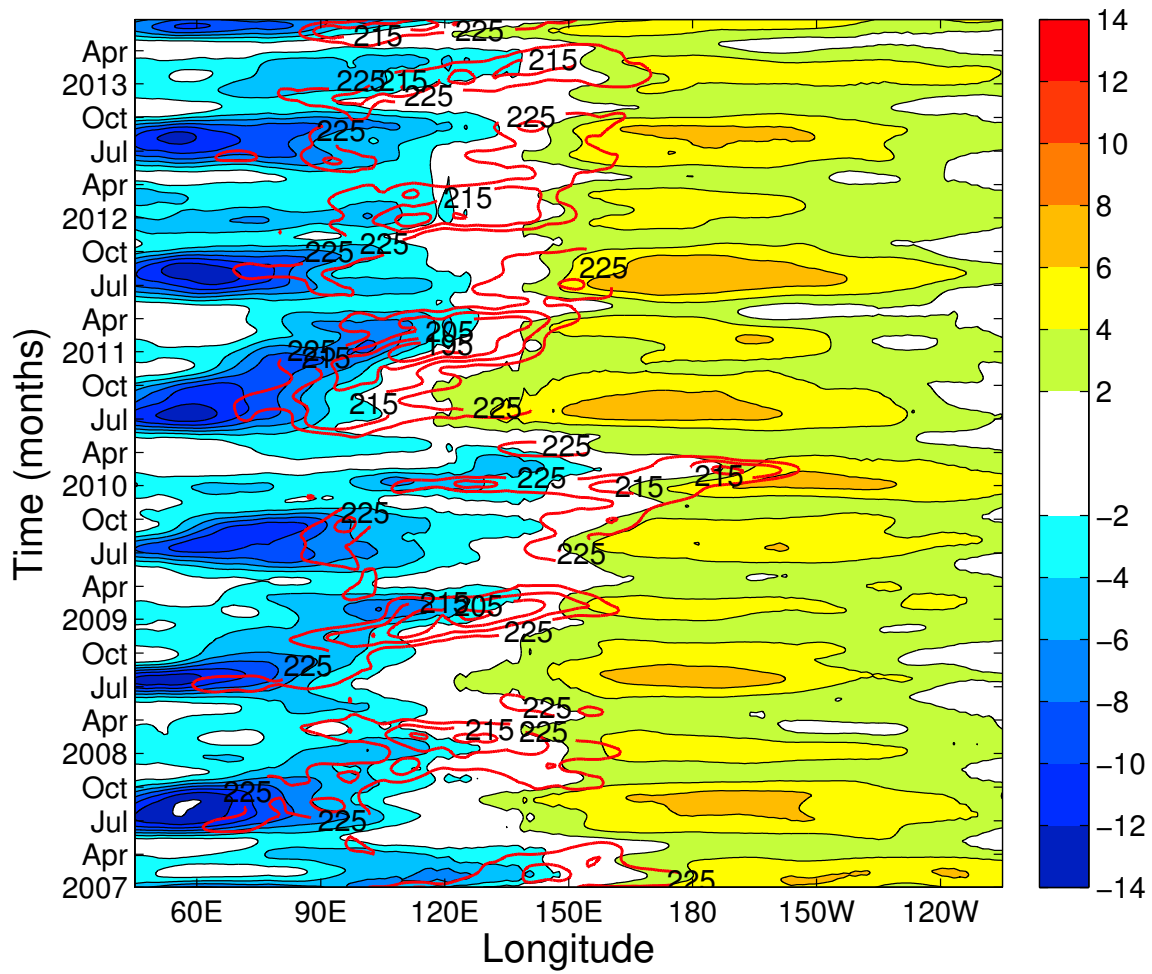


**Figure 9.** Longitude-time section at model level 45 ( $\sim 153$  hPa) of the Kelvin wave zonal wind along  $0.7^\circ\text{N}$  (blue to red shaded contours every  $2\text{ ms}^{-1}$  with zero line omitted) and the Outgoing Longwave Radiation averaged over the latitude belt  $15^\circ\text{S}$ - $15^\circ\text{N}$  (red contours each  $10\text{ Wm}^{-2}$  starting at  $225\text{ Wm}^{-2}$ ). Both fields have been filtered a priori using a low-pass filter with the cut-off period of 90 days.

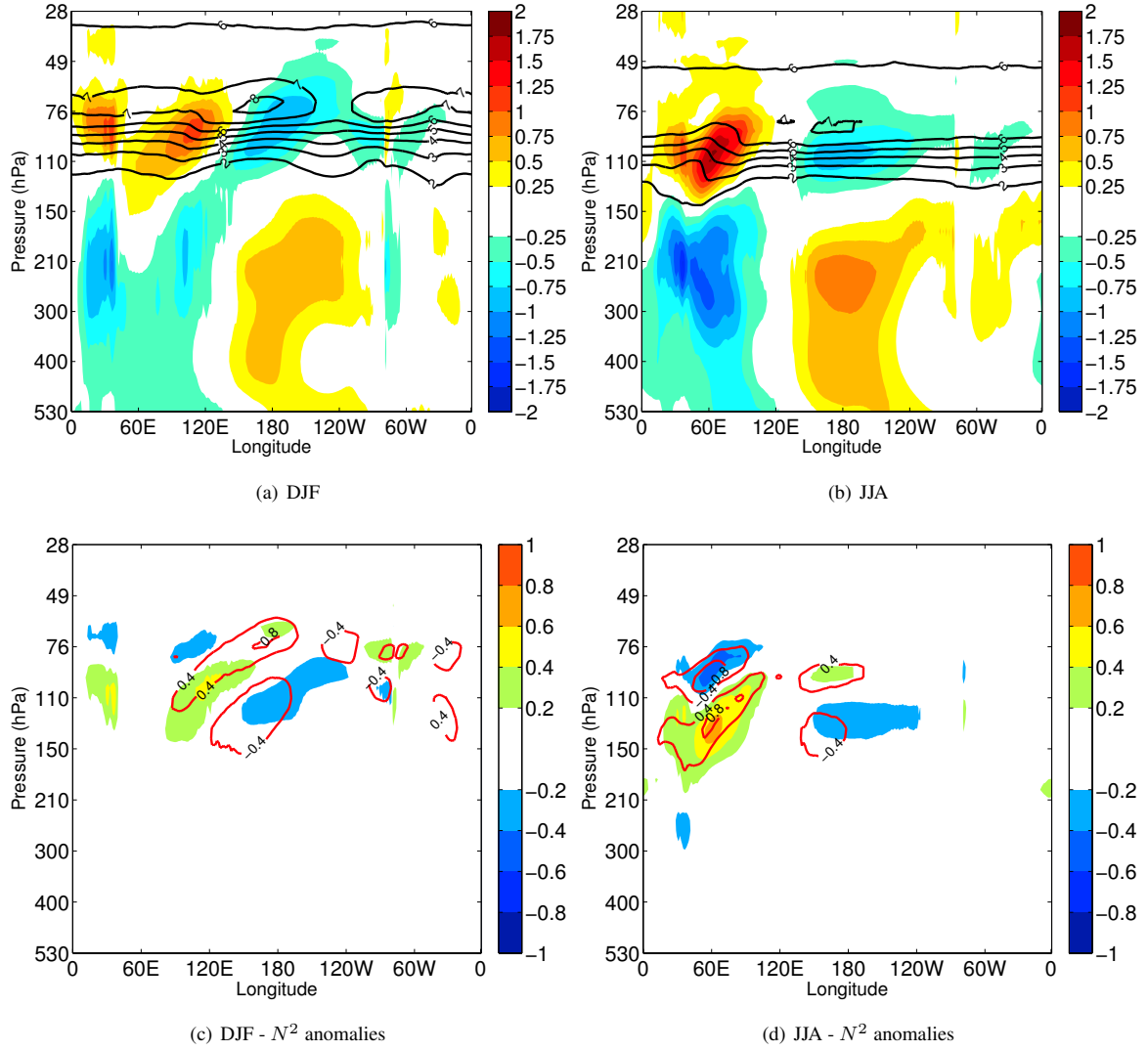


**Figure 10.** Seasonally averaged longitude-pressure sections for (a and c) DJF and (b and d) JJA. (a-b) KW temperature,  $\overline{T_{kw}}^s$ , (blue-to-red shades every 0.25 K) and static stability field,  $\overline{N^2}^s$  (black contours, each  $1 \times 10^{-4} \text{ s}^{-2}$ , starting at  $2 \times 10^{-4} \text{ s}^{-2}$ ). (c-d) KW static stability anomaly,  $\overline{N_{kw}^2}^s$  (blue-to-red, each  $0.2 \times 10^{-4} \text{ s}^{-2}$ ), and static stability anomaly with respect to the zonal mean,  $\overline{N^2}^s$  (red contours, each  $0.4 \times 10^{-4} \text{ s}^{-2}$ ).

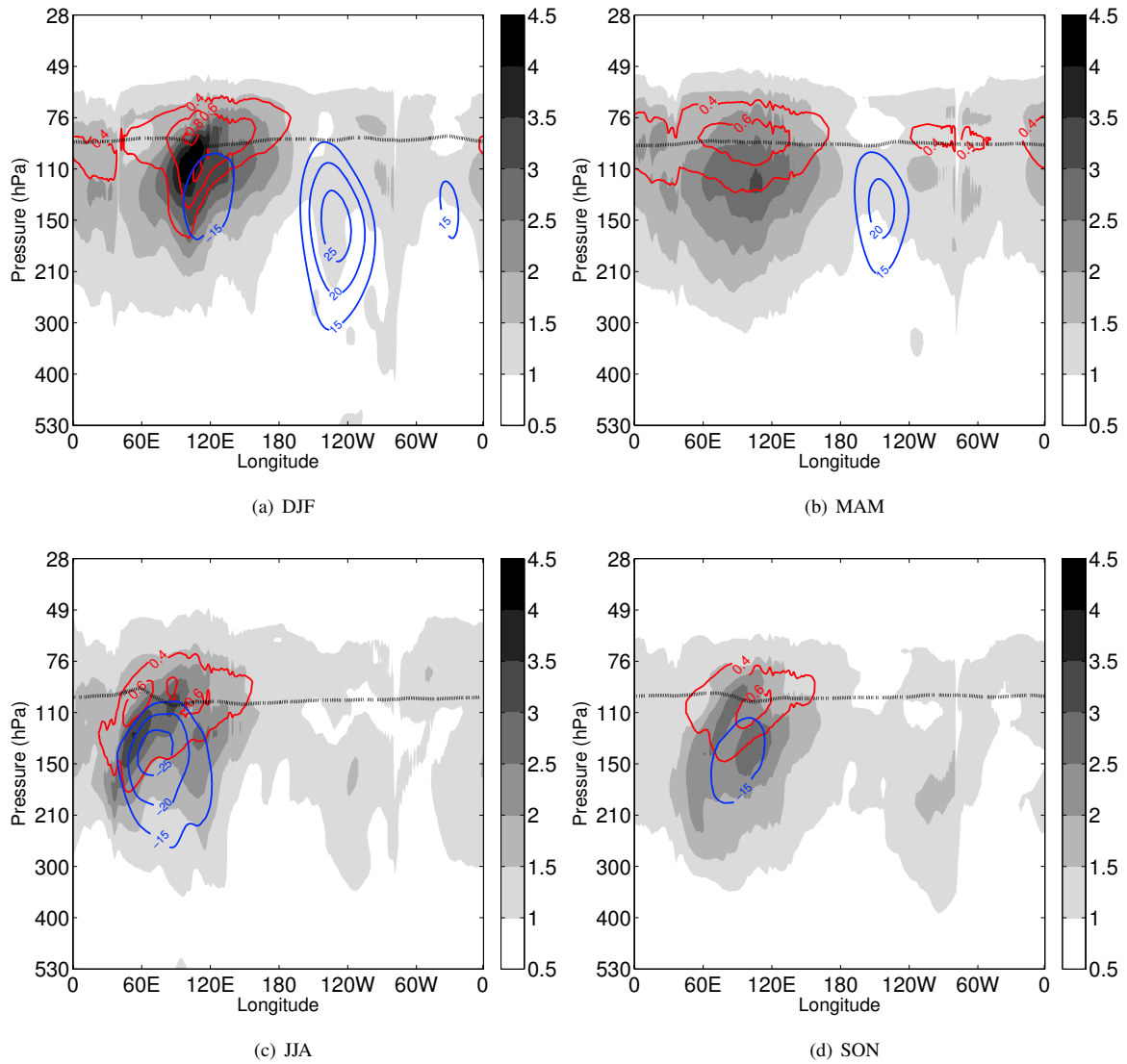


**Figure 11.** Seasonally averaged longitude-pressure sections along  $0.7^\circ\text{N}$  of the intraseasonal Kelvin wave zonal wind (white-to-black shades, each  $0.5 \text{ ms}^{-1}$ ) and temperature (red contours, each  $0.2 \text{ K}$ ). (a) DJF, (b) MAM, (c) JJA and (d) SON. The averaging is performed for the absolute values of both zonal wind and temperature perturbations. The background zonal wind (shown by blue contours) and the tropical tropopause height (single thick dotted contour) are defined as in Fig. 8.

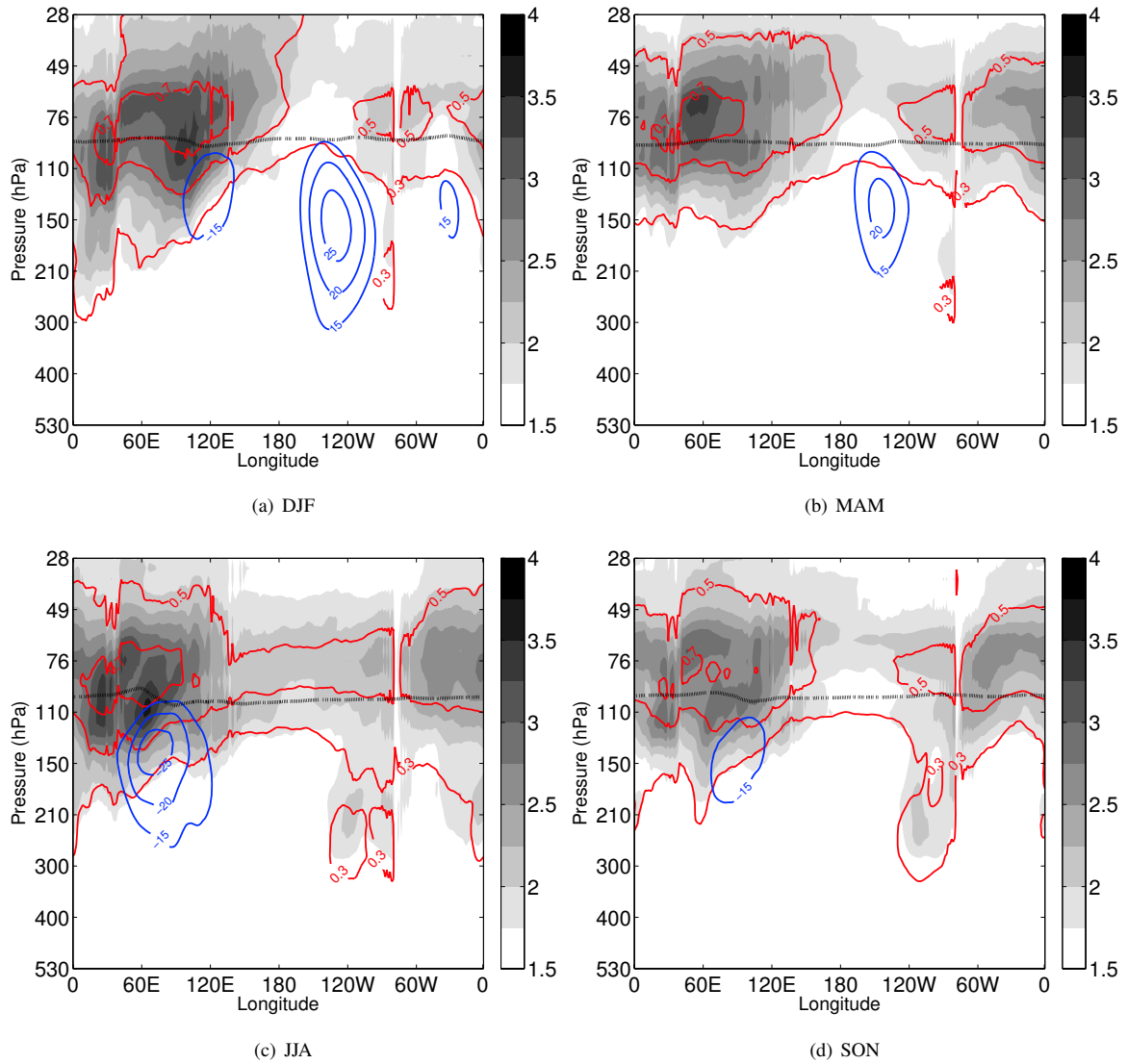


**Figure 12.** As in Fig. 11 but for the intramonthly Kelvin waves. The zonal wind (white-to-black shades) is drawn every  $0.25 \text{ ms}^{-1}$ .



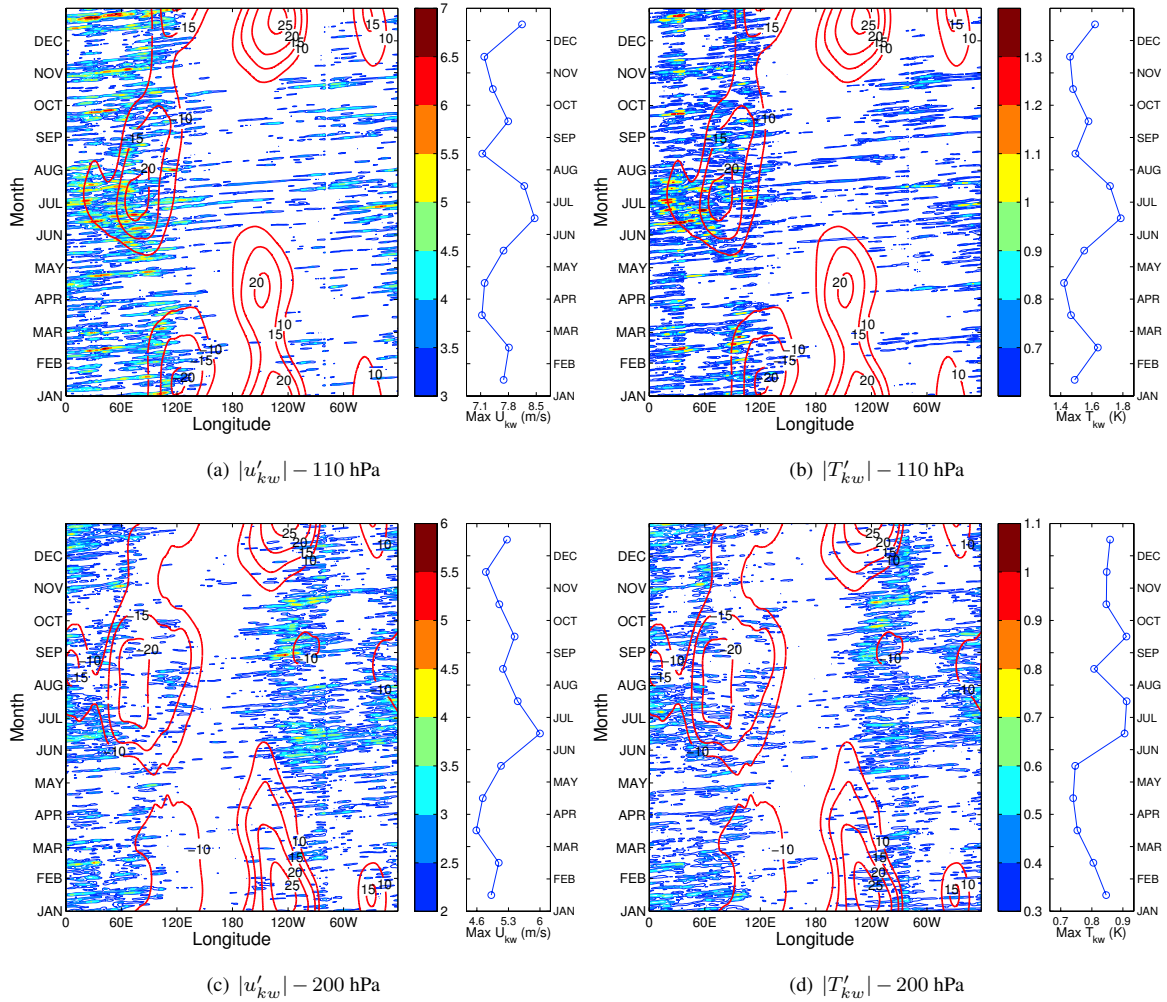


**Figure 13.** Intramonthly Kelvin wave zonal wind and temperature composites as a function of longitude and month in a calendar year at (a-b) model level 40 ( $\sim 110$  hPa) and (c-d) model level 49 ( $\sim 200$  hPa) along  $0.7^\circ\text{N}$ . The waves are accumulated from different years onto a single calendar year to highlight seasonal behaviour. Only the most energetic signals are shown: (a and c) zonal wind,  $|u'_{kw}|$ , each  $0.5 \text{ ms}^{-1}$ , and (b and d) temperature  $|T'_{kw}|$ , each  $0.1 \text{ K}$ . For comparison, the background zonal wind field is presented by red contours, each  $5 \text{ ms}^{-1}$ . On the right side of each panel, blue lines with circles denote maximal amplitude of the KW zonal wind occurring anywhere along the equator averaged over the 6-year period for each calendar month. This highlights seasonality in the maximum amplification of propagating KWs.

# Multivariate analysis of Kelvin wave seasonal variability in ECMWF L91 analyses

Marten Blaauw <sup>1</sup> and Nedjeljka Žagar <sup>1</sup>

<sup>1</sup>University of Ljubljana, Faculty of mathematics and physics, Ljubljana, Slovenia

Correspondence to: Marten Blaauw (marten.blaauw@fmf.uni-lj.si)

1 **Abstract.** ~~The paper presents the seasonal variability of~~

2 ~~The paper performs multivariate analysis of the linear~~ Kelvin waves (KWs) ~~represented by the operational 91-level ECMWF~~  
3 ~~analyses in 2007-2013 ECMWF analyses on 91 model levels. The waves are filtered using the normal-mode function decomposition~~  
4 ~~which simultaneously analyses wind and mass field based on their relationships from linear wave theory. Both spectral as well~~  
5 ~~as spatiotemporal features of the KWs are examined in terms of their seasonal variability in comparison with background wind~~  
6 ~~and stability. Furthermore, a differentiation is made using spectral bandpass filtering between the slow horizontal barotropic~~  
7 ~~KW response and the fast vertical projection response observed as vertically-propagating KWs~~ 2007-2013 period, with focus  
8 ~~on seasonal variability. The applied method simultaneously filters Kelvin wave wind and temperature perturbations in the~~  
9 ~~continuously stratified atmosphere on the sphere. The spatial filtering of the three-dimensional Kelvin wave structure in the~~  
10 ~~upper troposphere and lower stratosphere is based on the Hough harmonics using several tens of linearized shallow-water~~  
11 ~~equation systems on the sphere with equivalent depths ranging from 10 km to a few meters.~~

12 Results ~~show~~ provide the global Kelvin wave energy spectrum. It shows a clear seasonal cycle ~~in KW activity which is~~  
13 ~~predominantly at the largest zonal scales (wavenumber 1-2) with the Kelvin wave activity predominantly in zonal wavenumbers~~  
14 ~~1 – 2~~ where up to 50% more energy is observed during the solstice seasons in comparison with ~~boreal~~ spring and autumn. ~~The~~  
15 ~~spatiotemporal structure of the KW reveals the slow response as a robust "Gill-type" structure~~

16 ~~Seasonal variability of Kelvin waves in the upper troposphere and lower stratosphere is examined in relation to the background~~  
17 ~~wind and stability. A spectral bandpass filtering is used to decompose variability into three period ranges: seasonal, intraseasonal~~  
18 ~~and intramonthly variability component. Results reveal a slow seasonal KW component with a robust dipole structure in the~~  
19 ~~upper troposphere~~ with its position determined by the location of the dominant convective outflow ~~winds~~ throughout the  
20 seasons. Its ~~maximum~~ maximal strength occurs during ~~northern boreal~~ summer when easterlies in the Eastern ~~Hemisphere~~  
21 ~~hemisphere~~ are strongest. ~~The fast response in the form of free traveling KWs occur~~ Other two components represent vertically  
22 ~~propagating Kelvin waves and are observed~~ throughout the year with seasonal variability mostly found in the wave amplitudes  
23 being dependent on ~~the seasonality of the~~ background easterly winds ~~and static stability~~.

## 24 1 Introduction

25 Atmospheric equatorial Kelvin waves (hereafter KWs), first discovered in the stratosphere (Wallace and Kousky, 1968), are  
26 nowadays observed and studied over a broad range of spatial and temporal scales. A broad wavenumber-frequency spectrum  
27 can be traced to the spatiotemporal nature of tropical convection which generates KWs along with a spectrum of other equa-  
28 torial waves. Atmospheric wave response to the stochastic nature of convection was studied by Garcia and Salby (1987) and  
29 Salby and Garcia (1987) who made a distinction between (i) projection or vertical response to short-term heating fluctuations  
30 (e.g. daily convection) and (ii) barotropic or horizontal response to seasonal convective heating. For KWs, the vertical response  
31 gives rise to a broad frequency spectrum of vertically propagating KWs that radiate outward into the stratosphere where they  
32 drive zonal-mean quasi-periodic flows such as the quasi-biennial oscillation (QBO, Holton and Lindzen, 1972). The horizontal  
33 response to seasonal transitions in convective heating gives rise to planetary-scale disturbances with a half-sinusoidal vertical  
34 structure confined to the troposphere. A part of this response remains stationary over the convective hotspot; its shape resem-  
35 bling a classic "Gill-type" KW solution (Gill, 1980). The other part of the response intensifies and advances over the Pacific,  
36 representing a transient component of the Walker circulation (Salby and Garcia, 1987).

37 Both components of the KW response received increased attention in the scientific community over the last decades in terms  
38 of the role they play in the (intra)seasonal variability of the Tropical Tropopause Layer (hereafter TTL), defined as a transition  
39 layer between the typical level of convective outflow at  $\sim 12$  km where the Brunt-Väisälä frequency is at its minimum, and the  
40 cold point tropopause at  $\sim 16$ - $17$  km (Highwood and Hoskins, 1998; Fueglistaler et al., 2009)(Highwood and Hoskins, 1998; Fueglistaler e  
41 Within the TTL, temperature variations play an important role in controlling the stratosphere-troposphere exchange of vari-  
42 ous species such as ozone and water vapour thereby aiding in the dehydration process of air entering the stratosphere. The  
43 two parts of the KW response ~~alternate~~ modulate the TTL differently on different time scales (Highwood and Hoskins, 1998;  
44 Randel and Wu, 2005; Ryu et al., 2008; Flannaghan and Fueglistaler, 2013); their relative contribution to TTL dynamics varies  
45 with season and is not yet fully understood. The present study contributes to this topic by applying a novel multivariate analysis  
46 of Kelvin wave seasonal variability in model-level analysis data.

47 Seasonal variations of Kelvin wave dynamics in the TTL have been previously studied using temperature data derived  
48 from satellites such as SABER (Sounding of the Atmosphere using Broadband Emission Radiometry, Garcia et al., 2005;  
49 Ern et al., 2008; Ern and Preusse, 2009), HIRDLS (High Resolution Dynamics Limb Sounder, Alexander and Ortland, 2010),  
50 and GPS-RO (Global Positioning System Radio Occultation, Tsai et al., 2004; Randel and Wu, 2005; Ratnam et al., 2006).  
51 For example, Alexander and Ortland (2010) reported a clear seasonal cycle around 16-17 km ( $\sim 100$  hPa) in KW temperature  
52 observed by HIRDLS, coinciding closely with variations in background stability. A widely used method for the KW filtering  
53 from gridded data is the space-time spectral analysis introduced by Hayashi (1982). ~~It~~ Space-time spectral filtering assumes  
54 that the linear adiabatic theory for equatorial waves on a resting atmosphere is applicable (Gill, 1982). Filtering operates on  
55 single variable data and it has been widely used to diagnose equatorial waves in the outgoing longwave radiation (OLR, e.g.  
56 Wheeler and Kiladis, 1999) and climate model outputs (e.g. Lin and Coauthors, 2006). Based on 40-year ECMWF reanalysis  
57 (ERA-40) data, Suzuki and Shiotani (2008) found that the temperature component of Kelvin waves tends to peak at 70 hPa

58 while the zonal wind peaks at lower altitudes, i.e. at 100 hPa (and 150 hPa) in Eastern (Western) hemisphere in Eastern and  
59 Western hemisphere, respectively.

60 The zonal wind and geopotential height of the KW are closely related. For a single zonal wavenumber  $k$ , the geopotential,  
61  $\Phi_{kw}$ , and the zonal wind  $U_{kw}$  of a zonally propagating KW are related according to the following equation: On the equatorial  
62  $\beta$ -plane, shallow-water linear wave theory describes the Kelvin wave geopotential height ( $h_{kw}$ ) and zonal wind ( $u_{kw}$ ) perturbations  
63 propagating zonally with phase speed  $c$  as (Matsumo, 1966):

$$64 \quad \Phi_{kw} = g h_{kw}(x, y) = \frac{\nu}{k} \frac{c}{g} U_{kw}, \quad \text{where} \quad U_{kw}(x, y) = U_0 \exp\left(-\frac{\beta k y^2}{2\nu} - \frac{\beta y^2}{2c}\right) \cos k(x - ct). \quad (1)$$

65 Here,  $U_0$  is the KW amplitude in zonal wind on  $u_0$  is the zonal wind amplitude at the equator,  $\beta = 2\Omega/a$  ( $\Omega$  being the  
66 rotation rate and  $a$  the radius of Earth),  $\nu$  is the wave frequency,  $g$  is gravity and  $y$  is the distance from the equator.  
67 These expressions are obtained as a special solution of the linearized shallow-water equations on the equatorial  $\beta$ -plane  
68 (e.g. Holton, 2004, Chapter 11). The  $\beta = df/dy$ ,  $f$  being the Coriolis parameter. The dispersion relationship between the  
69 wave frequency  $\nu$  and the zonal wavenumber  $k$  is  $\nu = kc$ . The gravity wave speed in a layer of homogeneous fluid with mean  
70 depth  $D$  is given by  $c = \sqrt{gD}$  (Gill, 1982).

71 The KW  $e$ -folding decay width,  $a_e$ , known as the equatorial radius of deformation, is given by  $a_e = (c/2\beta)^{1/2}$ , where  
72 the KW phase speed  $c$  is determined from the dispersion relation  $\nu = kc$ . By prescribing the value of KW phase speed  $c$  (i.e.  
73 the equivalent depth of the shallow-water equation system), analytical solutions from linear wave theory  $D$ , the horizontal  
74 structure of KW is defined by (1) for any  $k$  and can be used to simultaneously analyze wind and height data of the KW wave  
75 geopotential height perturbations due to KW waves on a single horizontal level. Such multivariate analysis was carried out  
76 by Tindall et al. (2006) who analyzed several levels the ECMWF 15-year reanalysis dataset (for the lower stratosphere for  
77 the ERA-15) in the lower stratosphere. They reported a maximum of Kelvin wave activity at 100 hPa around the solstices  
78 when tropical cloud activity maximizes. For the ERA-15 data in 1981-93 period, their Kelvin wave analysis explained. Their  
79 results suggested that KWs contributes approximately 1 K<sup>2</sup> of the temperature variance on the equator with peak activity  
80 occurring during solstice seasons at 100 hPa, during December-February at 70 hPa and at 50 hPa it occurs during the  
81 easterly to westerly quasi-biennial oscillation (QBO) phase transition. Yang et al. (2003) used  $a_e$  as the fitting parameter for  
82 the projection of the ERA-15 data on the meridional structure of the KW and other equatorial waves. They found that the best  
83 fit trapping scale within 20°N-20°S is around 6°. The multivariate projection of data on the horizontal structures of equatorial  
84 waves including KWs on the equatorial  $\beta$ -plane was performed also for the short-range forecast errors of the ECWMF model  
85 (Žagar et al., 2005, 2007). For example, Žagar et al. (2007) found that forecast errors within 20°N-20°S belt project on KWs  
86 significantly more in the easterly QBO phase than in the westerly phase.

87 The present paper extends the use of linear wave theory from In this paper we extend the linear Kelvin wave analysis based  
88 on the shallow-water equation theory on the equatorial  $\beta$ -plane to the sphere. Second, we extend the KW filtering on individual  
89 horizontal levels or vertical planes to the three-dimensional (3D) spherical coordinates in order to analyze KW analysis  
90 simultaneously in wind and temperature fields in recent ECMWF operational analyses. We focus on. This study thus explores  
91 seasonal variability of KWs in the TTL layer in the ECMWF operational analyses during a period when the model employed

92 91-vertical level (L91) between the surface and 1 Pa. The L91 model was in operations between 2006 and early summer 2013  
93 when it was replaced by 137 levels. This study thus explores most of a multivariate fashion using most of the information  
94 on the vertical structure of KWs available in the L91 analysis data. We present a methodology for the simultaneous analysis  
95 of wind and temperature perturbations associated with KWs with respect to the background state and apply it to quantify  
96 scale-dependent seasonal KW variability in several frequency bands. wave structure available in recent operational ECMWF  
97 analyses.

98 The paper consists of five sections. Methodology On the sphere, the Kelvin mode is the slowest eastward-propagating  
99 eigensolution of the shallow-water equations (or Laplace tidal equations) linearized around a state of rest (e.g. Kasahara, 1976).  
100 In the continuously stratified atmosphere, the depth  $D$  becomes the "equivalent depth" of a given baroclinic mode and we need  
101 to solve Laplace tidal equations for a range of  $D$  from large (corresponding to the barotropic structure) to rather small (for  
102 high baroclinic modes) in order to consider the spectrum of Kelvin waves (e.g. Boyd, 2018). In contrast to the Kelvin wave  
103 trapping on the equatorial  $\beta$ -plane, which is controlled by  $a_e$  i.e. by the equivalent depth, the degree of the KW diagnosis  
104 and the data are presented in section 2 equatorial confinement on the sphere is in addition controlled by the zonal wavenumber  
105 (Boyd and Zhou, 2008). As shown by Boyd and Zhou (2008), even barotropic KW with  $D$  around 10 km are on the sphere  
106 confined within the tropical belt.

107 In section 2 we present a methodology which diagnosis 3D Kelvin waves in spherical datasets. Section 3 presents the  
108 KW energetics in wavenumber space focusing on the seasonal cycle. Section 4 presents a 3D view on KWs in L91 dataset,  
109 seasonal KW variability in several frequency bands both for the horizontal as well as for the vertical projection KW response.  
110 Conclusions and outlook are given in section 5.

## 111 2 Data and methodology

112 The Kelvin waves are filtered using the Normal-Mode-Function-normal-mode function (NMF) decomposition derived by  
113 Kasahara and Puri (1981) and briefly summarized below, formulated as the *MODES* software package by Žagar et al. (2015).  
114 Here the methodology is briefly summarized followed by the method for the computation of the KW temperature perturbations  
115 and by examples of the 3D KW structure in global data.

116 Input ECMWF operational analyses cover 6 covers approximately 6.5 years from January 2007 till June 2013, approximately  
117 6.5 years, untill June 2013. The dataset starts after two important updates in the ECMWF assimilation cycle: a resolution update  
118 on 1 February 2006 and the introduction of GPS-RO temperature profiles in the assimilation on 12 December 2006. The data  
119 ends at the next update in vertical resolution from L91 to L137 on 25 June 2013. The data horizontal resolution is  $256 \times 128$   
120 points in the zonal and meridional directions (regular Gaussian grid N64), respectively, on 91 irregularly spaced hybrid model  
121 levels up to around 0.01 hPa (around 80 km). The temporal resolution is 6 hours, i.e. 4 times per day, at 00, 06, 12 and 18 UTC.  
122 A case study of the large-scale KW in July 2007 (Žagar et al., 2009) showed how in this dataset by Žagar et al. (2009) showed  
123 that the NMF method provides information on the horizontal and vertical 3D wave structure and its vertical propagation in the

124 stratosphere. [Another case study from the same month demonstrated how the vertical KW structure improves as the number of](#)  
 125 [vertical levels increased \(Žagar et al., 2012\).](#)

## 126 2.1 Filtering of Kelvin waves by 3D normal-mode function expansion

127 The basic assumption behind the NMF expansion is that a global state of the atmosphere described by its mass and wind vari-  
 128 ables at any time can be considered as a superposition of the linear wave solutions upon a predefined background state. ~~These~~  
 129 ~~linear solutions describe two types of wave motions: Rossby waves and inertio-gravity waves which obey their corresponding~~  
 130 ~~dispersion relationships. The associated eigensolutions in terms of the Hough harmonics define both mass and wind fields of~~  
 131 ~~the waves. The linear wave theory approach has been successfully employed in many studies, especially for the large-scale~~  
 132 ~~tropical circulation features (e.g. Gill, 1980; Salby and Garcia, 1987; Garcia and Salby, 1987).~~

133 The NMF decomposition derived by Kasahara and Puri (1981) uses the  $\sigma$  ~~coordinates and a vertical coordinate and linearization~~  
 134 ~~around the state of rest and~~ realistic vertical temperature and stability stratification. 3D wave solutions of ~~primitive equations~~  
 135 ~~linearized around the state of rest~~ [linearized primitive equations](#) are represented as a truncated time ~~serie series~~  
 136 harmonic oscillations and the vertical structure functions. The [assumption of separability leads to separate equations for the](#)  
 137 [vertical structure and horizontal oscillations. The latter are known as shallow-water equations on the sphere or Laplace tidal](#)  
 138 [equations without forcing. The two systems are coupled by a separation parameter  \$D\$  which is called the equivalent height](#)  
 139 [\(Boyd, 2018\). Eigenmodes of the global shallow-water equations are known as Hough harmonics. They describe two types of](#)  
 140 [wave motions: Rossby waves and inertio-gravity waves which obey their corresponding dispersion relationships on the sphere.](#)

141  
 142 [The expansion of a global input data vector  \$\mathbf{X}\(\lambda, \varphi, \sigma\) = \(u, v, h\)^T\$  can be represented by a discrete finite series as:](#)

$$143 \begin{pmatrix} u(\lambda, \varphi, \sigma) \\ v(\lambda, \varphi, \sigma) \\ h(\lambda, \varphi, \sigma) \end{pmatrix} = \sum_{m=1}^M \mathbf{S}_m \left[ \sum_{n=1}^R \sum_{k=-K}^K \chi_n^k(m) \mathbf{H}_n^k(\lambda, \varphi; m) \right] G_m(\sigma) \quad (2)$$

144 The [input data vector contains wind components  \$u, v\$  and the transformed geopotential height  \$h\$  defined as  \$h = g^{-1}P\$  where](#)  
 145  [\$g\$  is the gravity and  \$P\$  is defined as:  \$P = \Phi + RT\_0 \ln\(p\_s\)\$ ; that it, it is the sum of geopotential  \$\Phi\$  and a surface pressure,  \$p\_s\$ , term.](#)  
 146 [Other two variables represent the specific gas constant for dry air \( \$R\$ \) and the globally-averaged vertical temperature profile](#)  
 147 [\( \$T\_0\(\sigma\)\$ \). The zonal and vertical truncations \( \$K\$  and  \$M\$ , respectively\) define ~~maximum maximal~~ numbers of zonal waves at a  
 148 single latitude \(wavenumber  \$k\$ \) and a maximal number of vertical modes ~~denoted  \$m\$  respectively.~~ \(denoted  \$m\$ \) respectively. For  
 149 \[every vertical structure eigenfunctions  \\$G\\_m\\(\sigma\\)\\$ , Hough harmonic functions,  \\$\mathbf{H}\\_n^k\\(\lambda, \varphi\\)\\$  describe non-dimensional oscillations in\]\(#\)  
 150 \[the horizontal plane of the fluid with the mean depth equal the equivalent depth  \\$D\\_m\\$ . The parameter  \\$D\\_m\\$  appears in Eq. \\(2\\) in\]\(#\)  
 151 \[the diagonal matrix  \\$\mathbf{S}\\_m\\$  with elements  \\$\\(gD\\_m\\)^{1/2}\\$ ,  \\$\\(gD\\_m\\)^{1/2}\\$  and  \\$D\\_m\\$  which normalizes the input data vector after the vertical\]\(#\)  
 152 \[projection and thereby removes dimensions. Parameter  \\$R\\$  is the total number of meridional modes which is a sum of the\]\(#\)  
 153 eastward inertio-gravity waves \(EIG\), westward inertio-gravity waves \(WIG\) and Rossby waves. ~~Oscillations in the horizontal~~  
 154 ~~plane are given in terms of Hough harmonic functions,  \$\mathbf{H}\_n^k\(\lambda, \varphi\)\$  for every vertical structure eigenfunctions  \$G\_m\(\sigma\)\$ . The~~](#)



155 horizontal and vertical solutions are connected by the equivalent depth parameter  $D_m$ , which appears in Eq. (2) in the diagonal  
 156 matrix  $\mathbf{S}_m$  with elements  $(gD_m)^{1/2}$ ,  $(gD_m)^{1/2}$  and  $D_m$ . Linearization about the state of rest is not a drawback of the method as  
 157 wave frequencies are used solely for the formulation of the projection basis and not for studying wave propagation properties.  
 158 As shown by Kasahara (1980) (see also its Corrigendum) the meridional structures of the Hough functions for large scales are  
 159 not significantly different if the linearization is performed around the non-zero mean zonal flow. The impact of latitudinal shear  
 160 on the Kelvin waves was shown negligible by Boyd (1978). Further details of the applied NMF representation NMF projection  
 161 procedure are given in Žagar et al. (2015).

162 The input data vector contains wind components  $u, v$  and the geopotential height  $h$  defined as  $h = g^{-1}P$  where  $g$  is the  
 163 gravity and  $P$  is a modified geopotential given by:  $P = \Phi + RT_0 \ln(p_s)$ , i. e. the sum of the geopotential field  $\Phi$  and a  
 164 surface pressure  $p_s$  term. Other two variables represent the specific gas constant for dry air ( $R$ ) and the globally-averaged  
 165 vertical temperature profile ( $T_0$ ). For each zonal wavenumber, the Kelvin mode is the lowest eastward-propagating  
 166 latitudinal Hough function. In (2), the Kelvin wave is represented by the nondimensional complex expansion coefficients  
 167  $\chi_n^k(m)$  represent both geopotential height and wind perturbations due to waves. The Kelvin mode is represented in (2) by  
 168 the first eastward-propagating IG mode. Although our meridional index starts from 1 (to follow otherwise used notation) with  
 169 the meridional index  $n = 1$ . However, to follow often used notation, we shall denote KW in the remainder the Kelvin wave  
 170 in the remainder of this study as the  $n = 0$  EIG mode, i.e. the KWs are given Kelvin wave wind and geopotential height are  
 171 represented by coefficients  $\chi_{kw} = \chi_0^k(m)$ .

172 In our application to the L91 ECMWF dataset, we used data on the N64 Gaussian grid and 91 model levels with model  
 173 top located at 0.01 hPa (around 80 km). Data are analyzed 4 times per day, at 00, 06, 12 and 18 UTC. The pre-processing  
 174 step consists of the interpolation of winds and geopotential from the hybrid ( $\sigma-p$ ) levels to  $\sigma$  levels after geopotential  $\Phi$   
 175 is computed on the hybrid levels. The truncation values are  $K = 55$ ,  $K = 85$  and  $M = 60$ . This means that KW signal  
 176 in 3D circulation at a single time instant consists of 5100 waves, 85 waves in every shallow-water equation system. Higher  
 177 vertical modes were left out as their contribution equivalent depth is smaller than 2 meters and their contribution to the total  
 178 KW signal is negligible in the outputs in the TTL and the stratosphere. The relation between the truncation parameters and the  
 179 normal-mode projection quality is discussed in Žagar et al. (2015) and references therein.

180 Once the forward projection is carried out and coefficients  $\chi_n^k(m)$  are produced, filtering of KWs in physical space can be  
 181 performed through (2) after setting all  $\chi$ , except those representing the KWs, to zero. The result of filtering are fields  $u_{kw}$ ,  
 182  $v_{kw}$  and  $h_{kw}$  which provide the KW zonal wind, meridional wind and geopotential height perturbations. Notice here that in  
 183 contrast to the equatorial  $\beta$ -plane, KWs on the sphere have a very small meridional wind component which is thus left out  
 184 from the discussion (Boyd, 2018).

185 The KW temperature perturbation,  $T_{kw}$  can be derived from the  $h_{kw}$  fields on  $\sigma$  levels using the hydrostatic relation in  $\sigma$   
 186 coordinates:

$$187 \quad T_{kw} = -\frac{g\sigma}{R} \frac{\partial h_{kw}}{\partial \sigma}. \quad (3)$$

188 The orthogonality of the normal-mode basis functions provides KW energy as a function of the zonal wavenumber and  
 189 vertical mode. After the forward projection, the energy spectrum of total (potential and kinetic) energy for each Kelvin wave  
 190 can be computed using the energy product for the  $k$ th and  $m$ th normal modes (Žagar et al., 2015) as:

$$191 \quad I_{\text{kw}}(k, m) = \frac{1}{2} g D_m \chi_{kw} [\chi_{kw}]^* . \quad (4)$$

192 The units are  $\text{J kg}^{-1}$ . The KW global energy spectrum as a function of the zonal wavenumber is obtained by summing energy  
 193 in all vertical modes:

$$194 \quad I_{\text{kw}}(k) = \frac{1}{2} \sum_{m=1}^M g D_m \chi_{kw} [\chi_{kw}]^* . \quad (5)$$

## 195 2.2 Examples of 3D structure of Kelvin waves in L91 analyses

196 Kelvin waves are shown in Fig. 1-2 for a few days in July 2010 to introduce and illustrate their properties as filtered by the  
 197 NMF methodology. ~~The second part of July 2010 was characterized by an abundance in both vertically propagating as well as~~  
 198 ~~quasi-stationary KW structures throughout the atmosphere.~~

199 Figure 1 illustrates the meridional structure of Kelvin waves on 25 July 2010 on 2 levels. KW activity was found largest in  
 200 the zonal wind component at 150 hPa over the Indian Ocean. The geopotential dipole structure is ~~centered-centred~~ over the  
 201 convective hotspot over the Maritime continent. At 100 hPa, we find largest amplitude of KW temperature perturbations up to  
 202 4 K positioned above the zonal wind maxima at 150 hPa. The meridional wind component of the KW is nonzero in spherical  
 203 coordinates, but is at most  $0.22 \text{ ms}^{-1}$  at 100 hPa which is negligible compared to the zonal wind component (maximum  $12.5$   
 204  $\text{ms}^{-1}$ ) making the KW wind field primarily zonal. Note that the presented horizontal structure at a single level is a superposition  
 205 of 60 vertical modes, i.e. 60 shallow water models with equivalent ~~depts-depths~~ from about 10 km to a couple of meters.

206 Figure 2 ~~can be discussed in relation to Eq. . It states that the amplitude of the cold (warm) KW temperature perturbation~~  
 207 ~~is proportional to the negative (positive) vertical gradient in geopotential, as well as in zonal wind since zonal wind and~~  
 208 ~~geopotential components are in phase. Horizontally, the cold anomaly is always located between the westerly and the easterly~~  
 209 ~~phase of the zonal wave component. Vertically, maximum positive temperatures are observed between easterly winds below and~~  
 210 ~~westerly winds above. A rough estimation can be made of the vertical wavelength based on alternating zonal wind minima and~~  
 211 ~~maxima. For example, on 31 July a quasi-stationary vertical wave structure with extension in the stratosphere located around~~  
 212 ~~60°E has easterly winds located at 50 hPa illustrates day-to-day filtered KW fields along the equator on three separate July days~~  
 213 ~~in 2010, namely 25, 28 and 31. Both zonal wind ( $\sim 21.5$  km) and 150 hPa ( $\sim 13.5$  km), which makes a vertical wavelength~~  
 214 ~~of around 8 km. blue-to-red shades) and temperature fields (red contours) are shown. Without any predefined constrains on the~~  
 215 ~~KW propagation, one can observe a rich variety of KW behaviour occurring in time: from the quasi-stationary dipole patterns~~  
 216 ~~centred at 160 hPa to a wave package of free propagating wave structures in the stratosphere transiting from the western into~~  
 217 ~~the eastern hemisphere.~~

218 In the stratosphere, ~~above 80 hPa , strong KW activity was present in the form of free waves propagating the uppermost~~  
 219 ~~easterly wind component in blue shades around 30 – 50 hPa moves in~~ eastward and downward ~~, therefore with direction,~~



220 demonstrating the upward transport of KW energy (Andrews et al., 1987). KW amplitudes were largest over Eastern hemi-  
221 sphere with temperatures up to 4 K and zonal winds up to  $12 \text{ ms}^{-1}$ . The large amount of KW activity occurred during the  
222 easterly phase of the QBO with strong easterly winds present between 30 and 80 hPa (not shown), providing favourable con-  
223 ditions for ~~the waves to propagate upward~~strong KW activity.

224 Between 100 and 200 hPa during the second half of July, there was low-frequency KW activity present in the form of a  
225 stationary and robust "wave-1" pattern with strong KW easterly winds up to  $24 \text{ ms}^{-1}$  in Eastern Hemisphere and KW westerly  
226 winds up to  $10 \text{ ms}^{-1}$  in the Western Hemisphere. The high vertical resolution within the TTL resolves shallow KW structures  
227 and a typical slanted structure towards the east in KW easterlies as well. The appearance and strength of horizontal KW  
228 response coincides with the presence of strong easterly winds in the TTL in the Eastern Hemisphere during this period (not  
229 shown). Figure 2 also shows that below 300 hPa the KW activity decreases and we shall not discuss levels under 300 hPa in  
230 the paper.

231 The zonal wind and temperature components are coupled through Eq. (3) which states that the amplitude of the negative  
232 KW temperature perturbation is proportional to the negative vertical gradient in geopotential (and vice versa), as well as in the  
233 zonal wind since the zonal wind and geopotential are in phase. Horizontally, the cold anomaly is always located between the  
234 westerly and the easterly phase of the zonal wind component. Vertically, maximal positive temperatures are observed between  
235 easterly winds below and westerly winds above. An estimate of the vertical wavelength can be made based on alternating zonal  
236 wind minima and maxima. For example, on 25th July a well-developed KW package extending into the stratosphere moved  
237 from the Western into the Eastern hemisphere. A quasi-stationary component of the wave package is observed around  $60^\circ\text{E}$   
238 with easterly winds located at 50 hPa ( $\sim 21.5 \text{ km}$ ) and 150 hPa ( $\sim 13.5 \text{ km}$ ), implying a vertical wavelength of around 8 km.

239 More examples based on daily basis filtered from the 10-day deterministic forecast of the ECMWF can be found on the  
240 MODES website<sup>1</sup>.

### 241 2.3 Other data and impact of the background state

242 In addition to the outputs from modal decomposition, full zonal wind and temperature fields from ECMWF analyses are used  
243 to compute the background fields based on the same N64 grid and over the same period (Jan 2007 - Jun 2013). Zonal wind  $U$   
244 and static stability  $N$  are latitudinally averaged in the belt  $5^\circ\text{S}$ - $5^\circ\text{N}$  on all model levels to produce their zonal structure.

245 Static stability profiles are estimated through

$$246 \quad N^2 = \frac{g^2}{\Theta} \frac{\partial \Theta}{\partial \phi} \quad (6)$$

247 in units of  $\text{s}^{-2}$  and are defined on hybrid model levels on which the geopotential field  $\phi$  and the potential temperature field  $\Theta$   
248 are derived a priori from the input data. Both fields are shown in Fig. 3.

249 The zonal wind field has the largest values on average in the TTL around 150 hPa with westerly winds peaking in the Western  
250 Hemisphere over the Pacific Ocean and easterly winds peaking in the Eastern ~~Hemisphere~~ hemisphere over the Indian Ocean  
251 and Indonesia. It represents a typical time-averaged outflow pattern in response to tropical convection (e.g. Fueglistaler et al.,

---

<sup>1</sup><http://meteo.fmf.uni-lj.si/MODES/>

252 2009). Throughout the seasons there is a longitudinal shift of this pattern following the convective source which is most clearly  
253 observed at 150 hPa. Such seasonal shift is visible up to 100 hPa in Fig. 3(b) where winds are weaker compared to 150 hPa.  
254 In northern winter, zonal winds are strongest over Indonesia and [the](#) Eastern Pacific with the zonal wind maxima position and  
255 strength similar compared to the longer ERA-40 dataset used by Suzuki and Shiotani (2008). During [northern-boreal](#) summer  
256 easterly winds mainly prevail over the Indian Ocean, which is linked to the Indian Monsoon season.

257 At 100 hPa, the static stability illustrates the strongest seasonal cycle with values ranging from near-tropospheric values  
258 of  $3 \times 10^{-4} \text{ ms}^{-2}$  during northern winter towards stratospheric values of  $5 - 6 \times 10^{-4} \text{ ms}^{-2}$  during [northern-boreal](#) summer.  
259 Note also the resolved local maxima in static stability at 80 hPa above the warm pools, known as the Tropical Inversion  
260 Layer (TIL) and which is possibly wave-driven (Grise et al., 2010; Kedzierski et al., 2016). Figure 3(b) suggests that the TIL  
261 descends down to 100 hPa during [the-boreal](#) summer months peaking over Western Pacific, in agreement with the cycle found  
262 in GPS-RO observations by Grise et al. (2010).

263 Kelvin waves are subject to wave modulation in changing background environments. Along its trajectory, the potential  
264 energy of the KW changes with varying background winds and stability which can be largely described by linear wave theory  
265 as long as waves are not near their critical level involving breaking and dissipation (Andrews et al., 1987). For simplification,  
266 KW modulation can be examined for the case of pure zonal as well as pure vertical wave propagation based on the wave  
267 modulation analysis performed by Ryu et al. (2008). A few key points on their local wave action conservation principle are  
268 [summarized-summarised](#) in the following.

269 In the tropical atmosphere, zonal modulation is the dominant process for KWs propagating in the stratosphere and in all  
270 non-easterly winds in the TTL. Vertical modulation becomes important in the presence of easterly winds within the TTL.  
271 Zonal modulation is found to affect both  $u_{kw}$  and  $T_{kw}$  components and their amplitudes are proportional to the Doppler-  
272 shifted phase speed by  $(c - U)^{1/2}$  in case of pure zonal propagation direction. This means that Kelvin waves diminish in  
273 amplitude over regions with westerly winds and become more prone to dissipative processes, while amplify over regions with  
274 easterly winds<sup>2</sup>. In case of pure vertical modulation, the change in wave potential energy mainly [resonates-fluctuates](#) with the  
275 temperature component of the Kelvin wave. Along the rays' vertical path, the waves amplitude is proportional to the Brunt-  
276 Väisälä frequency as  $\propto N^{3/2}$ , and to the Doppler-shifted phase speed as  $\propto (c - U)^{-1/2}$ , such that  $N$  is expected to play a  
277 primary role above 120 hPa where its value starts increasing rapidly (see Fig. 3).

278 Alexander and Ortland (2010) showed through wave modulation principles that temporal variations in zonal-mean  $N$  indeed  
279 are correlated with observed KW amplitudes at 16 km (approx. 100 hPa). A more extensive wave modulation analysis was  
280 described by Flannaghan and Fueglistaler (2013) using the full ray tracing equations to demonstrate that zonal winds in the TTL  
281 not only modulate Kelvin waves locally, but also create a lasting modulating effect on wave activity through ray convergence  
282 in the stratosphere. In particular, the seasonal cycle of the upper tropospheric easterlies (on average located over the western  
283 Pacific), that acts as an escape window for Kelvin waves throughout the year and largely explains the longitudinal structure of  
284 Kelvin wave zonal wind and temperature climatology.

---

<sup>2</sup>Keeping in mind that vertical wave propagation and consequently modulation becomes increasingly important as well wherever easterly winds are strong.

285 We shall present the seasonal variability of tropical convection by using the Outgoing Longwave Radiation (OLR) dataset  
286 with daily outputs from the NOAA Interpolated OLR product (Liebmann and Smith, 1996). The OLR product, often used as  
287 a proxy for convection, is extracted on a  $2.5^\circ \times 2.5^\circ$  grid and interpolated on a N64 grid. ~~Latitudal~~Latitudinal averages are  
288 derived over larger domain, namely over  $15^\circ\text{S}$ - $15^\circ\text{N}$  since organized convection tend to happen more remote from the equator,  
289 especially during the summer monsoon season over the Asian continent.

### 290 3 Kelvin wave energetics

291 We start with ~~an overview of a discussion of the~~ KW energy distribution among ~~the~~ zonal wavenumbers as given by (5),  
292 followed by ~~the seasonal cycle of KW energy as a function of zonal wavenumber.~~ seasonal differences.

#### 293 3.1 Energy distribution of Kelvin wave

294 The seasonal cycle in the energy-zonal wavenumber spectra is shown in Fig. 4 after summing up over all vertical modes. On  
295 average, energy decreases as the zonal wavenumber increases as typical for atmospheric energy spectra. As we deal with the  
296 large scales, we show only the first six zonal wavenumbers with energy values shown separately for the annual mean and the  
297 four seasons separately.

298 Figure 4 shows that largest seasonal variations in KW energy are found at the largest zonal scales. For all zonal wavenumbers,  
299 above annual-mean energy values are observed during ~~winter and summer seasons while autumn and spring~~ DJF and JJA  
300 seasons while SON and MAM are below annual-mean energy. In the zonal wavenumber 1, total KW energy varies between  
301  $200 \text{ Jkg}^{-1}$  in MAM season and somewhat over  $300 \text{ Jkg}^{-1}$  in JJA. In wavenumber 2, values do not exceed  $100 \text{ Jkg}^{-1}$  and  
302 JJA still contains the largest energy. At higher wavenumbers, DJF season becomes the most energetic. In  $k > 4$ , total KW  
303 energy is under  $20 \text{ Jkg}^{-1}$  and continue to reduce with  $k$ . The slope of the KW energy spectrum is between  $-5/3$  and  $-1$  at  
304 planetary scales (not shown), similar to the spectra presented in Žagar et al. (2009) for July 2007 data. The ~~summer~~-JJA spectra  
305 has on average the steepest slope compared to other seasons, in particular the ~~winter~~-DJF spectra. The energy distribution on  
306 planetary scales is mainly associated with large-scale tropical circulation established in response to ongoing tropical convection.  
307 Therefore, the zonal distribution of tropical convection may likely play a crucial role in explaining ~~winter and summer~~-DJF  
308 and JJA season differences of KW energy, which will be explored in next section.

#### 309 3.2 Seasonal cycle of KW energy

310 Figure 5 illustrates more details on the seasonal cycle by showing KW energy time series at the largest scales represented by  
311 zonal wavenumbers  $k = 1$ ,  $k = 2$  and remaining scales  $k > 2$ . During most ~~summers~~-JJA seasons and occasionally in ~~winter~~  
312 DJF (e.g. 2008) the total amount of KW energy in  $k = 1$  can reach up to  $600 \text{ Jkg}^{-1}$ , or twice the ~~summer~~-JJA average.  
313 The minimum in  $k = 1$  KW energy mainly occurs during October ~~month~~ followed by April with values dropping towards  
314  $100 \text{ Jkg}^{-1}$ , or half the ~~autumn~~-SON average. The temporal pattern in  $k = 2$  is similar to the  $k = 1$  pattern, but with a less

315 pronounced semiannual cycle with maximum values up to  $200 \text{ Jkg}^{-1}$  and minimum values towards  $30 \text{ Jkg}^{-1}$ . On zonal scales  
316  $k > 2$ , KWs still show a semiannual cycle with highest vertically-integrated values of energy ~~over winter seasons~~ in DJF.

317 In particular, for zonal wavenumber  $k = 1$  one can distinguish ~~inter-monthly~~ intermonthly in addition to semiannual vari-  
318 ability. ~~Inter-monthly~~ Intermonthly variability is most clearly observed during ~~northern summer~~ JJA, for example in July 2011  
319 where one can distinguish six separate peaks of over  $400 \text{ Jkg}^{-1}$  energy over a period of approximately 90 days resembling  
320 an average wave period of about 18 days. These are typical periods for free propagating Kelvin waves as observed in the  
321 TTL and lower stratosphere (e.g. Randel and Wu, 2005). Note here again that our KW energy is vertically integrated over the  
322 whole model depth. This means that the observed intermonthly variability of KWs appears dominated by the cyclic process of  
323 free propagating KWs entering the TTL, amplifying due to changing environmental conditions, followed by wave breaking or  
324 dissipation.

325 The dominant scales of temporal variability in KWs are illustrated by a frequency spectrum of  $k = 1$  in Fig. 6. The spectrum  
326 is produced by ~~a the~~ Fourier transform of energy data time series of 6.5 years ~~to frequency space~~. The resulting power  
327 spectrum has been smoothed by taking the Gaussian-shaped moving averages over the raw spectrum by using ~~a the~~ Daniell  
328 kernel three times (Shumway and Stoffer, 2010). The spectrum ~~shows a clear~~ contains a peak at 1-day period ~~representing~~  
329 ~~tidal variability in KWs~~ associated with the diurnal tide partially projecting on the Kelvin waves. After that, a gradual increase  
330 of energy is seen towards the 16-day period with multiple individual periods standing out. For periods longer than 20 days,  
331 individual peaks are found close to 25, 43 and 59 days. After that, most KW energy is contained by far in the semiannual cycle.  
332 The frequency spectrum provides ~~an a~~ useful starting point for the discussion in the next section when the spatiotemporal  
333 patterns of KWs shall be examined in several spectral domains.

334 Returning to Fig. 5, a low-pass filter with 90 day cut-off has been applied on KW energy in order to keep only the two  
335 main spectral peaks in Fig. 6. The result is visible as the thicker black line in Fig.5 for all three zonal wavenumber groups. A  
336 semiannual cycle for all zonal wavenumbers is evident with most energy observed around January and July, while least energy  
337 is observed approximately one month after the equinoxes. During the years 2007, 2010, 2011, and 2012, more  $k = 1$  KW  
338 energy is observed during ~~summer~~ JJA compared to the follow-up ~~winter~~. ~~The winter~~ DJF season. ~~The DJF~~ of 2009-2010 was  
339 for example above average with energy values for  $k = 1$  above  $350 \text{ Jkg}^{-1}$ .

340 The year to year differences can be explained by many coupled factors: ~~-,~~ In general, one expects ~~the~~ vertically-integrated  
341 KW activity to increase when background wind conditions become favorable, i.e. in the presence of easterly winds. This  
342 occurs in the TTL in relation to strong convective outflow (Garcia and Salby, 1987; Suzuki and Shiotani, 2008; Ryu et al.,  
343 2008; Flannaghan and Fueglistaler, 2013) during ~~winter and summer~~ DJF and JJA seasons mainly. Moreover, ~~one can expect~~  
344 ~~enhanced KW activity whenever the easterly QBO cycle is present in the~~ KW activity is enhanced whenever easterly QBO  
345 winds are present down into the lower stratosphere (Baldwin and Coauthors, 2001; Alexander and Ortland, 2010) or ~~when the~~  
346 ~~ENSO index is positive during El Niño~~ (Yang and Hoskins, 2013). The latter factor ~~might explain partly the~~ may partly explain  
347 a large difference in the ~~abundant amount of~~ KW energy during the El Niño ~~winter~~ DJF of 2009-2010 and the below-average  
348 ~~amount of KW energy~~ energy level a year after, during the strong La Niña ~~winter~~ DJF period of 2010-2011. However, during  
349 the La Niña ~~winter~~ DJF of 2007-2008, the amount of KW energy is ~~observed to be~~ above normal. That ~~winter~~ season was

350 however characterized by ~~favorable~~ above-normal MJO activity which often occurs during favourable easterly QBO conditions  
351 in the stratosphere ~~while during the winter of~~ (Son et al., 2017). During 2010-2011 DJF season stratospheric winds were largely  
352 westerly ~~of nature~~ thereby prohibiting KW activity. The role of these low-frequency atmospheric phenomena on KW seasonal  
353 variability is a topic of further research.

354 Finally, Fig. 5 also shows that KW activity in July 2007, previously examined by Žagar et al. (2009), was ~~an exceptionally~~  
355 ~~energetic month~~ exceptionally strong. A large part of that energy, ~~approximately 400 Jkg<sup>-1</sup> (52.7% of total KW energy), was~~  
356 ~~projected on~~ (somewhat more than half belonged to zonal wavenumber 1. In spatiotemporal terms, it ~~represented~~ is associated  
357 with the presence of a strong dipole structure in the TTL (as in Fig.2), which is colocated with favourable easterly wind  
358 conditions in the TTL as well as in the stratosphere (not shown). In fact, at 50 hPa the QBO was just at the beginning of its was  
359 easterly phase in July 2007.

## 360 4 A spatiotemporal view on Kelvin wave seasonal variability

### 361 4.1 Kelvin wave decomposition among wave periods

362 In this section, the spatiotemporal view of KWs shall be presented over three dominant ranges of wave periods in Fig. 6,  
363 namely: (i) the (semi)annual cycle using a low-pass filter with cut-off period at 90 days, (ii) the intraseasonal period using  
364 a bandpass filter over periods between 20-90 days, and finally (iii) the intramonthly period with bandpass filtered periods  
365 between 3-20 days. The ~~choice of ranges chosen periods~~, especially the intramonthly periods ~~is related to previous studies using~~  
366 ~~observations. For all three cases, mean 6-year,~~ are similar to those used in previous studies. In each case, mean 6-year fields as  
367 well as seasonal means shall be presented.

368 Note that our temporal filtering operates on time series of KW signals at every grid point. This is different from the  
369 commonly applied space-time filtering following Hayashi (1982) that applies KW dispersion relations. Our filtered KWs can  
370 appear stationary or even westward shifted due to westward-moving sources of the KW amplification (e.g. easterly winds, high  
371 static stability in the TTL).

372 Both KW components  $u_{kw}$  and  $T_{kw}$  are Fourier-transformed to frequency space where the spectral expansion coefficients  
373  $\chi_{kw}$  in domains outside the desired frequency ranges are put to zero. Case (i) results in KW components  $u_{kw,l}$  and  $T_{kw,l}$  where  
374  $l$  indicates the low-frequency component. Case (ii) results in  $u_{kw,m}$  and  $T_{kw,m}$  where  $m$  indicates the intramonthly period.  
375 Case (iii) results in fields  $u_{kw,h}$  and  $T_{kw,h}$  where  $h$  stands for the high-frequency component. Previous studies have defined  
376 free propagating Kelvin waves over similar ranges (3-20 days, Alexander and Ortland (2010); 4-23 days, Suzuki and Shiotani  
377 (2008)) and similarly for intraseasonal periods (23-92 days, Suzuki and Shiotani (2008)). Next, seasonal averages will be taken  
378 over the four seasons, resulting in variables  $\overline{u_{kw,l}}^s$ ,  $\overline{T_{kw,l}}^s$  for the low-frequency component and similarly for the other two  
379 cases. The superscript  $s$  represents one of the four seasons: northern winter ( $s = DJF$ ), spring ( $s = MAM$ ), summer ( $s = JJA$ ),  
380 and autumn ( $s = SON$ ).

381 Cases (ii) and (iii) contain purely subseasonal variability and therefore one can expect their ~~mean 6-year~~ fields means to be  
382 zero-valued since variability beyond 90 days has been put to zero. Similarly, mean fields for each of the four seasons results

383 in  $\overline{u_{kw,h}}^s \ll \overline{u_{kw,l}}^s$  and  $\overline{u_{kw,m}}^s \ll \overline{u_{kw,l}}^s$  and the same for the temperature component. This reflects the fact that positive  
384 and negative phases of the fast KW responses average out to approximately zero on seasonal timescales (figure not shown).  
385 Therefore, the seasonal mean ~~over-of~~ the absolute amplitudes ~~for-of-the~~ zonal wind and temperature are examined instead,  
386 i.e.  $|\overline{u_{kw,h}}^s|$ ,  $|\overline{u_{kw,m}}^s|$  and similarly for temperature ~~component, in-order-to-study~~. This describes seasonal fluctuations in  
387 subseasonal KW amplitudes<sup>3</sup>.

388 Figure 7 shows results for all three cases after taking mean over the whole period. The left panel resembles a dominant  
389 "wave-1" structure with zonal wind maximized around 140 hPa. Easterly KW winds are strongest around 60°E and westerly  
390 winds around the Date Line. Note that two stationary perturbations over African (30°E) and South American (80°W) orography  
391 are the result of our terrain-following NMF analysis. If one compares the KW zonal wind pattern with the climatological zonal  
392 wind pattern in Fig. 3(a) it can be observed that the zonal wind pattern is located around 20° west of the climatological pattern.  
393 Wave temperature perturbations are largest where the vertical gradients in zonal wind are largest which explains the ~~quadripole~~  
394 ~~structure. Heating (cooling) by KWs is quadrupole structure. Warm and cold KW anomalies are~~ located at 100 hPa in ~~Eastern~~  
395 ~~(Western) Hemisphere and the other way around~~ the Eastern and Western hemisphere, respectively, and vice versa at 200-300  
396 hPa.

397 The average low-frequency or seasonal KW structure has a significant resemblance with the classical Gill-type KW solution  
398 (Gill, 1980) describing a steady-state linear wave response to convective forcing. The Gill-type KW solution is characterized  
399 by westerly upper-troposphere winds east of the large-scale convective source. In responds to the seasonal cycle of convection,  
400 the solution in Fig. 7a illustrates, in addition to a low-frequency KW variability in westerly winds, also a considerable  
401 low-frequency variability west of the convective outflow. This part of the signal represents the wave modulation effect of  
402 the propagating KWs on seasonal timescales.

403 The middle panel of Fig. 7 shows the average distribution of KW activity on intraseasonal timescales. The activity is largest  
404 in the Eastern Hemisphere ~~hemisphere~~ with average zonal wind maxima up to 3 ms<sup>-1</sup> and temperature maxima up to 0.7 K.  
405 Zonal wind activity is largest over a broad area between 90 and 150 hPa over the Indian Ocean and the Maritime Continent.  
406 Temperature activity occurs slightly higher around 90-100 hPa. Intraseasonal activity is locally somewhat increased also around  
407 120°W, west of the Andes mountain range.

408 Finally, Fig. 7c illustrates the average distribution of ~~free-propagating-intramonthly~~ KWs. The Eastern ~~Hemisphere~~ hemisphere  
409 again makes up for the larger KW activity than the Western hemisphere, but the maximum is located more upward in compar-  
410 ison to the intraseasonal scales, around 80 hPa. Zonal wind activity peaks up to 3 ms<sup>-1</sup> over a broad range of 70-110 hPa and  
411 temperature peaks over a more narrow area around 76 hPa (up to 0.75 K). The main area for KW activity is found over Indian  
412 Ocean region, while least wave activity is above central Pacific. Towards the stratosphere KW activity reduces and becomes  
413 more uniform along in ~~longitudal~~ longitudinal direction.

---

<sup>3</sup>Most previous studies define KW activity as square amplitude rather than absolute amplitude. In our high resolution dataset we observe highly localized patterns of the KW activity in the Eastern hemisphere due to ongoing wave amplification. By using absolute amplitudes we better visualize the longitudinal structure of the KW activity in comparison to its local maxima.



## 414 4.2 Low-frequency Kelvin wave variability

415 The seasonal patterns of the low-frequency components of the KW (~~from hereon referred to as the Gill-type KW response~~) is  
416 presented as pressure-longitudinal cross-sections along the equator (at 0.7°N) of the KW seasonal means, given by  $\overline{[u_{kw,l}]^s}$   
417 and  $\overline{[T_{kw,l}]^s}$  in Fig. 8.

418 The largest ~~Gill-type KW response is found during NH summer~~ amplitudes are found during the JJA months. A strong dipole  
419 "wave-1" pattern is evident in the TTL. The strongest zonal winds are found close to 150 hPa with easterlies up to  $-12 \text{ ms}^{-1}$   
420 centered over Indian Ocean and westerlies up to  $6 \text{ ms}^{-1}$  over the Western Pacific. Negative temperature KW anomalies at 110  
421 hPa are strongest as well during JJA with values up to 1.5 K over Indian Ocean and annually averaged value of  $-0.5 \text{ K}$  over  
422 Western Pacific.

423 During ~~NH winter DJF~~, the dipole pattern ~~is has~~ shifted more eastward and upward compared to ~~NH summer JJA~~ and has a  
424 more slanted structure. Easterly (westerly) KW winds are located more east over the Maritime continent (central Pacific) and  
425 are centered at 130 hPa. The upper temperature dipole pattern is found higher up at 90 hPa approximately. Values are somewhat  
426 weaker compared to NH summer with easterlies up to  $-6 \text{ ms}^{-1}$  and westerlies up to  $5 \text{ ms}^{-1}$ .

427 Finally, ~~NH autumn and spring seasons SON and MAM season months~~ are transition seasons with respect to the strength  
428 and position of the KW dipole as it moves west- and downward towards ~~summer JJA~~ and east- and upward towards ~~winter NH~~  
429 ~~spring DJF~~. MAM has the weakest KW dipole with slightly stronger westerly winds up to  $5 \text{ ms}^{-1}$ .

430 The longitudinal position and the strength of the ~~Gill-type low-frequency~~ KWs have been linked to the seasonal patterns of  
431 the background winds in the TTL representing the upper level monsoon and Walker circulations (Flannaghan and Fueglistaler,  
432 2013). The average background winds maximize at 150 hPa as shown in Fig. 3(a). In Fig. 8, one can see how the KW easterlies  
433 in ~~Eastern Hemisphere the Eastern hemisphere~~ are strongest during ~~NH summer JJA~~ in relation to the Indian-South Asian  
434 monsoon circulation. Background easterlies as strong as  $-30 \text{ ms}^{-1}$  are located approximately  $10^\circ$  east of the KW maximum  
435 easterlies. ~~NH winter DJF~~ has the strongest background westerlies in relation to the upper-level circulation of the Western  
436 Pacific anticyclones. ~~NH spring (autumn) MAM~~ shows similar background wind patterns compared to ~~NH winter (summer)~~  
437 DJF but with weaker circulation. SON shows similar patterns with JJA but with weaker winds.

438 Further details on longitudinal position and interannual variability of ~~Gill-type the low-frequency~~ KW response at its max-  
439 imum value at 150 hPa are illustrated by the Hovmoller diagram in Fig. 9. For comparison, tropical convection is represented  
440 as well through the OLR proxy variable averaged over  $15^\circ\text{S}$ - $15^\circ\text{N}$  latitudes. All fields have been filtered with a 90 day cut-  
441 off low-pass filter in order to highlight the seasonality. As a result, one can observe enhanced/reduced ~~Gill-type~~ KW activity  
442 during the same individual seasons as seen from the timeseries in Fig. 5. Above average seasonal KW activity with stronger  
443 Gill-type dipole structures occurred during the summer of 2007 (mainly through its easterlies at  $60^\circ\text{E}$ ) and during the winters  
444 of 2006-2007 and 2009-2010. In these winters, El-Nino was active and a clear longitudinal eastward shift is observed in OLR,  
445 in the background circulation (not shown), as well as in the Gill-type dipole KW structure. The El-Nino winter of 2009-2010  
446 was followed by a strong La Nina winter with an increase in tropical convection over the Maritime continent (note: OLR values  
447 below  $195 \text{ Wm}^{-2}$ ).

448 The vertical seasonal movement of the KW dipole has been linked with the seasonal movement of the tropical tropopause  
 449 height (Flannaghan and Fueglistaler, 2013; Ryu et al., 2008). The position of the tropical tropopause height (represented by  
 450 a static stability value of  $5 \times 10^{-4} \text{ s}^{-2}$  in Fig. 8) is found at approximately 85 hPa during winter-DJF and descends towards  
 451 100 hPa in summer-JJA, similar to values obtained from GPS-RO observations by Grise et al. (2010). In particular, during  
 452 summer-JJA, one can notice how the asymmetry in the tropical tropopause height over Indian Ocean around  $60^\circ\text{E}$  coincides  
 453 with increasing temperatures by the KW dipole up to 1.5 K. Such deformation of the tropical tropopause is also evident during  
 454 winter and autumn-DJF and SON seasons.

455 Figures 10a and 10b illustrate seasonal-mean KW temperatures  $\overline{T_{kw,l}}^s$  in relation to the tropical tropopause layer defined by  
 456 static stability  $N^2$ . Seasonal variations in KW temperatures are collocated with the position of the tropopause, descending down  
 457 from its highest position during winter-DJF to its lowest position during summer-JJA. Temperature amplitudes are observed to  
 458 decline roughly above  $N^2 = 5 - 6 \times 10^{-4} \text{ s}^{-2}$ . Within this zonal-mean seasonal picture, zonal asymmetries in  $N^2$  exist and are  
 459 found: (i) near the Date Line with values of  $8 \times 10^{-4} \text{ s}^{-2}$  at 80 hPa during winter-DJF and  $7 \times 10^{-4} \text{ s}^{-2}$  at 90 hPa during summer  
 460 JJA and (ii) lower at 100 hPa over the Indian Ocean during summer-JJA. Particularly during NH-summer-JJA, the deformation  
 461 of the zonal-mean static stability field collocates strongly with the position of a strong KW temperature anomaly over Indian  
 462 Ocean. A rough estimation is made on the contribution of the KW anomaly to the zonal deformation of the tropopause layer by  
 463 removing zonal-mean parts of both fields. First, static stability zonal anomalies,  $\overline{N'^2}^s$ , are derived by subtracting zonal-mean  
 464 values of  $N^2$  from the full  $N^2$  field per timestep and at every pressure level, followed by seasonal averaging. Next, we can  
 465 estimate the static stability change associated with the KW anomaly, using the relation:  $N_{kw}^2 = \frac{g}{\theta} \frac{\partial \theta_{kw}}{\partial z}$ , followed by seasonal  
 466 averaging as well, i.e.  $\overline{N_{kw}^2}^s$ .

467 As a result, Fig. 10c and 10d show how both static stability anomalies are overlapping. During winter-DJF, the structure of  
 468 the zonal anomaly  $\overline{N'^2}^s$  has a positively-valued tilt eastward which stretches up to 80 hPa, while during summer-JJA a strong  
 469 static stability anomaly is found more localized over Indian ocean region with values in the TTL up to  $\overline{N'^2}^{JJA} = \pm 0.8 \times 10^{-4}$   
 470  $\text{ s}^{-2}$ . The anomaly associated with the KW temperature anomaly is found to peak up to  $+0.6 \times 10^{-4} \text{ s}^{-2}$  during summer-JJA  
 471 and up to  $+0.4 \times 10^{-4} \text{ s}^{-2}$  during winter-DJF. Finally, by dividing both fields with each other, the resulting contribution of the  
 472 quasi-stationary Kelvin wave to the observed deformation of the tropical tropopause layer is estimated up to 60% (during JJA  
 473 and 80% )-during-NH-summer-(winter)during DJF.

#### 474 4.3 Intraseasonal Kelvin wave variability

475 The seasonality of intraseasonal Kelvin wave variability is shown in Fig. 11 and shall be briefly discussed here. The NH-winter  
 476 DJF stands out as the most active season for KW activity, located mainly in the Eastern hemisphere centered-centred at  $100^\circ\text{E}$   
 477 and with maximum activity at 110 hPa for zonal wind and temperature with a second maximum in temperature at 90 hPa.  
 478 Values observed are up to 0.8 K for KW temperature and  $5 \text{ ms}^{-1}$  for KW zonal wind. During NH-spring-MAM season, the  
 479 KW activity fields are weaker but spread over a larger area in the Eastern hemisphere and in the TTL with maximum activity  
 480 centered at 120 hPa (90 hPa) for the zonal wind (temperature) component. Both NH-summer and autumn-JJA and SON seasons  
 481 have KW activity positioned at lower altitudes and more westward. In both seasons, KW zonal wind activity is split up between



482 two structures with an eastward tilt with height; one with a maximum around 110°E and one pattern starting from 100 hPa and  
483 extending towards 60°E. Note also the increase in KW activity in the Western hemisphere below 150 hPa in the East Pacific.  
484 The maximum KW activity in the temperature component for both seasons is positioned near 100 hPa approximately on the  
485 tropical tropopause contour with value  $5 \times 10^{-4} \text{ s}^{-2}$ .

486 The eastward tilted structure is observed throughout all seasons except ~~NH-spring~~ MAM when background easterly winds  
487 are nearly absent in the Eastern hemisphere. In all other seasons one can observe how the tilted structure is locked to the  
488 background easterlies with maximum amplitudes located slightly above and west of it. Such eastward tilt with height has  
489 been frequently observed, for example over radiosonde station Medan at 100°E during the early stage of MJO development  
490 (Kiladis et al., 2005).

#### 491 4.4 Intramonthly Kelvin waves

#### 492 ~~4.5 Free-propagating Kelvin-waves~~

493 The seasonal variability of ~~free-traveling~~ intramonthly Kelvin waves, represented by their absolute amplitudes  $\overline{|u'_{kw,h}|^s}$  and  
494  $\overline{|T'_{kw,h}|^s}$ , shall be examined in relation to the background conditions. Figure 12 illustrates favorable regions for KW activity. In  
495 general, KW activity increases upward from around 120 hPa towards its zonal-mean peak value at 76 hPa. The largest values  
496 are observed in ~~EH~~ the Eastern hemisphere in region from 30°E till 150°E. The temperature component in particular has a  
497 constant maximum peak (up to 0.8 K ~~in EH~~) located around 76 hPa throughout the year, where also the largest increase in  $N^2$   
498 occurs as shown in Fig. 3. Above 70 hPa, KW activity continuously decreases in the stratosphere.

499 The longitudinal structure of the KW zonal wind shows two distinct peaks in the TTL, one consistently located at 76  
500 hPa and another around 100-110 hPa in the ~~EH~~ Eastern hemisphere which is mainly present during solstice seasons. The  
501 first maximum coincides with the temperature distribution which can be explained by their balance relationships and free  
502 horizontal propagation in the stratosphere. Below the tropopause, KW activity is coupled to convective processes alternating  
503 the tropospheric vertical wave structures as discussed by Flannaghan and Fueglistaler (2012).

504 The secondary maximum around 110 hPa in Fig. 12 is present mainly during solstice seasons in ~~EH~~ the Eastern hemisphere  
505 and it is associated with the seasonal movement of the background wind. The maximum of KW wind and the background wind  
506 maximum move eastward from ~~winter-to-summer~~ DJF to JJA season similar to the low-frequency variability. A day-by-day  
507 comparison of the KW activity and background wind confirms that propagating KWs amplify while approaching a region of  
508 strong easterlies, forming a folding structure around it while the individual KWs dissipate towards the center of easterly winds.  
509 One can notice in Fig. 12 a fast reduction of KW amplitudes eastward of its maximum towards the center of the background  
510 easterlies. It is likely related to dissipation and wave breaking processes as observed over Indonesia (120°E) by Fujiwara et al.  
511 (2003). Within such regions, the KW-background wind interaction becomes complex and the linearity assumption breaks  
512 (Ryu et al., 2008; Flannaghan and Fueglistaler, 2013).

513 A comparison with the previous study by Suzuki and Shiotani (2008) using ERA-40 data shows that the L91 data contain  
514 stronger KW activity in the vicinity of the background easterlies in the Eastern ~~Hemisphere~~ hemisphere, and more fine-scale

515 details which can be explained by better analyses based on more observations and improved models including increased  
516 resolution. For example, Suzuki and Shiotani (2008) used 5 levels of ERA-40 data between 50 and 200 hPa whereas the present  
517 study considers 25 model levels between 50 – 200 hPa. Maxima of the KW temperature signal appear in similar locations and  
518 strength except for a small offset in vertical position (70 hPa in Suzuki and Shiotani (2008) versus 80 hPa in Fig. 12) and a  
519 larger zonal asymmetry in our results.

520 Another view of the seasonal cycle of free propagating KWs is illustrated in Fig. 13 which focuses on the spatiotemporal  
521 distribution of individual KW ~~packetstracks~~. Hovmoller diagrams ~~are illustrated~~ of KW zonal wind and temperature at levels  
522 110 and 200 hPa ~~cumulated~~ from different years ~~are shown into a single calendar year~~ along with the background zonal wind.  
523 In addition, the monthly-mean values of daily maximum KW amplitudes occurring ~~at a specific longitude along the equator are~~  
524 ~~added next to in longitude are added on the rightside of~~ each diagram. ~~It represents seasonality in the KW maximum amplitudes~~  
525 ~~in a similar fashion to Fig. 6 in Alexander and Ortland (2010) which is based on HIRDLS satellite data.~~

526 The individual wave tracks at 110 hPa illustrate KWs with amplitudes exceeding  $3 \text{ ms}^{-1}$  and 0.6 K which are propagating  
527 throughout the year in the Eastern ~~Hemisphere~~~~hemisphere~~, during June–October months only over the Pacific, and all except  
528 ~~winter-DJF~~ months in most of the Western Hemisphere. Typical wave tracks start east of the  $0^\circ$  ( $30^\circ\text{W}$ ) meridian during  
529 winter (summer) and largely disappear west of  $120^\circ\text{E}$ . The largest wave amplitudes are observed between  $50^\circ\text{E}$  and  $100^\circ\text{E}$   
530 prior to regions of easterly winds in agreement with Fig. 12. Here presented details show that most notable waves appear  
531 during the Asian monsoon period with upper-level easterlies prevailing from June into September. The largest ~~Kelvin-wave~~  
532 ~~KW~~ amplitudes appear confined to the June and July months followed by a rapid drop in August. In fact, a local minimum in  
533 the number of KWs as well as in wave amplitudes occurs in August before the KW activity increases slightly during autumn.

534 At 200 hPa, the favorable area for KW propagation shifts to the Western Hemisphere and large KW activity is observed  
535 west of the South American continent throughout the year (west of  $80^\circ\text{W}$ ) with a westward extension over the Pacific during  
536 ~~northern-summer~~~~JJA~~. Another set of wave tracks starts over ~~equatorial~~~~equatorial~~ South America around  $30^\circ\text{W}$  ( $5^\circ\text{W}$ ) and  
537 continues till  $60^\circ\text{E}$  (~~during JJA. During DJF these wave tracks shift more east and start at  $5^\circ\text{W}$  and continue till  $90^\circ\text{E}$ ) during~~  
538 ~~northern-summer (winter)~~. The seasonal shifts of approximately  $30^\circ$  in KW tracks collocate with similar shifts in the prevailing  
539 TTL winds.

540 The amplitude of KWs undergoes a clear annual cycle with a small secondary peak present during ~~northern-winter~~~~DJF~~, as  
541 represented by the monthly-means of daily maximum amplitudes ~~along the equator~~ on the rightside of Fig. 13. The largest  
542 amplitudes are found at 110 hPa during ~~NH-summer~~~~JJA~~ with monthly-mean zonal wind (temperature) values up to  $8.5 \text{ ms}^{-1}$   
543 ( $1.8 \text{ K}$ ) in June. During the ~~winter-DJF~~ months Kelvin waves amplify more eastward with monthly-mean zonal wind (temper-  
544 ature) values up to  $7.8 \text{ ms}^{-1}$  ( $1.6 \text{ K}$ ) in December. ~~Our result matches well with the observed seasonal pattern in maximum~~  
545 ~~KW temperatures at 16km ( $\sim 100 \text{ hPa}$ ) from the HIRDLS satellite observations (Alexander and Ortland, 2010, Fig. 6).~~ At 200  
546 hPa, KW amplitudes are on average lower with a yearly-averaged amplitude reduction around 55% in temperature and 35% in  
547 zonal wind.

548 The semiannual cycle in maximum amplitudes remains visible up till 70 hPa. Above 70 hPa, where the KW activity remains  
549 large in Eastern ~~Hemisphere~~ hemisphere (Fig. 12), the semiannual cycle is replaced by an interannual cycle in line with the  
550 dominant impact of the QBO.

## 551 **5 Discussion and Conclusions**

552 We have applied the multivariate decomposition of the ECMWF operational analyses during the period 2007-2013 when  
553 the operational data assimilation ~~was and forecasting were~~ performed on 91 ~~levels. Model-level data were analyzed every 6~~  
554 ~~hours. The applied model levels. The applied normal-mode function~~ decomposition provides simultaneously the wind com-  
555 ponents, geopotential height and temperature perturbations of ~~the Kelvin waves on the terrain-following levels~~ Kelvin waves  
556 for many scale without any prior data filtering. The three-dimensional Kelvin wave structure in the upper troposphere and  
557 lower stratosphere is composed of Kelvin wave solutions of 60 linearized shallow-water equation systems on the sphere with  
558 equivalent depths from 10 km up to about 3 meters. As the KW meridional wind component is very small it is not discussed -  
559 here. We showed that large-scale KWs readily persist in the data despite analyzing selected processing times independently.

560 The KW is a normal mode of the global atmosphere and our 3D-orthogonal decomposition allows quantification of its  
561 contribution to the global energy spectrum and variability. We have presented the total (kinetic+potential) energy of KWs in  
562 the L91 data as a function of the zonal wavenumber in different seasons. The zonal wavenumber  $k = 1$  contains the largest  
563 portion of KW energy in all seasons. There is almost one third more energy in JJA than in MAM in  $k = 1$ . In  $k = 2$  there is  
564 50% less energy than in  $k = 1$  but JJA still contains most energy. In all larger zonal wavenumbers, the most energetic season is  
565 DJF.

566 We focused on the spatiotemporal features of the KW temperature and zonal wind components in the four seasons. The  
567 Kelvin wave seasonal cycle in the tropical tropopause layer (TTL) was compared with seasonal variability of the Outgoing  
568 Longwave Radiation (OLR), and the background wind and stability fields, which are believed to play an important role for  
569 the KW variability. Our study results of the seasonal KW variability ~~complements complement~~ previous studies which applied  
570 different methods for the KW filtering and different datasets. ~~As KW is a normal mode of the global atmosphere, our filtering~~  
571 ~~of the KW using the 3D-orthogonal normal-mode function decomposition of global data is a useful approach to quantification~~  
572 ~~of the KW variance. The KW is the most energetic inertio-gravity mode of the global atmosphere (Žagar et al., 2009) and~~  
573 ~~its representation in weather and climate models is crucial for reliable simulations of the tropics and its impact on global~~  
574 ~~circulation.~~

575 ~~We have presented the total energy of the KWs in the L91 data extending between the surface and 1 Pa as a function of the~~  
576 ~~zonal wavenumber. Zonal wavenumber  $k = 1$  contains a largest portion of KW energy in all seasons. Its energy varies between~~  
577  ~~$\sim 300$  in JJA in NH spring to over 400 J/kg in NH summer. In  $k = 2$  there is 50% less energy than in  $k = 1$  but the NH summer~~  
578 ~~is still the most energetic season. In all greater zonal wavenumbers, DJF season contains most energy.~~

579 Frequency The frequency spectrum has revealed a semiannual cycle as well as intraseasonal and intramonthly variabil-  
580 ity. Three ranges of wave periods were analyzed: 3-20 days, 20-90 days and longer than 90 days. This choice was partly

581 deliberate in order to compare our results with several previous studies of KW variability. First we demonstrated that the  
582 ~~seasonal-mean KW low-frequency KW dipole~~ pattern in the TTL, with ~~(westerly-) easterly-westerly~~ winds in the ~~(Western-)~~  
583 ~~Eastern hemisphere resembles a time-averaged Western hemisphere and with easterly winds in the Eastern hemisphere, partly~~  
584 ~~resembles a seasonal-averaged~~ Gill-type "wave-1" pattern ~~and contains partly low-frequency modulation of vertically-propagating~~  
585 ~~KWs~~. The quadrature-shaped temperature component represents a thermally adjusted pattern with respect to the zonal wind  
586 component, and contributes to seasonal ~~(cooling)-warming~~ above 100 hPa in the ~~(Eastern) Western Western and cooling in the~~  
587 ~~Eastern~~ hemisphere. The largest KW amplitudes are observed during ~~summer and winter JJA and DJF~~ seasons. From boreal  
588 summer towards winter, KW ~~perturbation-perturbations~~ moves eastward (from Indian Ocean basin towards Maritime Conti-  
589 nent) and upward (e.g. zonal wind component moves up from 150 hPa towards 120 hPa). The KW zonal wind amplitude varies  
590 between 12 m/s strong easterlies over Indian ocean near 150 hPa in JJA to 6 m/s over Western Pacific. Over Indian Ocean in  
591 JJA, the KW easterlies thus make almost half of the total wind vector. The associated KW temperature perturbations are from  
592 1.5 K over Indian ocean in JJA to -0.5 K over West Pacific. The zonal modulation of Kelvin waves is found to be locked with  
593 respect to the seasonal movement of convection and the convective outflow in the TTL. The modulation effect is strongest  
594 for ~~Gill-type the low-frequency~~ Kelvin waves during the summer monsoon season, when strong easterly winds are present at  
595 150 hPa, resulting in the largest KW zonal wind and temperature anomalies, of which the latter results in deformation of the  
596 tropical tropopause over Indian Ocean.

597 Intraseasonal (periods 20-90 days) activity is strongest in ~~NH-winter DJF~~ with maxima up to 0.8 K for KW temperature  
598 and up to 5 m/s for KW zonal wind centred at 120°E. Both temperature and zonal wind activities have eastward tilt with  
599 height. In comparison to previous study by Suzuki and Shiotani (2008) using ERA-40 data, the slanted structure in the present  
600 data continues to extend more upward and eastward which is likely due to the increased number of vertical model levels  
601 compared to ERA-40. The importance of vertical model resolution for the KW ~~wave~~-structure and amplitude was demonstrated  
602 in Žagar et al. (2012) and Podglajen et al. (2014).

603 For periods 3–20 days, the seasonal cycle of KWs is clearly seen in ~~the~~ wave amplitude. ~~The In the zonal-mean perspective,~~  
604 ~~the~~ largest amplitudes are located ~~-from a zonal-mean perspective-~~ between 70 and 100 hPa for both zonal wind and tem-  
605 perature ~~as expected for the free-propagating Kelvin waves~~ but it is modulated by the seasonal movement of the TTL. A  
606 major zonal asymmetry was found in KW activity: around 110 hPa ~~the~~ Kelvin wave undergoes amplification mainly in ~~Eastern~~  
607 ~~Hemisphere the Eastern hemisphere~~ during the solstice seasons, while at 200 hPa a secondary region of ~~the~~ KW amplifica-  
608 tion occurs in ~~Western Hemisphere the Western hemisphere~~ during boreal summer. ~~Free-propagating The intermonthly~~ KWs  
609 show largest amplitudes in the vicinity of the strongest easterlies preferably west and above the ~~center-centre~~ of easterlies. The  
610 ~~NMF methodology has made applied novel methodology makes~~ it possible to observe such dynamics on daily basis whenever  
611 easterlies are strong in the TTL. Nearly real-time representation of the KW activity is available on <http://modes.fmf.uni-lj.si>.

612 In summary, our seasonal variability analysis shows that the background wind in the TTL linked with convective outflows,  
613 play a dominant role in the longitudinal position where ~~the~~ zonal modulation of Kelvin waves is preferred, while the tropical  
614 tropopause and its seasonal vertical movement ~~determines-determine~~ the vertical extent of ~~the~~ KW modulation processes.

615 *Acknowledgements.* This study was funded by the European Research Council (ERC), Grant Agreement no. 280153 **MODES**, <http://meteo.fmf.uni-lj.si/MODES>.  
616 [MODES. We are grateful to Dr George Kiladis and an anonymous reviewer for their detailed constructive comments.](#)

617 **References**

- 618 Alexander, M. J. and Ortland, D. A.: Equatorial waves in High Resolution Dynamics Limb Sounder (HIRDLS) data, *J. Geophys. Res.*, 115,  
619 D24 111, <https://doi.org/10.1029/2010JD014782>, 2010.
- 620 Andrews, D. G., Holton, J. R., and Leovy, C. B.: *Middle atmospheric dynamics*, Academic Press, 1987.
- 621 Baldwin, M. P. and Coauthors: The Quasi-Biennial Oscillation, *Rev. Geophys.*, 39, 179–229, 2001.
- 622 Boyd, J. P.: The Effects of Latitudinal Shear on Equatorial Waves. Part II: Applications to the Atmosphere, *J. Atmos. Sci.*, 35, 2259–2267,  
623 1978.
- 624 Boyd, J. P.: *Dynamics of the Equatorial Ocean*, Springer-Verlag GmbH Germany 2018, 2018.
- 625 Boyd, J. P. and Zhou, C.: Uniform Asymptotics for the Linear Kelvin Wave in Spherical Geometry, *J. Atmos. Sci.*, 65, 655–660,  
626 <https://doi.org/10.1175/2007JAS2356.1>, 2008.
- 627 Ern, M. and Preusse, P.: Wave fluxes of equatorial Kelvin waves and QBO zonal wind forcing derived from SABER and ECMWF temperature  
628 space-time spectra, *Atmos. Chem. Phys.*, 9, 3957–3986, 2009.
- 629 Ern, M., Preusse, P., Krebsbach, M., Mlynczak, M. G., and Russell, J. M.: Equatorial wave analysis from SABER and ECMWF temperatures,  
630 *Atmos. Chem. Phys.*, 8, 845–869, 2008.
- 631 Flannaghan, T. J. and Fueglistaler, S.: Tracking Kelvin waves from the equatorial troposphere into the stratosphere, *J. Geophys. Res.*, 117,  
632 <https://doi.org/10.1029/2012JD017448>, d21108, 2012.
- 633 Flannaghan, T. J. and Fueglistaler, S.: The importance of the tropical tropopause layer for equatorial Kelvin wave propagation, *J. Geophys.*  
634 *Res.*, 118, 5160–5175, 2013.
- 635 Fueglistaler, S., Dessler, A. E., Dunkerton, T. J., Folkins, I., Fu, Q., and Mote, P. W.: Tropical tropopause layer, *Reviews of Geophysics*, 47,  
636 <https://doi.org/10.1029/2008RG000267>, 2009.
- 637 Fujiwara, M., Yamamoto, M. K., Hashiguchi, H., and Horinouchi, T.: Turbulence at the tropopause due to breaking Kelvin waves observed  
638 by the Equatorial Atmosphere Radar, *Geophysical Research Letters*, 30, 1171, <https://doi.org/10.1029/2002GL016278>, 2003.
- 639 Garcia, R. R. and Salby, M. L.: Transient response to localized episodic heating in the Tropics. Part II: Far-field behavior, *J. Atmos. Sci.*, 44,  
640 499–530, 1987.
- 641 Garcia, R. R., Lieberman, R., Russell III, J. M., and Mlynczak, M. G.: Large-scale waves in the mesosphere and lower thermosphere observed  
642 by SABER, *J. Atmos. Sci.*, 62, 4384–4399, <https://doi.org/10.1175/JAS3612.1>, 2005.
- 643 Gill, A. E.: Some simple solution for heat-induced tropical circulation, *Quart. J. Roy. Meteor. Soc.*, 106, 447–462, 1980.
- 644 Gill, A. E.: *Atmosphere-Ocean Dynamics*, Academic Press, New York, 1982.
- 645 Grise, K. M., Thompson, D. W. J., and Birner, T.: A global survey of static stability in the stratosphere and upper troposphere, *J. Climate*, 23,  
646 2275–2292, 2010.
- 647 Hayashi, Y.: Space-time spectral analysis and its applications to atmospheric waves, *J. Meteor. Soc. Japan*, 60, 156–171, 1982.
- 648 Highwood, E. J. and Hoskins, B. J.: The tropical tropopause, *Q.J.R. Meteorol. Soc.*, 124, 1579–1604, 1998.
- 649 Holton, J. R.: *An introduction to dynamical meteorology*, vol. 4, Elsevier Academic Press, 2004.
- 650 Holton, J. R. and Lindzen, R. S.: An updated theory for the quasi-biennial cycle of the tropical stratosphere, *J. Atmos. Sci.*, 29, 1076–1080,  
651 1972.
- 652 Kasahara, A.: Normal modes of ultralong waves in the atmosphere, *Mon. Wea. Rev.*, 104, 669–690, 1976.

653 Kasahara, A.: Effect of zonal flows on the free oscillations of a barotropic atmosphere, *J. Atmos. Sci.*, 37, 917–929. Corrigendum, *J. Atmos.*  
654 *Sci.*, 38 (1981), 2284–2285, 1980.

655 Kasahara, A. and Puri, K.: Spectral representation of three-dimensional global data by expansion in normal mode functions, *Mon. Wea. Rev.*,  
656 109, 37–51, 1981.

657 Kedzierski, R. P., Matthes, K., and Bumke, K.: The tropical tropopause inversion layer: variability and modulation by equatorial waves,  
658 *Atmos. Chem. Phys.*, 16, 11 617–11 633, <https://doi.org/10.5194/acp-16-11617-2016>, 2016.

659 Kiladis, G. N., Straub, K. H., and Haertel, P. T.: Zonal and vertical structure of the Madden–Julian Oscillation, *J. Atmos. Sci.*, 62, 2790–2809,  
660 <https://doi.org/10.1175/JAS3520.1>, 2005.

661 Liebmann, B. and Smith, C. A.: Description of a complete (interpolated) outgoing longwave radiation dataset, *Bull. Am. Meteorol. Soc.*, 77,  
662 1275–1277, 1996.

663 Lin, J.-L. and Coauthors: Tropical intraseasonal variability in 14 IPCC AR4 climate models. Part I: Convective signals, *J. Climate*, 19,  
664 2665–2690, 2006.

665 Matsuno, T.: Quasi-geostrophic motions in the equatorial area, *J. Meteor. Soc. Japan.*, 44, 25–43, 1966.

666 Podglajen, A., Hertzog, A., Plougonven, R., and Žagar, N.: Assessment of the accuracy of (re)analyses in the equatorial lower stratosphere,  
667 *J. Geophys. Res. Atmos.*, 119, 11 166–11 188, <https://doi.org/10.1002/2014JD021849>, 2014.

668 Randel, W. J. and Wu, F.: Kelvin wave variability near the equatorial tropopause observed in GPS radio occultation measurements, *J.*  
669 *Geophys. Res.*, 105(D12), 15 509–15 523, <https://doi.org/10.1029/2000JD900155>, 2005.

670 Ratnam, M. V., Tsuda, T., Kozu, T., and Mori, S.: Long-term behavior of the Kelvin waves revealed by CHAMP/GPS RO measurements and  
671 their effects on the tropopause structure, *Ann. Geophys.*, 24, 1355–1366, 2006.

672 Ryu, J.-H., Lee, S., and Son, S.-W.: Vertically propagating Kelvin Waves and tropical tropopause variability, *J. Atmos. Sci.*, 65, 1817–1837,  
673 2008.

674 Salby, M. L. and Garcia, R. R.: Transient response to localized episodic heating in the tropics. Part I: Excitation and short-time near-field  
675 behavior, *J. Atmos. Sci.*, 44, 458–498, 1987.

676 Shumway, R. and Stoffer, D.: Time series analysis and its applications: with R examples, Springer texts in statistics, Springer New York,  
677 <https://doi.org/https://books.google.si/books?id=dbS5IQ8P5gYC>, 2010.

678 Son, S.-W., Lim, Y., Yoo, C., Hendon, H. H., and Kim, J.: Stratospheric Control of the Madden–Julian Oscillation, *Journal of Climate*, 30,  
679 1909–1922, <https://doi.org/10.1175/JCLI-D-16-0620.1>, 2017.

680 Suzuki, J. and Shiotani, M.: Space-time variability of equatorial Kelvin waves and intraseasonal oscillations around the tropical tropopause,  
681 *J. Geophys. Res.*, 113, D16 110, <https://doi.org/10.1029/2007JD009456>, 2008.

682 Tindall, J. C., Thuburn, J., and Highwood, E. J.: Equatorial waves in the lower stratosphere. II: Annual and interannual variability, *Q.J.R.*  
683 *Meteorol. Soc.*, 132, 195–212, <https://doi.org/10.1256/qj.04.153>, 2006.

684 Tsai, H.-F., Tsuda, T., Hajj, G., Wickert, J., and Aoyama, Y.: Equatorial Kelvin waves observed with GPS occultation measurements (CHAMP  
685 and SAC-C), *J. Meteor. Soc. Japan.*, 82, 397–406, 2004.

686 Žagar, N., Andersson, E., and Fisher, M.: Balanced tropical data assimilation based on a study of equatorial waves in ECMWF short-range  
687 forecast errors, *Q.J.R. Meteorol. Soc.*, 131, 987–1011, <https://doi.org/10.1256/qj.04.54>, 2005.

688 Žagar, N., Andersson, E., Fisher, M., and Untch, A.: Influence of the quasi-biennial oscillation on the ECMWF model short-range forecast  
689 errors in the tropical stratosphere, *Q. J. R. Meteorol. Soc.*, 133, 1843–1853, 2007.

690 Žagar, N., Tribbia, J., Anderson, J. L., and Raeder, K.: Uncertainties of estimates of inertia-gravity energy in the atmosphere. Part II: Large-  
691 scale equatorial waves, *Mon. Wea. Rev.*, 137, 3858–3873, Corrigendum: 138:2476-2477, 2009.

692 Žagar, N., Terasaki, K., and Tanaka, H. L.: Impact of the vertical resolution of analysis data on the estimates of large-scale inertio-gravity  
693 energy, *Mon. Wea. Rev.*, 140, 2297–2307, 2012.

694 Žagar, N., Kasahara, A., Terasaki, K., Tribbia, J., and Tanaka, H.: Normal-mode function representation of global 3D datasets: Open-access  
695 software for the atmospheric research community, *Geosci. Model Dev.*, 8, 1169–1195, 2015.

696 Wallace, J. M. and Gousky, V. E.: Observational evidence of Kelvin waves in the tropical stratosphere, *J. Atmos. Sci.*, 25, 900–907, 1968.

697 Wheeler, M. and Kiladis, G. N.: Convectively coupled equatorial waves: Analysis of clouds and temperature in the wavenumber-frequency  
698 domain, *J. Atmos. Sci.*, 56, 374–399, 1999.

699 Yang, G.-Y. and Hoskins, B. J.: ENSO impact on Kelvin Waves and associated tropical convection, *J. Atmos. Sci.*, 70, 3513–3532, 2013.

700 Yang, G.-Y., Hoskins, B. J., and Slingo, J.: Convectively coupled equatorial waves: A new methodology for identifying wave structures in  
701 observational data, *J. Atmos. Sci.*, 60, 1637–1654, 2003.